Inaugural - Dissertation

zur Erlangung der Doktorwürde der
Naturwissenschaftlich - Mathematischen
Gesamtfakultät der
Ruprecht - Karls - Universität Heidelberg

vorgelegt von
Diplom Mathematikerin
Elfriede Friedmann
aus Temeschburg/Rumänien

Tag der mündlichen Prüfung: 10.11.2005

Thema

Riblets in the viscous sublayer

Optimal Shape Design of Microstructures

Gutachter Prof. Dr. Dr. h.c.mult Willi Jäger

Prof. Dr. Rolf Rannacher

Abstract

Previous research has established that a smooth surface has not necessarily minimal drag: Many experiments by different laboratories, e.g. NASA and DLR Berlin, indicate that an extra surface layer with tiny grooves aligned in the stream-wise direction can be used to reduce the drag. The aim of this project is to find the optimal shape of such microstructures on surfaces of submerged bodies. We assume that these microstructures remain in the viscous sublayer where the flow equations are the 3D incompressible, steady state Navier-Stokes equations with a Couette in- and outflow determinated through two boundary conditions, the no-slip condition on the lower boundary and the friction condition on the upper one. The objective function of our optimization problem is the tangential drag force, which we want to minimize. Solving this problem is difficult because of the rough boundary, which causes a big amount of data. We apply homogenization theory and replace the rough boundary by a smooth one, where the right boundary conditions have been determined. Furthermore, our optimization problem can be simplified using this approximation and we end up minimizing a scalar size, the Navier constant, which is calculated using the velocity of an auxiliary boundary layer equation. To solve the optimization problem we use sensitivity-based optimization methods. The sensitivity is calculated analytically and we use it to determine the gradient of the cost function with respect to the design variable. A minimum is sought by using the steepest descent algorithm with step size according to Armijo rule. The necessary optimality conditions are derived and a sequence of admissible domains is built which tends to the optimal solution. The state equations are solved numerically using finite elements on unstructured grids and multigrid algorithms. The results obtained with this approach give us a drag reduction of approximately 2–6% relative to the drag of the smooth configuration.

Zusammenfassung

Bisherige Forschung hat gezeigt, dass eine glatte Oberfläche eines in Flüssigkeit eingetauchten Körpers nicht die minimale Widerstandskraft haben muss: So kann eine hauchdünne Folie mit Rillen, die in Strömungsrichtung ausgerichtet sind, als widerstandsminimierende Oberfläche dienen. Dieser Ansatz resultierte aus den Forschungsergebnissen der NASA und der DLR Berlin. Das Ziel dieses Projekts besteht darin, die optimale Form der Mikrostrukturen auf der Oberfläche zu finden, so dass die Widerstandskraft minimal wird. Bei der Modellierung müssen wir uns darauf beschränken, dass die Rillen aus der viskosen Grenzschicht nicht herausragen. Die Strömungsgleichungen können dann durch die inkompressiblen stationären Navier-Stokes Gleichungen beschrieben werden. Als Ein- und Ausströmung ist eine Couette Strömung festgelegt, die am unteren Rand durch die Haft- und am oberen Rand durch die Reibungsbedingung gegeben ist. Das Zielfunktional unseres Optimierungsproblems ist die tangentiale Widerstandskraft. Die Lösung dieses Problems gestaltet sich schwierig, da der untere rauhe Rand eine Handhabung großer Datenmengen erfordert. Durch Anwendung von Homogenisierung können wir diesen rauen Rand durch einen glatten ersetzen, wobei die Informationen der Rauheiten durch andere Randbedingungen mitgegeben werden. Nach einer Reihe von Approximationen wird das

ursprüngliche Optimierungsproblem so vereinfacht, dass die Zielfunktion durch eine skalare Größe, der Navier Konstanten, und die Nebenbedingungen durch die Grenzschichtgleichungen gegeben sind. Zur Lösung des Optimierungsproblems verwenden wir die auf Sensitivitäten basierenden Optimierungsmethoden. Die Sensitivitäten, die zur Bestimmung des Gradienten des Zielfunktionals bezüglich der Designvariablen dienen, werden analytisch bestimmt. Ein Minimum wird durch das Verfahren des steilsten Abstiegs mit regulierter Schrittweite nach der Armijo Regel gesucht. Die notwendigen Optimalitätsbedingungen werden abgeleitet, und eine Minimalfolge zulässiger Gebiete gebildet. Die Nebenbedingungen, die durch die Grenzschichtgleichungen gegeben sind, werden nummerisch durch eine Finite-Elemente-Diskretisierung auf unstrukturierten Gittern mittels Mehrgitterverfahren gelöst. Die so erhaltenen Ergebnisse weisen eine Widerstandsminimierung zwischen 2 und 6% relativ zum Widerstand der glatten Oberfläche auf.

Es gibt keine großen Entdeckungen und
Fortschritte, solange es noch ein
unglückliches Kind auf Erden gibt.

Albert Einstein (14.03.1879 - 18.04.1955)

Contents

List of Figures

List of Tables

Introduction

Shape optimization is nowadays very important in industry and science. It is used to improve technical properties of materials and devices to obtain higher profit at an increased or at least equal level of reliability. In the general context of shape optimization we have to distinguish three branches of optimization: size, classical shape and topology optimization. In the first branch, the size optimization, a typical size of an object is used as optimization parameter, e.g. a thickness distribution, whereas other dimensions are kept fix; several examples can be found in [26]. In the second branch, the classical shape optimization, the shape of a given domain is altered, keeping the topology unchanged. In the third branch, the topology optimization, the topology and the shape are allowed to change. Considering beam structures, the topology can be changed by varying the number of the beams, or considering continuous structures, by adding holes to the domain (see [15] for both cases).

Problems of shape optimization are typically of interdisciplinary character: At first, a model has to be crafted thoroughly, which requires knowledge of the physical background; then a solution to the equations has to be found. Since most of the solutions can not be found analytically, a numerical approximation has to be supplied. The following mathematical areas come together in this process: the theory of partial differential equations (or of ordinary differential equations), approximation of these partial differential equations (for example using finite elements), and the theory of mathematical programming. In this thesis we present a shape optimization problem in the field of fluid mechanics with practical applications. A further area of mathematics, the theory of fluid dynamics, plays an important role to handle the state problem. An additional difficulty appears in our problem where we want to optimize a rough boundary of very small size, on the so-called micro scale. Models with different scales are difficult to handle numerically. Homogenization has to be used to approximate the oscillating model by a smooth one, where the coefficients of the smooth model are obtained through a limiting process. In literature (see [26], [41] and [48]) we find several examples of shape optimization with fluid dynamical applications, and we find homogenization applied to riblets in [1], [5]. We want to combine all these fields in this thesis applying shape optimization to a homogenized model after a complex process of modeling and approximations.

It was first observed by Walsh that rough surfaces can have a lower drag than a smooth one: In [8], [9], [10], [11], [58] experiments on flows over rough surfaces are presented. The authors chose three or more possible shapes of rough surfaces and compared the values for the drag. The idea how to choose the shapes are given by a shark skin model. Sharks belong to one of the oldest species, are fast and silent swimmers, and have evolved such

that their shape is adapted to their environment. The rough structure on their surface, well-investigated in [53], is nowadays of great interest. The most durable materials, such as fiberglass, are built based upon the same principles. The most important property of this rough structure is its contribution to drag reduction. The longitudinal riblets impede the vortices of the cross flow and thus reduce drag. An artificial shark skin was build by DLR Berlin. The model was enlarged significantly for manufacturing reasons and tested in an oil channel. An artificial shark skin of small size was developed by NASA laboratories to test the drag reduction capability. This thin plastic film was then produced by the company 3M and applied to the surface of an Airbus A340 and to the hull of the sailboat *Stars and Stripes*. The turbulent shear stress reduction obtained was about 7–8%. This means for the case of the aircraft a saving of 3% of the total fuel per flight. The same amount of drag reduction was obtained by testing the swimming suit *Fastskin* developed by the company Speedo, this swimming suit imitates the shark skin too. The structure of shark skin is known not only as a drag reducing tool but also as modern protective coating replacing the toxic anti-fouling used before 2003. The costs of shipping companies are so reduced by an artificial shark skin acting as anti-fouling and with this the drag can be reduced indirectly up to 15%.

The experiments carried out by Walsh, Bechert and co-workers, the results obtained from the different laboratories (NASA, DLR), and tests of rough surfaces on aircrafts, ships and swimming suits, are the motivation for this thesis. We solve the following problem: Find the optimal shape of microstructures on a submerged body such that its tangential drag force is minimized. Our considerations are based upon Schlichting's boundary layer theory for microstructures within the viscous sublayer of the boundary layer, and upon the homogenization results obtained by W. Jäger and A. Mikelić in [32], [33]. The contribution of this thesis is to model and to solve the three-dimensional shape optimization problem using these homogenization results and to find a connection between the theory developed here and the experimental results. From the set objectives, we achieved the following results: From our calculations we obtained a shape of microstructures which is up to 6% better than the smooth surface. Calculating the sensitivity analytically we could improve the cost function of our optimization problem by a sequence of shrinking domains. The optimal shape found is a thin peak represented by cubic spline functions. Enlarging the class of admissible shapes by imposing less regularity, the calculations done on the slit domain in two dimensions and on blade like riblets in three dimensions gave the best results. One connection to the experiments mentioned above is that the spacing of the ridges is twice their height. This structure is found also on the shark skin. An important result is the validity of the homogenized model resulting from the comparison with direct calculations on the rough boundary.

This thesis consists of three parts: Modeling the flow equations in the two-dimensional rough channel, solving the two-dimensional shape optimization problem, and modeling and solving the flow equations in the three-dimensional rough channel with longitudinal riblets, similar to those found on shark skin, using results from the two-dimensional problem.

The first part deals with the mathematical modeling of the two-dimensional optimization problem which means finding the optimal shape of the periodically distributed roughness at the bottom of the channel in order to minimize the tangential drag force. To model the

flow over very small rugosities we have to consider the boundary layer theory developed by Schlichting (see [54]). Because analysis in the buffer layer is out of reach until now, we restrict our model by keeping the roughness within the viscous sublayer of this boundary layer. In this regime the fluid motion can be described by the incompressible steady state Navier-Stokes equation with a Couette flow profile prescribed at the in- and out-flow boundary and given by the boundary conditions, the velocity U on the upper boundary and the no-slip condition at the lower boundary, which is fixed at the in- and outflow through the maximal height of the microstructure. This system has oscillating coefficients which makes it hard to solve it numerically. We apply homogenization to approximate this system with one having smooth coefficients. Because the small rugosities do not influence the main flow the limiting equations will also be given by the incompressible steady state Navier-Stokes equation with a perturbed Couette flow profile. This profile is given by a different boundary condition on the artificial smooth boundary, called wall law. Wall laws are an approach where the no-slip condition at rough surfaces are replaced by the non-penetration condition plus a relation between the tangential velocity and the shear stress, the slip condition. In [32] W. Jäger and A. Mikelić justified the wall laws by multiscale expansions. In numerous former papers the flow over a porous medium was studied, and in [31] the effective boundary conditions at the contact interface between a porous medium and a viscous incompressible fluid were derived rigorously. The interface condition of Beavers and Joseph was replaced by the condition of Saffman, because the filtration velocity is much smaller:

$$\frac{\partial u_\tau}{\partial \nu} = \alpha(\kappa^\varepsilon)^{-\frac{1}{2}} u_\tau + O(\varepsilon).$$

For the case of flow over rough boundaries an analogous wall law was found with different parameters called Navier slip condition:

$$u_1^{\text{eff}} = -\varepsilon C_{\text{bl}} \frac{\partial u_i^{\text{eff}}}{\partial x_2} \text{ on } S,$$

where the Navier constant C_{bl} is calculated from an auxiliary boundary layer problem. Usually this wall laws are determined empirically and differ in each problem. Mostly they are given by a non-linear function of the tangential velocity. In [42], O. Pironneau announced a rigorous result for the approximation of the Stokes flow over a rough boundary, and in [2] the authors obtained the effective wall laws for a flow over a rough surface at high Reynolds numbers, proportional to $\frac{1}{\varepsilon}$, constructing an asymptotic expansion with the help of boundary layer correctors, but only a numerical validation is presented therein. In [32] and [33] convergence results are proved for the asymptotic expansion of the velocity, for the mass-flow and for the tangential drag force, and the constants in the wall law were determined. The solution of the so-called effective equations of our model can be given analytically, it is the effective Couette flow determined by the boundary condition on the upper boundary, the prescribed velocity U and the Navier slip condition. With this effective solution we can approximate the oscillating tangential drag force with the so-called effective tangential drag force accurately:

$$\mathcal{F}_{\text{t}}^{\text{eff}} = \frac{\nu}{2} \frac{U}{L_2 - \varepsilon C_{\text{bl}}}.$$

The resulting simplified optimization problem consists of finding the optimal shape of a microstructure in one cell of roughness which minimizes the effective drag and with this the Navier constant C_{bl}. The state equations of this problem are then reduced to the boundary layer equations, the Stokes equation with additional boundary condition on the interface. Before solving this problem we compare the drag of the smooth configuration with the rough one and conclude that the rough one has a lower drag indeed so that our optimization problem is justified. To have a well-posed optimization problem we have to impose some constraints on the shape. We are interested in comparing shapes of riblets with the same height. To fix it correctly in the cell problem we analyze first the effect of different spacing on the cost function.

In the second part of this thesis we solve the two-dimensional optimization problem. The theory which deals with the differentiation of functionals with respect to the design variables is called sensitivity analysis and is a very important ingredient of the optimization process. To calculate the sensitivities, the gradient information, it is important to parametrize the shape function and to establish the design parameters. In our model the part of the boundary to be determined is described by the graph of a smooth function which is twice continuously differentiable. This makes the analysis and the numerical realization much easier. The change in geometry is described as a normal variation of the domain: $\Gamma_\lambda = \{s+\lambda\alpha(s)n(s)|\, s \in \Gamma\}$. To guarantee that the regularity of the boundary Γ will not get lost after some iterations, the function α must be small and twice continuously differentiable. After having an analytical representation of the sensitivities

$$\delta\mathcal{J} = \int_\Gamma \alpha(s)|\partial_n \beta^{\mathrm{bl}}(s)|^2 ds + o(||\alpha||_{C^2[0,1]})$$

it is obvious how to determine the optimal states by using optimization algorithms which require gradients. For the optimization routine we choose the steepest descent with Armijo line search. To solve the state equations we can use a tool box for solving partial differential equations which is able to capture the rough boundary. First, the state problem has to be approximated on a finite domain, i.e. the infinite boundary layer has to be cut at a position k and boundary conditions have to be imposed on this new boundary. We use the package FEMLISP developed by N. Neuss from the technical simulation group of the IWR in order to solve a boundary layer equation of fluid flow over a porous bed. For our model of fluid flow over a rough boundary we had the advantage that with this program the Navier constant could be calculated directly and the output could be reduced to the gradient of the velocities on the rough boundary. We were able to find corresponding results in the approximation techniques. For the discretization, finite elements on unstructured grids and multigrid algorithms are used. In the important last section of part two we compare the calculations for the homogenized problem with calculations on the original oscillating problem. These calculations, which we refer to as direct simulations, are a contribution of R. Rannacher in order to validate our calculations done on the homogenized model. The direct calculations evaluating the tangential drag force on the rough boundary can be performed at larger scales (0.02 – 0.3mm) and are more accurate for them. Nevertheless, at smaller scales the results from both models are nearly the same. The importance of homogenization is highlighted when we consider very small scales ($<$ 0.01mm). Due to the spectacular progress in the last decades, important analytical tools were developed in this field. Our effective model and the effective tangential drag force,

derived using these tools, replace the oscillating model and drag force which can not be calculated anymore with direct simulations. Using special limiting behavior of asymptotic expansions we are able to give statements about these very small scales which would never be possible by numerics only. But even for larger scales the homogenized model can be used to get first results. It is much easier to implement and the calculations are less complex and therefore much cheaper because the domain of computations is reduced to one cell of roughness with artificial boundary conditions on the smooth interface. This cell is only a small part of the whole rough channel. The calculations can be performed on a normal personal computer, whether the direct simulations requires special algorithms to capture the complicated structure of the rough boundary. These direct calculations are needed if one is interested in the exact values for the solutions or the drag force for larger scales. We used them also to compare the drag reducing effect of the microstructures with the results obtained in the experiments and found that microstructures with height of 0.15mm reduce the tangential drag force with 12% compared to the smooth surface. This result is close to the one obtained from Bechert and his co-authors in [10], where he found an drag reduction of 10%. The direct calculations presented in this section were done by Th. Richter using Gascoigne.

In the third part the three-dimensional model of a rough channel is presented: This model describes the rough shark skin of fast swimming sharks. First, the homogenization results for an arbitrary rough geometry obtained by W. Jäger and A. Mikelić in [33] are presented. Here, the Navier slip condition has a matrix coefficient in front of the effective shear stress:

$$u_j^{\text{eff}} = -\varepsilon \sum_{i=1}^{2} M_{ji} \frac{\partial u_i^{\text{eff}}}{\partial x_3}, \quad j = 1, 2 \text{ on } S.$$

This comes from the boundary condition on the upper boundary, the prescribed velocity $U = (U_1, U_2, 0)$, which is imposed to model the correct viscous sublayer. Even if the stream velocity is chosen only in the x-direction, we will have a velocity in the y-direction because of the vortices which occur in the upper layer. The Navier matrix M is calculated using again an auxiliary boundary layer problem and its structure depends on the shape of the microstructure. Because of the physiognomy of sharks, the applications and experiments we restrict the three-dimensional shape of our layer of roughness to longitudinal riblets. This simplifies the problem significantly: On the one hand, because the Navier matrix is then not only negative definite but also diagonal and, on the other, because we will be able to decompose the three-dimensional boundary layer equation into two two-dimensional ones. One of them is the cross flow, which we solved already in part two, and the second one is the longitudinal flow, the two-dimensional Laplace equation, which has to be solved additionally. Due to this decomposition, we will be able to use the optimization results from part two and have to calculate only the values for the corresponding longitudinal Navier constant, and hereby the tangential drag force given by

$$\left(\mathcal{F}_{\text{t}}^{\text{eff}}\right)_1 = \frac{\nu}{L_3} \frac{1}{1 - \frac{\varepsilon}{L_3} C_{||}^{\text{bl}}} U_1$$

and

$$\left(\mathcal{F}_{\text{t}}^{\text{eff}}\right)_2 = \frac{\nu}{L_3} \frac{1}{1 - \frac{\varepsilon}{L_3} C_{\perp}^{\text{bl}}} U_2.$$

$C_{||}^{\text{bl}}$ and $C_{\perp}^{\text{bl}}$ are the entries of the Navier matrix M, the so called longitudinal and cross Navier constant. The contribution to the drag reduction will be much higher in the three-dimensional case because the Navier constant from the longitudinal flow will be minimized more than the one from the cross flow.

We conclude the thesis with discussions of the obtained results. We will point out the reduced complexity of our numerical calculations due to the application of homogenization. We will justify the advantages of the chosen parametrization, methods and routines, and will discuss the results obtained in both simulations, the direct and the one on the homogenized model, in detail. We will close with an outlook for future projects.

Acknowledgements

My scientific work came into being under the influence of several persons:

I would like to express my deep gratitude to Prof. Willi Jäger for selecting such an interesting subject and leaving it trustfully in my hands. It was a great process of learning for me to have the freedom of shaping a scientific work independently which would not have been possible without his encouragement and financial support.

The results obtained in this thesis can be seen as a consequence of previous works on flows over porous media or over rough boundary of Prof. Willi Jäger together with Prof. Andro Mikelić from the University of Lyon. I am indebted to Prof. Andro Mikelić who had time for friendly discussions whenever he was in Heidelberg and who answered questions even from abroad.

I would like to thank the German Research Council (DFG) and Prof. Georg Bock for their financial support within the International Graduiertenkolleg IGK 710 "Complex processes: Modeling, Simulation and Optimization".

Thanks to this organization a joint work came into existence with Prof. Rolf Rannacher whom I want to thank for his interest and for the opportunity he gave to me to validate the homogenized model and to complete the work with additional calculations.

Most of my numerical knowledge I learned practically spending time with Dr. Nicolas Neuss. I would like to thank him for the calculations, for all modifications he immediately implemented, for helping me getting along with his program package and for his critical corrections.

Many thanks to Eberhard Michel who was always ready for scientific discussions. Thanks for reading and corrections and good look for your own work.

Thanks to Thomas Richter for the calculations.

Thanks to the system administrators of IWR and Applied Analysis, especially Markus Ridinger, Cristian Croitoru and Eberhard Michel, thanks to the secretaries, especially Elke Pietschmann, Ina Scheid, Ria Lynott and Astrid Sudmann, and thanks to my colleagues who provided me a pleasant environment during this work.

No words can express my gratefulness to my family for their support during all the years of my studying and their encouragement: I would like to thank my parents especially for

their daily help with my son Felix in the last three years. Thanks for moving to Leimen in order to make it possible for me to spend enough time for science. Many thanks to my husband Martin for his love, for the comfortable atmosphere at home, for his support and for taking some of his short free time to read my thesis. I would like to thank Felix. He learned me to use my time efficiently. His cordially welcoming makes me forget every unsolved problem bothering me. Last but not least I would like to thank my daughter who is supposed to be born in the end of November. She was the motivating factor for finishing this thesis. I can not answer the question who keeps whom awake at night but I hope that I do not stress her too much.

Chapter 1

Modeling of flow over 2D rough surfaces

1.1 Rough surfaces and their industrial importance

It is well known, that the golf ball would never fly as far as it does with a smooth surface instead of the dimpled one. Taking a closer look to the surface we see that the indentations in the center are slightly deeper than those at the poles. This simple design with its proper backspin helps the ball flying farther and we can conclude: A rough surface can have a lower drag than a smooth one.

During the last decade we could observe an increasing scientific interest in fluid dynamic effects caused by biological surfaces. The two most well-known examples are lotus leaves and shark skin. In both examples microstructures on the surface play an important role. The perfect cleaning characteristic of the lotus leaf, discovered by Abramson, Barthlott and co-workers (see [6], [7]), works only due to a certain surface microstructure, whereby impurity particles have a reduced contact area so that the water droplets can easily overcome the difficulty of releasing them from the surface. The microscopic wax crystals on the leaf surface lead to an extremely low surface energy, so that the particles are bound to the water droplet surface (see Figure 1.1.3). How microstructures on shark skin reduce drag was first pointed out by Walsh in [58], Bechert, Hoppe and Reif in [11] after the detailed examination of the skin structure of sharks by Reif and Dinkelacker (see [53]). But also today shark skin is of great interest in the modern technological biology. This is pointed out in Nachtigalls book 'Bionik' ([43]). In a reacent BMBF project (see [36]) researches from the University of Bremen presented their idea to reduce costs of shipping companies by using shark skin as bio-antifouling. The natural cover on the boat's hull consists of shells and barnacles which increase the drag of the boat significantly and destroy its painting very fast. They found out that coating with an artificial shark skin reduces this fouling about 70% and hereby an drag reduction of 15% is obtained.

As sharks belong to one of the oldest species in nature they have optimized their shape for more than 200 million years, i.e. they evolved such that they minimize their energy consumption during movement, they reduce drag. On the skin of fast swimming sharks tooth-like microstructures called dermal denticles ('tiny skin teeth') were found (see Figure

1.1.4). They are between 0.1 and a few millimeters high and typically have a broad basal plate, a narrow stalk and a broad ridged crown. From [39] we know that dermal denticles are built on the same high level engineering principles as the most durable materials nowadays, such as fiberglass. This principle concerns the embedding of a hard material inside a softer one, this technique combines the best properties of both, rigidity without brittleness and plasticity without distortion. Here, these two materials are apatite, a hard crystalline mineral, which is embedded in collagen, a soft protein. Due to these components dermal denticles are as hard as granite and as strong as steel but are anchored elastically. Globally seen they have a mushroom like shape with tips on one side pointing towards the shark tail, which is why a shark feels relatively smooth if stroked from head-to-tail, but sand-papery coarse if stroked the other way. The crowns of the dermal denticles on fast swimming sharks are smooth and almost ridgeless on the tip of the snout and leading edges of the fins, but elsewhere on the body they have ridges with depths one-half to two-thirds their width. The crowns overlap tightly and the alignment of these ridges on their top varies along the body, they form a path of least flow resistance over the surface, a streaky structure in the downstream direction (see figure 1.1.5). Speaking about microstructures from now on we refer only to those ridges on the crown and do not consider the whole dermal denticles because there is no fluid circulation between them. The scales are tiny (0.01–0.1mm) and their number is between 3 and 7 ridges on one denticle of a fast shark. The lateral spacing of the ridges is between 0.035–0.1mm. Calculated with the body length, the Reynolds number of fast sharks is high ($\mathrm{Re} \approx 10^6 - 10^7$). Different laboratories (NASA, DLR) tested artificial surfaces with this kind of scales in a turbulent boundary layer, and they found a drag reduction of about 7%. A fluid dynamical explanation is given by many authors: The most important theory says that the alignment of crown ridges with the 'natural' flow direction of water over the shark's body can be expected to maximize drag reduction by reducing turbulence, preventing eddy formation or dampening them. The results of our research stays in agreement with this theory. Bone has suggested in [17] that the ridges work like longitudinal vortex generators which enhance mixing in the turbulent boundary layer and keep the flow attached there. This second theory is exactly the opposite one than the one mentioned above. Enhanced mixing means an increasing shear stress. In this case drag reduction is obtained only due to avoiding flow separation. This is also one of the tricks behind the dimples in the golf ball. But here we have to consider the whole structure of the dermal denticle at an angle of attack and not only the scales on their crown which together form the riblets and a turbulent boundary layer which can not be considered in analysis of flow until now. It is also assumed, that the scales on the shark skin are elastically anchored on the skin of living sharks, which can not be established on a dead piece of shark skin. But it has been shown experimentally that an increasing angle of attack enhances mixing and thus delays the flow separation. Another theory is that low speed streaks of the viscous sublayer occur in regions of low pressure, and this low pressure is utilized to inject fluid through the slits between the scales in the downstream direction. This theory has been analyzed and tested successfully especially for aircraft wings in order to delay the separation of the boundary layer (see [9]). We will not consider flow separation in this thesis. Another utility for fluid dynamical drag reduction in water is of course the production of mucus of bony fish (see [28]). But sharks produce less mucus than other fishes, so we will not pay any attention to this fact in this work.

Pictures from http://www.botanik.uni-bonn.de/system/bionik.htm

Figure 1.1.1: *Nelumbo nucifera,the holy lotus flower, the symbol of purity.*

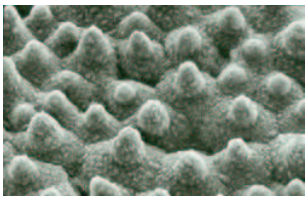

Figure 1.1.2: *Selfcleaning process: combination of microstructure and nanostructure of wax crystals.*

Figure 1.1.3: *The impurities attach to the water surface.*

How strategic roughness yield aero- and hydrodynamic benefits is a great deal of research nowadays. This new technique is used also by airplanes, ships and swimming suits to reduce drag. The grooves must be very closely spaced to obtain the drag reducing effect.

Turbulent shear stress reduction of 7-8% below the value of smooth surfaces has been demonstrated in several laboratories: The NASA developed a thin film, where riblets had been molded for the coating of means of transportation like airplanes and ships. This film was produced by the company 3M. The results from testing on the surface of an Airbus A340 assure a drag reduction of 7–8% after coating only 75% of the surface due to technical reasons. This 8% drag reduction involved a fuel saving of 2.4 tons per flight which is 3% of the total consumption, which amounts to either a cost saving or a better profit provided by increasing the number of passengers by 15. A ship called 'Stars and Stripes' which took part in America's Cup in 1987 was also coated with this film. After this ship won the Cup there were a lot of discussions concerning the rules, and they become stricter afterwards. Generally in sports surface microstructures are becoming more and more important. The company Speedo produces a swimmer suit called 'Fast Skin' which imitates the shark skin. Different tests provided that this suit is 7.5% faster than other suits tested and has 3% lower surface resistance. The imitated shark skin suit could also be interesting for cycling, skiing and other sports.

Of course, a direct application like the one on airplanes is not easy. There are a lot of difficulties to overcome: for the application of the thin film on the surface of an airplane the airplane has to be on the ground which means a decrease in profit for the company, due to the film an inspection of the airplane can be difficult, a small crack under the film can hardly be discovered, the effects of contaminations have to be checked and the film must be renewed after 2–3 years. Due to these difficulties this attempt failed, but the interest in microstructures is high and it remains a task to better understand their function and also their manufacturing (polymer films) (see [40]). Since 2002 a new technique in producing such kind of microstructures on aircraft wings is taken into account: perforated aircraft wings where millions of tiny holes are drilled in the leading edges of the wing. Researchers at Heriot-Watt University and the aerospace company BAE SYSTEMS have carried out

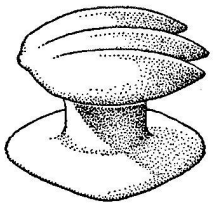

Figure 1.1.4: *Microstructure on the shark skin (see [56]).*

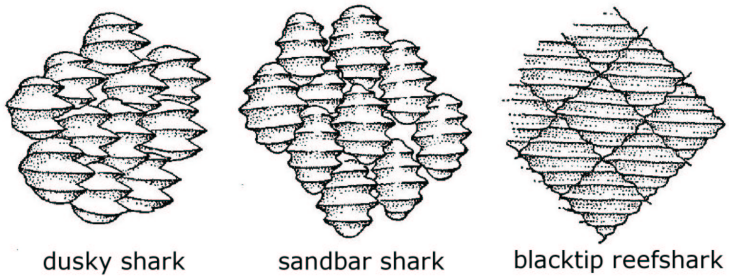

Figure 1.1.5: *Together the microstructures from the shark skin form a striped structure in the stream line direction(see [56]).*

the studies on drilling such holes using laser beams.

In this thesis we will focus on how the shape of microstructures should look like to reduce skin friction. Drag reducing mechanisms derived from shark skin have been considered e.g. by Bechert, Bartenwerfer, Hoppe and Reif in [8]. They claim the microstructures which give a drag reduction of about 7–8% below the smooth surface, which are also used in the examples mentioned above, are small longitudinal riblets. The dimension of the spacing and height are comparable to the dimensions of the viscous sublayer of a turbulent boundary layer. These tiny riblets are also found on all species of fast sharks.

How do the microstructures work? There are small streamline vortices in the viscous sublayer of a turbulent boundary layer, which produce a local upwash of slow fluid away from the surface and the other way around. These longitudinal vortices are responsible for the streaky structure of the boundary layer and thus for the production of low speed streaks. The streaky structure of the viscous boundary layer shows that the velocity profile is highly unstable and this causes the high fluctuations in the layer above. The vortices are also responsible for the momentum exchange and thus for turbulent skin friction. The development of these longitudinal vortices requires cross-flow in the viscous sublayer. To reduce the turbulent skin friction Bechert found out in [11] that one has to hamper the cross-flow in order to decrease turbulent mixing and turbulent shear stress, and this happens if the spacing of the riblets is small enough and if the ridges have sharp edges.

Whereas the authors of [8] build on a theory of the viscous Couette type flow on surfaces

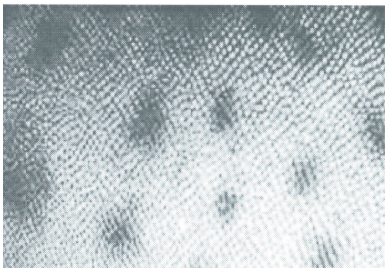

Figure 1.1.6: *The shark skin of spiny dogfish or bramble shark, a slower swimmer (see [33]).*

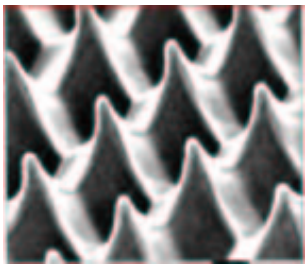

Figure 1.1.7: *Artificial skin produced with laser technology.*

with small longitudinal riblets of different shapes, including sawtooth, blade-like, scalloped and convex riblet cross sections, we will calculate the optimal shape of periodically distributed riblets using the approximation theory of the oscillating viscous Couette flow due to the theory of homogenization developed by Jäger and Mikelić in [33].

1.2 The viscous sublayer in two dimensions

To model the flow over small microstructures on the surface of a swimming body we consider at first the so-called boundary layer of a turbulent flow which consists of the flow within a thin layer. According to the theory of Schlichting, a turbulent boundary layer consists of three parts, a viscous sublayer, which is relative small ($y^+ \leq 5$, where $y^+ = \frac{x_2}{\delta}$ is the characteristic wall coordinate), the buffer layer ($5 < y^+ < 20$), and the logarithmic or overlap layer ($y^+ > 20$). It is assumed that in each sublayer the velocity of the flow is described by a different profile: In the viscous one where $U \sim \sqrt{\nu}$ the profile is linear, and in the logarithmic layer a logarithmic profile $u^+ = \frac{1}{\kappa}\ln(y^+) + C^+$ is used, where $u^+ = \frac{\bar{u}}{v}$ is the rescaled velocity, $\bar{u}$ the mean velocity in the pure viscous layer and C^+ is a characteristic constant ($C^+ = 5$ for the smooth wall). The riblets used on the surface of aircrafts extend into the buffer layer. Their height is about $h = 15\delta$, where δ is the thickness of the viscous sublayer. With this kind of riblets a drag reduction of about 8-10% was obtained in the experiments. To consider the analysis of flow in the buffer layer is out of reach until now. In this thesis we have to restrict ourselves to riblets that remain in the viscous sublayer of the turbulent boundary layer, which means they

are about 15 times smaller than the riblets used on the aircraft.

Prandtl already introduced the notion of boundary layer in 1904. He divided the flow surrounding a body in two domains: a layer subject to friction in the neighborhood of the body and a frictionless region outside of this layer.

A special property of this boundary layer is that under some circumstances reverse flow occurs in the immediate proximity of the surface. Then, in connection with this reverse flow, a separation of the boundary layer takes place together with a more or less strong formation of vortices in the flow behind the body. This change in pressure distribution gives rise to the form drag. The boundary theory therefore offers an approach to the calculation of this form drag. It is believed that riblets delay this flow separation and thus minimize turbulent drag, but we will not consider this issue in this thesis.

The flow in this viscous sublayer of thickness δ is the same flow considered between two parallel plates with a distance δ from each other, where the lower plate is kept fix and the upper one moves with velocity U uniformly and parallel to the lower one. Due to this parallel moving the transverse velocity component in y-direction is equal to zero. Because of the adherence of the fluid to the surfaces a linear velocity distribution between the two plates, the so-called Couette flow, describes the model. A flow where no transverse velocity occurs is called simple shear flow. The shear stress is given by the ratio

$$\tau = \frac{\text{tangential force}}{\text{area}} = \frac{\mathcal{F}_t}{A} = \mu \frac{du}{dy},$$

where μ is the dynamic viscosity, $\nu = \frac{\mu}{\varrho}$ the kinematic viscosity and ϱ is the density of the fluid. For our model, for water, $\nu = 1.01 \times 10^{-6} m^2/s$. The dimensionless Reynolds number is given by

$$\text{Re} = \frac{\text{inertia force}}{\text{friction force}} = \frac{U\delta}{\nu} = \frac{\varrho U \delta}{\mu}.$$

Inserting the data for our model: $\varrho_{\text{water}} = 10^3 kg/m^3$, $\mu = 10^{-3}$ Pas, the size of the viscous sublayer being $\delta \sim \sqrt{\nu} = 10^{-3}$ m and the shear velocity $|U| = \sqrt{\frac{\tau}{\varrho}} = 10^{-3}$, we calculate the Reynolds number of our model which in this case is Re=1. The boundary layer thickness and the velocity component parallel to the surface are independent of x, they do not vary along the wall.

Another characteristic measure for the boundary layer is the ratio between displacement thickness δ^* and momentum thickness ϑ. The first variable is a size for the deflection of the stream lines from the surface by the boundary layer and the second one measures the momentum loss in the boundary layer,

$$\frac{\delta^*}{\vartheta} = 2.218.$$

The drag consists of the contribution of the pressure drag (form drag) and the surface friction drag. The pressure drag, also called form drag, is caused by the difference between the front and rear of the body. The amount of this drag depends on the size and shape of its object. If the shape is streamlined, i.e. the flow is allowed to decelerate along its back part, then the boundary layer is prevented or delayed in separating from the object. This

decreases the pressure drag. But this depends of course also on the size of the object. On a very big object flow separation occurs even if the shape is streamlined. If the shape is not streamlined, then purposely situated so called 'vortex generators' (microstructures) cause the boundary layer to be turbulent. This keeps the energy level high and reduces the risk of flow separation. Compared with the amount of pressure drag, the skin friction is only a small percentage of the total drag. It occurs because of the viscosity of the fluid and is created within the boundary layer. Its amount is obtained by integrating the wall shear stress over the entire surface. We conclude pointing out that a turbulent boundary layer causes more skin friction than a laminar one, but the reduction in pressure drag is much greater (golf ball).

In this thesis we model only the viscous sublayer of a turbulent flow over a rough surface, that means we analyze only the local effect of microstructures on the skin friction which we want to reduce by finding the optimal shape of these microstructures. We do not consider flow separation and do not consider the form drag.

Our model (see figure 1.3.8) describes a two dimensional channel $P = (0, L_1) \times (0, L_2)$ of height of the viscous sublayer $L_2 = \delta = 10^{-3}$ m with a rough surface bottom, the so-called layer of roughness $\mathcal{R}^\varepsilon = (\cup\varepsilon(Y + (k_1, -b_2))) \cap ((0, L_1) \times (-\varepsilon b_2, 0))$ which consists of the periodically repetition of one cell of roughness $Y = \{y \in Z = (0, b_1) \times (0, b_2) \mid b_2 > y_2 > \max\{0, \gamma(y_1)\}\}$. The rough boundary is denoted by $\mathcal{B}^\varepsilon = \varepsilon(\cup\gamma + (k_1, -b_2))$ and describes periodically distributed humps of characteristic length and amplitude. The domain where the fluid flows is thus given by $\Omega^\varepsilon = P \cup \Sigma \cup \mathcal{R}^\varepsilon$. The flow itself can be described with the incompressible steady state Navier-Stokes equations with a Couette Flow profile (Re=1) with Dirichlet boundary conditions on the rough boundary, the so-called no-slip condition:

$$\begin{cases} -\nu\Delta v^\varepsilon + (v^\varepsilon\nabla)v^\varepsilon + \nabla p^\varepsilon &= 0, \text{ in } \Omega^\varepsilon \\ \text{div } v^\varepsilon &= 0, \text{ in } \Omega^\varepsilon \\ v^\varepsilon &= 0, \text{ on } \mathcal{B}^\varepsilon \\ v^\varepsilon &= U, \text{ on } \Sigma_2 \\ \{v^\varepsilon, p^\varepsilon\} &- x_1 \text{ periodic.} \end{cases} \tag{1.2.1}$$

Proposition 1.2.1. If $|U|L_2 < 2\nu$, there is a solution $\{v^\varepsilon, p^\varepsilon\} \in H^2(\Omega^\varepsilon) \times H^1(\Omega^\varepsilon)$ of (1.2.1).

The proof can be found in [33], where it is done for the general case of three dimensions.

To calculate the solution $\{v^\varepsilon, p^\varepsilon\}$ of this system numerically is difficult. Because of the rough boundary we need a huge amount of data and a very fine mesh to capture the rough boundary as exact as possible. To reduce the numerical effort we first apply homogenization, where the rough boundary is replaced by a smooth artificial one with new boundary conditions as proposed by Jäger and Mikelić in [33], the so-called Navier slip condition. This Navier slip condition is obtained by the authors constructing an asymptotic expansion with help of so-called boundary layer correctors. A similar ansatz was presented

before by O. Pironneau in [2] for high Reynolds numbers, but only a numerical validation was given. The new equations on the smooth domain, the so-called effective equations, are calculated by the authors as a limit process, where the characteristic length ε tends to zero. We will use the results from [32] and [33] in order to approximate our oscillating system (1.2.1) in the next section.

1.3 Homogenization applied to the incompressible steady state Navier-Stokes equation in the viscous sublayer

In this section we briefly describe the process of homogenization applied to the incompressible steady state Navier-Stokes equation. As mentioned before this process has been studied in detail by Jäger and Mikelič in [33].

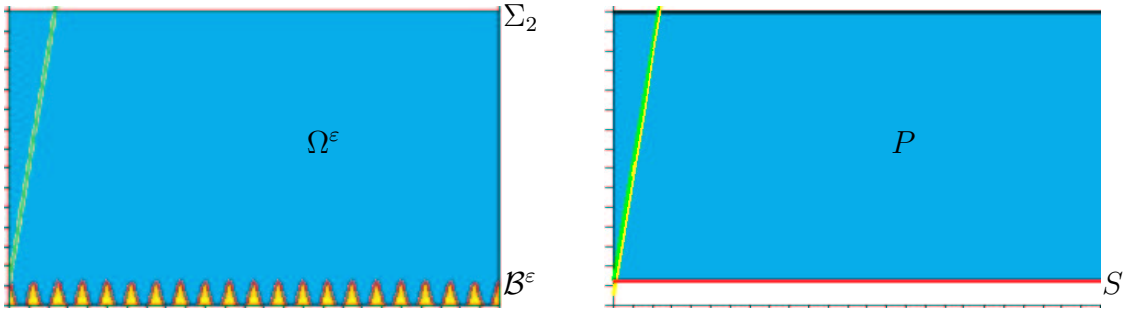

Figure 1.3.8: *Visualization of the process of homogenization.*

In figure 1.3.8 we explain geometrically the process: The left picture shows the rough channel filled with water. With red we mark the rough boundary, with yellow the solid part of the microstructure and the green line indicates the linear profile of the Couette flow given by the boundary condition U at the upper boundary and by zero on the top of the microstructure. Doing homogenization we replace this complicated structure with a simple one shown in the right picture where the red line represents the artificial smooth boundary S on which the new boundary conditions which describe the influence of the roughness have to be determined. It is clear that we will have no zero boundary condition on S that means that our velocity profile differs from the left one. The new profile is the yellow line and the green one represents v_0, the Couette flow in P with the no-slip condition on S. In the case where S is situated directly on the top of the microstructures the two green lines from both figures coincides. How the new profile is constructed will be explained in the next steps.

The Couette flow in P, satisfying the no-slip condition at Σ, is given by

$$v^0 = \frac{Ux_2}{L_2}, \qquad p^0 = 0.$$

If $|U|L_2 < 2\nu$ then v^0 is unique. This is true in our case, because $Re = 1 < 2$. The idea of the authors was to extend the velocity v^0 to $\Omega^\varepsilon \setminus P$ by zero and to construct the solution

of (1.2.1) as a small perturbation to this Couette flow. They present a convergence result and the error estimates for the approximation. Let us emphasize the important results:

Theorem 1.3.1. Let $|U|L_2 < 2\nu$ and let

$$R_0 = \frac{\nu}{L_2}\frac{|U|}{\nu - \frac{L_2|U|}{2}}\sqrt{L_1 b_2}$$

Then for $\varepsilon < \frac{L_2}{b_2}$ the problem (1.2.1) has a solution $\{v^\varepsilon, p^\varepsilon\} \in H^2(\Omega^\varepsilon)^2 \times H^1(\Omega^\varepsilon)$, εb_1 - periodic in x_1 and satisfying

$$||\nabla(v^\varepsilon - v^0)||_{L^2(\Omega^\varepsilon)^4} \leq R_0\sqrt{\varepsilon}$$

Moreover,

$$||v^\varepsilon||_{L^2(\Omega^\varepsilon \setminus P)^2} \leq \frac{b_2}{\sqrt{2}} R_0 \varepsilon\sqrt{\varepsilon}$$

$$||v^\varepsilon||^2_{L^2(\Sigma)} \leq 2^{\frac{1}{4}}\sqrt{b_2} R_0 \varepsilon$$

$$||p^\varepsilon - p^0||_{L^2(P)} \leq C\sqrt{\varepsilon}.$$

Furthermore, the solution is C^∞ in P.

Proof. see [33].

Theorem 1.3.2. Let $|U|L_2 \leq \nu$ and $\varepsilon \leq C(b_1, b_2, L_1)\nu^{\frac{9}{14}}$. Then $v^\varepsilon \in H^2(\Omega^\varepsilon)$, constructed in Theorem 1.3.1, is a unique solution to (1.2.1) and $p^\varepsilon \in H^1(\Omega)$ is unique up to a constant.

Proof. see [33].

The authors obtained the uniform a priori estimates for $v^\varepsilon, p^\varepsilon$ which we do not want to mention here again. We recommend [32] and [33] to the reader. We just point out here that they have found that Couette's flow v^0 is an $\mathcal{O}(\varepsilon^{\frac{3}{2}})$ approximation of v^ε in $L^2(P)$, where:

$$v^\varepsilon = v^0 - \varepsilon\beta^{\text{bl}}\Big(\frac{x}{\varepsilon}\Big)\frac{\partial v_1^0}{\partial x_2} + \varepsilon C_{\text{bl}}\Big(\frac{\partial v_1^0}{\partial x_2}e_1 + d^1\Big)H(x_2) + O(\varepsilon^2), \tag{1.3.1}$$

and where d^1 corresponds to the counterflow generated by the boundary condition on the artificial interface, and, restricted to S, an $\mathcal{O}(\varepsilon)$ approximation of $v^\varepsilon|_S$ in $L^2(S)$:

$$\frac{\partial v_1^\varepsilon}{\partial x_2} = \frac{\partial v_1^0}{\partial y_2}\Big(1 - \frac{\partial \beta_1^{\text{bl}}}{\partial y_2}\Big) + O(\varepsilon)$$

$$\frac{1}{\varepsilon}v_1^\varepsilon = -\frac{\partial v_1^0}{\partial y_2}\beta_1^{\text{bl}}(\frac{x}{\varepsilon}) + O(\varepsilon).$$

After averaging these equations on S and neglecting higher order terms the familiar form of the Navier slip condition is found:

$$u^{\text{eff}} = -\varepsilon C_{\text{bl}}\frac{\partial u_i^{\text{eff}}}{\partial x_2}.$$

To calculate the effective coefficient in this wall law, the Navier constant, the approaches from [30] and [31] were followed.

The solution $\{v^\varepsilon, p^\varepsilon\}$ was constructed formally as an asymptotic expansion which is shown in (1.3.1). For a better understanding we have to explain briefly the terms in this expansion: the first one is the Couette flow, the second term is the first order boundary layer correction to obtain the correct boundary condition on the artificial smooth boundary S. This correction is a constant of order ε. This means that the linear profile is shifted to the right by this amount which gives the wrong boundary condition on the upper boundary where the velocity U is prescribed. To correct this boundary condition we have to add the third term which contains the counter flow and the resulting profile is again a linear one with a lower origin.

In the homogenization process we are interested in the limit of this oscillating solution for $\varepsilon \to 0$. Here we will not specify in what kind of limit process we are interested, the details can be found in [33] or in the literature ([3], [16], [20], [27]). The limit equations, the so-called effective equations, are obtained due to this limit process where the asymptotic expansion of v^ε is inserted in the equations and the limit process is executed. It is clear that in P, far away from the irregularities, the flow will not be influenced much. It will still be governed by the incompressible steady state Navier-Stokes system. The presence of the irregularities will only contribute to the effective boundary conditions at the artificial smooth boundary S. This contribution is found exactly in the Navier slip condition, in the coefficient C_{bl}, the so-called Navier constant. This constant is calculated using an auxiliary boundary layer equation solved by $\{\beta^{\mathrm{bl}}, \omega^{\mathrm{bl}}\}$ which will be given in the next section.

The effective Couette Navier flow is given by:

$$\begin{cases} -\nu\Delta u^{\mathrm{eff}} + (u^{\mathrm{eff}}\nabla)u^{\mathrm{eff}} + \nabla p^{\mathrm{eff}} &= 0, \text{ in } P \\ \text{div } u^{\mathrm{eff}} &= 0, \text{ in } P \\ u^{\mathrm{eff}} &= (U_1, 0), \text{ on } \Sigma_2 \\ u_1^{\mathrm{eff}} &= -\varepsilon C_{\mathrm{bl}} \frac{\partial u_i^{\mathrm{eff}}}{\partial x_2}, \text{ on } S \\ u_2^{\mathrm{eff}} &= 0, \text{ on } S \\ \{u^{\mathrm{eff}}, p^{\mathrm{eff}}\} \quad x_1 &- \text{ periodic,} \end{cases} \tag{1.3.2}$$

where P is the rectangle where the fluid flows, the viscous sublayer in two dimensions, Σ_2 is the upper boundary, where the flow velocity reaches the value U, and S is the lower boundary of P, the so-called artificial smooth boundary, where the Navier slip condition holds (see figure 1.3.8).

Proposition 1.3.3. If $|U|L_2 < 2\nu$, there is a unique solution of (1.3.2):

$$\begin{cases} u^{\mathrm{eff}} &= (U + (\frac{x_2}{L_2} - 1)(1 - \frac{\varepsilon}{L_2} C_{\mathrm{bl}})^{-1} U, 0), \quad x \in P \\ p^{\mathrm{eff}} &= 0, \quad x \in P. \end{cases}$$

Proof. see [33].

Further we would like to replace the oscillating solution $\{v^\varepsilon, p^\varepsilon\}$ by the effective one $\{u^{\text{eff}}, p^{\text{eff}}\}$. Therefore the following error estimates hold:

Corollary 1.3.4. Under the assumptions of theorem 1.3.1 we have

$$||\nabla(v^\varepsilon - u^{\text{eff}})||_{L^1(P)} \leq C\varepsilon,$$

$$\sqrt{\varepsilon}||v^\varepsilon - u^{\text{eff}}||_{L^2(P)} + ||v^\varepsilon - u^{\text{eff}}||_{L^1(P)} \leq C\varepsilon^2.$$

1.4 The shape optimization problem

In this thesis we want to analyze the effect of the microstructures on the drag. As mentioned before, the drag consists of two parts, the drag form and the skin friction. We focus our attention to the skin friction, and suppose that a uniform pressure gradient is maintained in the longitudinal direction in the channel. Under these assumptions the normalized tangential drag force on S is given by

$$\mathcal{F}_{\text{t}}^\varepsilon = \frac{1}{L_1}\int_S \nu n \cdot \sigma \cdot e_1 dx_1,$$

where $n = e_2$ is the normal vector to S and $\sigma_{ij} = \frac{1}{2}(\frac{\partial u_i}{\partial x_j} + \frac{\partial u_j}{\partial x_i}) - p\delta_{ij}$ is the total stress tensor, consisting of the viscous shear stress, due to viscous forces in the fluid, and of the fluid pressure p. The normalized formula for the drag is then

$$\mathcal{F}_{\text{t}}^\varepsilon = \frac{1}{L_1}\int_S \frac{1}{2}\nu\Big(\frac{\partial}{\partial x_2}u_1^\varepsilon(x_1,0) + \frac{\partial}{\partial x_1}u_2^\varepsilon(x_1,0)\Big)dx_1. \tag{1.4.1}$$

In the last section we have seen that we are able to replace $\{v^\varepsilon, p^\varepsilon\}$ by $\{u^{\text{eff}}, p^{\text{eff}}\}$ in order to reduce the calculation costs. With these effective parameters we take a look at the so-called effective tangential drag force, given by

$$\mathcal{F}_{\text{t}}^{\text{eff}} = \frac{1}{L_1}\int_S \frac{1}{2}\nu\Big(\frac{\partial}{\partial x_2}u_1^{\text{eff}}(x_1,0) + \frac{\partial}{\partial x_1}u_2^{\text{eff}}(x_1,0)\Big)dx_1 = \frac{1}{L_1}\int_S \frac{1}{2}\nu\frac{\partial}{\partial x_2}u_1^{\text{eff}}(x_1,0).$$

The last equation holds because we know that the Couette flow depends only on x_2 and not on x_1.

Now we reached the main issue of this thesis which is to solve the following optimization problem: Find the optimal rough structure $\gamma \in G$, where G is the set of all admissible shapes of microstructures Γ, which we will specify later, such that the effective tangential drag force or the skin friction acting on the artificial smooth boundary S is minimized

$$\min_{\gamma\in G} \quad \mathcal{F}_{\text{t}}^{\text{eff}} = \frac{1}{2L_1}\int_S \nu\frac{\partial}{\partial x_2}u_1^{\text{eff}}(x_1,0)dx_1,$$

and u^{eff} is calculated from the effective Navier-Stokes flow which models the flow in the viscous sublayer of a turbulent flow:

$$\begin{cases} -\nu\Delta u^{\text{eff}} + (u^{\text{eff}}\nabla)u^{\text{eff}} + \nabla p^{\text{eff}} &= 0, \text{ in } P \\ \text{div } u^{\text{eff}} &= 0, \text{ in } P \\ u^{\text{eff}} &= (U_1, 0), \text{ on } \Sigma_2 \\ u_1^{\text{eff}} &= -\varepsilon C_{\text{bl}} \frac{\partial u_i^{\text{eff}}}{\partial x_2}, \text{ on } S \\ u_2^{\text{eff}} &= 0, \text{ on } S \\ \{u^{\text{eff}}, p^{\text{eff}}\} \quad x_1 &- \text{ periodic.} \end{cases}$$

If we insert the solution of the effective Couette flow from Proposition 1.3.3 in the formula for the effective tangential drag, we get

$$\mathcal{F}_{\text{t}}^{\text{eff}} = \frac{\nu}{2} \frac{U}{L_2 - \varepsilon C_{\text{bl}}}, \tag{1.4.2}$$

which means that our optimization problem depends only on the Navier constant $C_{\text{bl}} = -\int_{Z^{\text{bl}}} |\nabla\beta^{\text{bl}}(x_1, 0)|^2 dx$ which is defined by the solution of the auxiliary boundary layer problem β^{bl} (see (1.4.3)). This boundary layer problem describes the concentration of the changes of the velocity and pressure field around the interface S and their rapidly decay with increasing distance from S.

Considering the tangential drag force corresponding to the effective velocity u^{eff} instead of the oscillating skin friction, we make following approximation error:

Theorem 1.4.1. Let the skin friction $\mathcal{F}_{\text{t}}^{\varepsilon}$ be defined by (1.4.1). Then we have

$$|\mathcal{F}_{\text{t}}^{\varepsilon} - \mathcal{F}_{\text{t}}^{\text{eff}}| \leq C\varepsilon^2 \frac{U^2}{\nu L_2}(1 + \frac{\nu}{L_2 U}).$$

Proof. see [33].

The formula (1.4.2) is of great importance to the theory of flows over rough surfaces. It says that the presence of any periodic roughness diminishes the tangential drag, because C_{bl} is negative and thus $\{I - \frac{\varepsilon}{L_2} C_{\text{bl}}\}^{-1} < I^{-1}$.

Being able to solve the effective equations analytically, we can do a few simplifications which have a significant impact on our optimization problem. As we see in (1.4.2), our calculation are reduced to the determination of the so-called Navier constant C_{bl}. In our resulting optimization problem we only need to solve the boundary layer equation, no longer the Navier-Stokes equation, which is of less computational effort. The optimization problem reads as follows:

$$\min_{\gamma \in \text{G}} \quad \text{C}_{\text{bl}} = -\int_{\text{Z}^{\text{bl}}} |\nabla\beta^{\text{bl}}(\text{y})|^2 \text{dy}$$

subject to the boundary layer equations

$$\begin{cases} -\Delta\beta^{\mathrm{bl}} + \nabla\omega^{\mathrm{bl}} &= 0, \text{ in } Z^+ \cup Y \\ \operatorname{div}\ \beta^{\mathrm{bl}} &= 0, \text{ in } Z^{\mathrm{bl}} \\ \left[\beta^{\mathrm{bl}}\right]_S(\cdot,0) &= 0, \text{ on } S \\ \left[\{\nabla\beta^{\mathrm{bl}} - \omega^{\mathrm{bl}} I\}e_2\right]_S(\cdot,0) &= e_1, \text{ on } S \\ \beta^{\mathrm{bl}} &= 0, \text{ on } \Gamma \\ \{\beta^{\mathrm{bl}}, \omega^{\mathrm{bl}}\} \quad x_1 &- \text{ periodic,} \end{cases} \tag{1.4.3}$$

where $S = (0,1)$, $Z^+ = (0,1)\times(0,\infty)$, and $Z^{\mathrm{bl}} = Z^+ \cup S \cup Y$.
The detailed equations are:

$$\begin{aligned} -\tfrac{\partial^2}{\partial x_1^2}\beta_1^{\mathrm{bl}}(x_1,x_2) - \tfrac{\partial^2}{\partial x_2^2}\beta_1^{\mathrm{bl}}(x_1,x_2) + \tfrac{\partial}{\partial x_1}\omega^{\mathrm{bl}} &= 0, \text{ in } Z^+ \cup Y \\ -\tfrac{\partial^2}{\partial x_1^2}\beta_2^{\mathrm{bl}}(x_1,x_2) - \tfrac{\partial^2}{\partial x_2^2}\beta_2^{\mathrm{bl}}(x_1,x_2) + \tfrac{\partial}{\partial x_1}\omega^{\mathrm{bl}} &= 0, \text{ in } Z^+ \cup Y \\ \tfrac{\partial}{\partial x_1}\beta_1^{\mathrm{bl}}(x_1,x_2) + \tfrac{\partial}{\partial x_2}\beta_2^{\mathrm{bl}}(x_1,x_2) &= 0, \text{ in } Z^{\mathrm{bl}} \\ [\beta_1^{\mathrm{bl}}](\cdot,0) = [\beta_2^{\mathrm{bl}}](\cdot,0) &= 0, \text{ on } S \\ [\tfrac{\partial}{\partial x_2}\beta_1^{\mathrm{bl}}](\cdot,0) &= 1, \text{ on } S \\ [\tfrac{\partial}{\partial x_2}\beta_2^{\mathrm{bl}} - \omega^{\mathrm{bl}}](\cdot,0) &= 0, \text{ on } S \\ \beta_1^{\mathrm{bl}} = \beta_2^{\mathrm{bl}} &= 0 \text{ on } \Gamma. \end{aligned} \tag{1.4.4}$$

Let $V = \{z \in L^2_{\mathrm{loc}}(Z^{\mathrm{bl}})^2 : \nabla_y z \in L^2(Z^{\mathrm{bl}})^4;\ z = 0 \text{ on } \Gamma;\ \operatorname{div}_y z = 0 \text{ in } Z^{\mathrm{bl}};\ z\ \ y_1 \text{ - periodic}\}$.
Using test functions from this space we get the following weak formulation of the problem:

$$\int_{Z^+\cup Y} \nabla\beta^{\mathrm{bl}}\nabla\varphi - \int_{\partial(Z^+\cup\bar{Y})} \nabla\beta^{\mathrm{bl}}\varphi n - \int_{Z^+\cup Y} \omega^{\mathrm{bl}} \operatorname{div}\varphi + \int_{\partial(Z^+\cup\bar{Y})} \omega^{\mathrm{bl}}\varphi n = 0 \tag{1.4.5}$$

$$\begin{aligned} \textstyle\int_{Z^+\cup Y} \nabla\beta^{\mathrm{bl}}\nabla\varphi &= \textstyle\int_{Z^+\cup Y} \omega^{\mathrm{bl}} \operatorname{div}\varphi + \int_{\partial Z^+}(\nabla\beta^{\mathrm{bl}} - \omega^{\mathrm{bl}})n\varphi + \int_{\partial\bar{Y}}(\nabla\beta^{\mathrm{bl}} - \omega^{\mathrm{bl}})\varphi e_2 \\ &= -\textstyle\int_S [\{\nabla\beta^{\mathrm{bl}} - \omega^{\mathrm{bl}}\}e_2]\varphi \\ &= -\textstyle\int_S e_1\varphi. \end{aligned} \tag{1.4.6}$$

We are working in the space of divergence free functions, that means that the integral over the whole domain from the right hand side will disappear. For the weak formulation of our problem we get:

$$\beta^{\mathrm{bl}} \in V : \int_{Z^{\mathrm{bl}}} \nabla\beta^{\mathrm{bl}}\nabla\varphi = -\int_S \varphi e_1 \quad \forall\varphi \in V. \tag{1.4.7}$$

Proposition 1.4.2. Problem (1.4.7) has a unique solution $\beta^{\mathrm{bl}} \in V$. Furthermore, there exists $\omega^{\mathrm{bl}} \in L^2_{\mathrm{loc}}(Z^{\mathrm{bl}})$ such that (1.4.7) holds in the sense of distributions. Finally, $\{\beta^{\mathrm{bl}}, \omega^{\mathrm{bl}}\} \in V \cap C^\infty(Z^+ \cup Y)^2 \times C^\infty(Z^+ \cup Y)$.

Proof.

Using the Lax-Milgram lemma there is a unique $\beta^{\mathrm{bl}} \in V$ satisfying (1.4.7), using De Rhams theorem we obtain $\omega^{\mathrm{bl}} \in L^2_{\mathrm{loc}}(Z^{\mathrm{bl}})$, which is unique up to a constant, satisfying (1.4.7). By the elliptic theory the pair $\{\beta^{\mathrm{bl}}, \omega^{\mathrm{bl}}\} \in V \cap C^\infty(Z^+ \cup Y)^2 \times C^\infty(Z^+ \cup Y)$ is the solution of the boundary layer equation (1.4.3).

□

In the next lemma we recall some properties of the solution of the boundary layer equation (1.4.3) from [32] which we will need for further proofs.

Lemma 1.4.3. Any solution $\{\beta^{\mathrm{bl}}, \omega^{\mathrm{bl}}\}$ of (1.4.3) satisfies

$$\begin{aligned}
\int_0^1 \beta_2^{\mathrm{bl}}(y_1, a) dy_1 &= 0, && \forall \quad a \in (0, +\infty); \\
\int_0^1 \omega^{\mathrm{bl}}(y_1, a_1) dy_1 &= \int_0^1 \omega^{\mathrm{bl}}(y_1, a_2) dy_1, && \forall \quad a_1 > a_2 \geq 0; \\
\int_0^1 \beta_1^{\mathrm{bl}}(y_1, a_1) dy_1 &= \int_0^1 \beta_1^{\mathrm{bl}}(y_1, a_2) dy_1, && \forall \quad a_1 > a_2 \geq 0; \\
C_{\mathrm{bl}} = \int_0^1 \beta_1^{\mathrm{bl}}(y_1, 0) dy_1 &= -\textstyle\int_{Z^{\mathrm{bl}}} |\nabla \beta^{\mathrm{bl}}(y)|^2 dy.
\end{aligned} \tag{1.4.8}$$

1.4.1 A rough surface has lower drag than a smooth one

In this subsection we will describe geometrically the Navier constant C_{bl}, will specify where to fix the position of the smooth boundary and will evaluate the drag force for the rough and the smooth configuration. We will be able to prove that the drag is smaller for the rough configuration.

First we do some further simplification of the cost function of our optimization problem which was given as

$$\min_{\gamma \in \mathrm{G}} \quad \mathcal{F}_{\mathrm{t}}^{\mathrm{eff}} = \frac{\nu}{\mathrm{L}_2}(1 - \frac{\varepsilon}{\mathrm{L}_2}\mathrm{C_{bl}})^{-1}\mathrm{U}. \tag{1.4.9}$$

Since the parameters ν, L_2 and U are fixed in the model, we focus our attention only on the expression in the parenthesis. (1.4.9) is equivalent to

$$\max_{\gamma \in G} \quad 1 - \frac{\varepsilon}{L_2} C_{\mathrm{bl}}. \tag{1.4.10}$$

The variable ε is the scaling parameter of the cell problem and remains fix for any height $h \in [0, 1]$ of the microstructure inside the cell. The real height of the microstructure enters in the model through the product of the scaling parameter ε and the height of the microstructure in the macroscopic cell h, εh. (1.4.10) is equivalent to

$$\min_{\gamma \in G} \quad C_{\mathrm{bl}}. \tag{1.4.11}$$

For a fixed shape γ of microstructure, which is given in one single cell of roughness because of the periodicity, we analyze the effect of the height of this microstructure to the cost

function. The results of the calculations for a fix ε, $\varepsilon = 1 \times 10^{-4}$ m, are listed in table 1.4.1. The lower the height h of the microstructure in the cell the lower the value for the Navier constant or the higher its absolute value. The product $\varepsilon \cdot C_{\text{bl}}$ reaches its minimum for the smooth situation, if we consider no microstructures on the shark skin. This means that a thinner fish has lower drag which is well known.

Table 1.4.1: The Navier constant depends linearly on the height of the microstructure.

h	$\varepsilon \cdot C_{\text{bl}}$ $[10^{-4}]$	$\lvert h \cdot C_{\text{bl}} \rvert$ $[10^{-4}]$
0	-1.0	0
0.1	-0.935	0.0935
0.2	-0.850	0.17
0.3	-0.7569	0.22707
0.4	-0.661	0.2644
0.5	-0.5638	0.2819
0.6	-0.4659	0.2795
0.7	-0.3675	0.257
0.8	-0.2689	0.215
0.9	-0.1700	0.153

We want to compare the rough structure with a smooth one. Therefore we have to fix our artificial surface S in the model such that it is always clear where the effective drag is evaluated. We will see later that it makes sense to fix S in the macroscopic model above the microstructures in a distance twice their height. Independent from this, S will always be located at $y_2 = \frac{x_2}{\varepsilon} = 0$, where (y_1, y_2) denote the macroscopic coordinates in the cell and (x_1, x_2) the microscopic coordinates in the realistic model. Removing the whole layer of roughness, we obtain the smooth configuration without any riblets at $y_2 = \frac{x_2}{\varepsilon} = -1$. This smooth structure corresponds to a model for a thinner fish. In the simulations of (1.4.3) we have to situate S always above the boundary Γ such that the boundary conditions can be fulfilled. Mathematically, it is not of interest to compare the rough configuration with a smooth one which models a thinner or a thicker fish. We want to compare a smooth surface, like a wing of an airplane, with the same surface with tiny holes, or the shark skin, where riblets were formed during evolution, with a fish skin without riblets but the same thickness.

The Navier constant, which is calculated by solving the boundary layer equation (1.4.3), describes the distance of the origin of the effective Couette flow to the smooth surface S. It was already shown in [33] that we have freedom in fixing S, a transposition of this interface of order $O(\varepsilon)$ implies a perturbation in the solution of order $O(\varepsilon^2)$. By changing

the position of the smooth boundary the value of the Navier constant and the thickness of the smooth channel P changes. To compare our two configurations, we need to evaluate the effective drag, and therefore to measure the Navier constant C_{bl}, directly on the top of the microstructures. In this case we are interested in the distance between the top of the microstructure and the origin of the effective Couette flow which we will denote by $C_{bl,a}$:

Lemma 1.4.4. Let $h-1 \leq a$, where h is the height of the microstructure and let $\beta^{\mathrm{bl,a}}$ be the solution of the boundary layer problem (see (1.4.3)) with $S = [0,1] \times \{0\}$ replaced by $S^a = [0,1] \times \{a\}$. Then

$$C_{\mathrm{bl,a}} = \int_0^1 \beta^{\mathrm{bl,a}}(y_1, a) dy_1 = C_{\mathrm{bl}} - a.$$

This lemma is a generalization of Lemma 2 from ([32]), where the condition $a > 0$ was posed. In our case, where the height of the microstructure does not reach our artificial smooth boundary, the lemma is also valid for $h - 1 \leq a < 0$.

Proof. From Lemma 1.4.3 we know, that

$$C_{\mathrm{bl,a}} = \int_0^1 \beta^{\mathrm{bl,a}}(y_1, c) dy_1, \quad \forall c \geq a \geq h-1$$

and respectively

$$C_{\mathrm{bl}} = \int_0^1 \beta^{bl,0}(y_1, d) dy_1, \quad \forall d \geq 0.$$

We choose a region $[0,1] \times [c_1, c_2]$, where $h - 1 \leq c_1 \leq a \leq 0 < c_2$, and integrate the first component of the boundary layer equation (1.4.3) over it:

$$\int_0^1 \int_{c_1}^{c_2} \Big[-\frac{\partial^2 \beta_1^{\mathrm{bl}}}{\partial y_1^2} - \frac{\partial^2 \beta_1^{\mathrm{bl}}}{\partial y_2^2} + \frac{\partial \omega^{bl}}{\partial y_1} \Big] dy_1 dy_2 = 0$$

$$\iff \int_{c_1}^{c_2} \Big[-\frac{\partial \beta_1^{\mathrm{bl}}}{\partial y_1}(1, y_2) + \frac{\partial \beta_1^{\mathrm{bl}}}{\partial y_1}(0, y_2) \Big] dy_2$$

$$- \int_0^1 \Big[\frac{\partial \beta_1^{\mathrm{bl}}}{\partial y_2}(y_1, c_2) - \frac{\partial \beta_1^{\mathrm{bl}}}{\partial y_2}(y_1, 0^+) + \frac{\partial \beta_1^{\mathrm{bl}}}{\partial y_2}(y_1, 0^-) - \frac{\partial \beta_1^{\mathrm{bl}}}{\partial y_2}(y_1, c_1) \Big] dy_1$$

$$+ \int_{c_1}^{c_2} \Big[\frac{\partial \omega^{bl}}{\partial y_1}(1, y_2) - \frac{\partial \omega^{bl}}{\partial y_1}(0, y_2) \Big] dy_2 = 0.$$

The first and the third integral of the equation above vanish because of the periodicity. The jump of $\frac{\partial \beta_1^{\mathrm{bl}}}{\partial y_2}(y_1, y_2)$ at the interface S is given by the boundary layer equation by 1. So that we can conclude that

$$\frac{\partial}{\partial y_2} \int_0^1 \Big[\beta_1^{\mathrm{bl}}(y_1, c_2) - \beta_1^{\mathrm{bl}}(y_1, c_1) \Big] = -1,$$

which is equivalent with

$$\frac{\partial}{\partial y_2} \int_0^1 \beta_1^{\mathrm{bl}}(y_1, y_2) dy_1 = -1 \quad \text{for } h - 1 \leq c_1 < y_2 \leq 0,$$

because for $0 \leq y_2 < c_2$ the integral vanishes. Now we are able to set

$$\int_0^1 \beta_1^{\mathrm{bl}}(y_1, y_2)dy_1 = -y_2 + C \quad \text{for } h-1 \leq c_1 < y_2 \leq 0.$$

The constant C we calculate using the definition of C_{bl} as $\int_0^1 \beta_1^{\mathrm{bl}}(y_1, 0)dy_1$. It follows that

$$\int_0^1 \beta_1^{\mathrm{bl}}(y_1, y_2)dy_1 = -y_2 + C_{\mathrm{bl}}$$

and

$$\int_0^1 \beta_1^{\mathrm{bl}}(y_1, a)dy_1 = -a + C_{\mathrm{bl}}.$$

We now take a look at the variational equation of $\beta^{\mathrm{bl,a}} - \beta^{\mathrm{bl}}$:

$$\int_{Z^{bl}} \nabla(\beta^{\mathrm{bl,a}} - \beta^{\mathrm{bl}})\nabla\varphi = -\int_0^1 \varphi_1(y_1, a) - \varphi_1(y_1, 0)$$

and testing with $\varphi = \beta^{\mathrm{bl,a}} - \beta^{\mathrm{bl}}$ we obtain

$$\int_{Z^{bl}} \Big[\nabla(\beta^{\mathrm{bl,a}} - \beta^{\mathrm{bl}})\Big]^2 = -\int_0^1 (\beta_1^{\mathrm{bl,a}}(y_1, a) - \beta_1^{\mathrm{bl}}(y_1, a) - \beta_1^{\mathrm{bl,a}}(y_1, 0) + \beta_1^{\mathrm{bl}}(y_1, 0))$$

$$= -\int_0^1 -\beta_1^{\mathrm{bl}}(y_1, a) - \beta_1^{\mathrm{bl}}(y_1, 0) = -(a - C_{\mathrm{bl}} + C_{\mathrm{bl}}) = -a. \tag{1.4.12}$$

On the other hand

$$\int_{Z^{bl}} \Big[\nabla(\beta^{\mathrm{bl,a}} - \beta^{\mathrm{bl}})\Big]^2 = \int_{Z^{bl}} \nabla(\beta^{\mathrm{bl,a}})^2 + \int_{Z^{bl}} \nabla(\beta^{\mathrm{bl}})^2 - 2\int_{Z^{bl}} \nabla\beta^{\mathrm{bl,a}}\nabla\beta^{\mathrm{bl}}$$

To calculate the last integral we use the variational formulation for $\beta^{\mathrm{bl,a}}$:

$$\int_{Z^{bl}} \nabla\beta^{\mathrm{bl,a}}\nabla\varphi = -\int_{S_a} \varphi e_1.$$

Testing with $\varphi = \beta^{\mathrm{bl}}$ we obtain

$$\int_{Z^{bl}} \nabla\beta^{\mathrm{bl,a}}\nabla\beta^{\mathrm{bl}} = -\int_0^1 \beta_1^{\mathrm{bl}}(y_1, a) = a - C_{\mathrm{bl}}. \tag{1.4.13}$$

From (1.4.12) and (1.4.13) we obtain

$$-C_{\mathrm{bl,a}} - C_{\mathrm{bl}} - 2(a - C_{\mathrm{bl}}) = -a \iff C_{\mathrm{bl,a}} = C_{\mathrm{bl}} - a.$$

□

In our boundary layer cell we fixed the top of the admissible shapes at $y_2 = -0.5$ and the artificial smooth boundary S at $y_2 = 0$. To evaluate the drag directly on the top of the microstructures we have to translate S by 0.5 downwards. For the comparison of the rough structure with the smooth one we obtain the following theorem:

Theorem 1.4.5. The effective tangential drag force measured directly on the tip of the microstructures is given by

$$\mathcal{F}_{\mathrm{t}}^{\mathrm{eff,a}} = \frac{\nu}{2}\,\frac{U}{L_2 - \varepsilon C_{\mathrm{bl}}}.$$

and the tangential drag for the smooth surface in this case is given by

$$\mathcal{F}_{\mathrm{t}}^{\mathrm{smooth}} = \frac{\nu}{2}\,\frac{U}{L_2 + 0.5\varepsilon}.$$

Proof. The effective velocity u^{eff} is a linear function in x_3 and its derivative is constant. If we have to evaluate the integral for the effective tangential drag for different positions of S, we have to consider the change in L_2. In this case L_2 has to be replaced by $L_2 + \frac{1}{2}\varepsilon$:

$$\mathcal{F}_{\mathrm{t}}^{\mathrm{eff,a}} = \frac{\nu}{L_2 + \frac{1}{2}\varepsilon}\Big[1 - \frac{\varepsilon}{L_2 + \frac{1}{2}\varepsilon}C_{\mathrm{bl,a}}\Big]^{-1}U = \frac{\nu}{L_2 + \frac{1}{2}\varepsilon}\Big[1 - \frac{\varepsilon}{L_2 + \frac{1}{2}\varepsilon}(C_{\mathrm{bl}} + \frac{1}{2})\Big]^{-1}U$$

$$\iff \mathcal{F}_{\mathrm{t}}^{\mathrm{eff,a}} = \frac{\nu}{L_2}\Big[1 - \frac{\varepsilon}{L_2}C_{\mathrm{bl}}\Big]^{-1}U.$$

For the smooth plate the same considerations hold: by moving the interface downwards by $\frac{1}{2}\varepsilon$ we have to add this amount to the boundary layer thickness L_2, so we obtain

$$\mathcal{F}_{\mathrm{t}}^{\mathrm{smooth}} = \frac{\nu U}{L_2 + 0.5\varepsilon}.$$

□

The next theorem predicts that a rough surface has a smaller drag and that it is useful to look at a shape optimization problem to minimize it.

Theorem 1.4.6. If we compare the smooth surface with the same surface where holes are drilled in, we can say that

$$\mathcal{F}_{\mathrm{t}}^{\mathrm{eff}} < \mathcal{F}_{\mathrm{t}}^{\mathrm{smooth}}.$$

Proof.

$$\mathcal{F}_{\mathrm{t}}^{\mathrm{eff,a}} = \frac{\nu}{L_2}\Big[1 - \frac{\varepsilon}{L_2}C_{\mathrm{bl}}\Big]^{-1}U < \mathcal{F}_{\mathrm{t}}^{\mathrm{smooth}} = \frac{\nu U}{L_2 + 0.5\varepsilon}$$

$$\iff \frac{1}{L_2 - \varepsilon C_{\mathrm{bl}}} < \frac{1}{L_2 + \frac{1}{2}\varepsilon} \iff -\varepsilon(C_{\mathrm{bl}} + \frac{1}{2}) > 0,$$

which is true because the parenthesis is always negative.

□

For further calculations we keep the height of the microstructure $h = 0.5$ fix and minimize only the Navier constant C_{bl} where ε remains the scaling parameter not to confuse with the height of the microstructure.

1.4.2 Optimal spacing

In this subsection we discuss the effect of spacing of the microstrucures on the skin friction. Therefore we keep the shape and the height of the microstructure fix and compare the skin friction for different spacing. The period of our cell model is fixed by one. We obtain different spacing keeping the height constant using different scaling factors ε (see figure 1.4.11). We have to pay attention to the fact that scaling with a different factor means that also the position of our artificial smooth boundary changes. To obtain comparable numbers for the Navier constant C_{bl} we have to evaluate them at the same position using the formula from lemma 1.4.4

$$\tilde{C}_{\mathrm{bl}} = C_{\mathrm{bl,a}} = C_{\mathrm{bl}} - a,$$

where $C_{\mathrm{bl,a}}$ is the Navier constant evaluated at the position a, where $h - 1 \leq a$, and C_{bl} is the Navier constant evaluated at the position zero ($y_2 = 0$) on the cell model.

We compare the geometries given in figure 1.4.9. Here we have the microscopic representation of the rough bottom of the channel to visualize the different spacing. Here we use the same function to represent $\mathcal{B}^{\varepsilon}$ but with different spacing coefficient τ. The function is:

$$\frac{3}{4} \cdot 10^{-4} \Big[\sin(\tau \frac{2}{3} \cdot 10^4 \pi x + \frac{3\pi}{2}) + 1 \Big].$$

The values for the Navier constants C_{bl} and $\tilde{C}_{\mathrm{bl}}$ are listed in table 1.4.2. We want to compare the skin friction on the same position for all geometries, that means we have to compare the values in the last column.

Table 1.4.2: The Navier constant for different spacing (shape 1).

s	N	$\tilde{C}_{\mathrm{bl}}$	C_{bl}
0.75×10^{-4}	16	-0.519	-0.519
1.5×10^{-4}	16	-0.5353	-0.5353
3×10^{-4}	16	-0.5638	-0.5638
6.0×10^{-4}	32	-0.8043	-0.304
9.0×10^{-4}	48	-0.88	-0.2133

In figures 1.4.10 − 1.4.13 we see the first component of the boundary layer velocity but only in the cell of roughness $(-1, 0) \times (0, 1)$, the lower part of our macroscopic cell model which additionally consists of the domain $Z_1 = (0, 1) \times (0, 1)$ where the first component of the solution of the boundary layer equation stabilizes to a constant value. The coloured region represents the domain Y, the part of the cell of roughness which is filled with fluid. The domains presented here are visualized with the different scaling used to obtain the different spacing of the microstructures with constant heights.

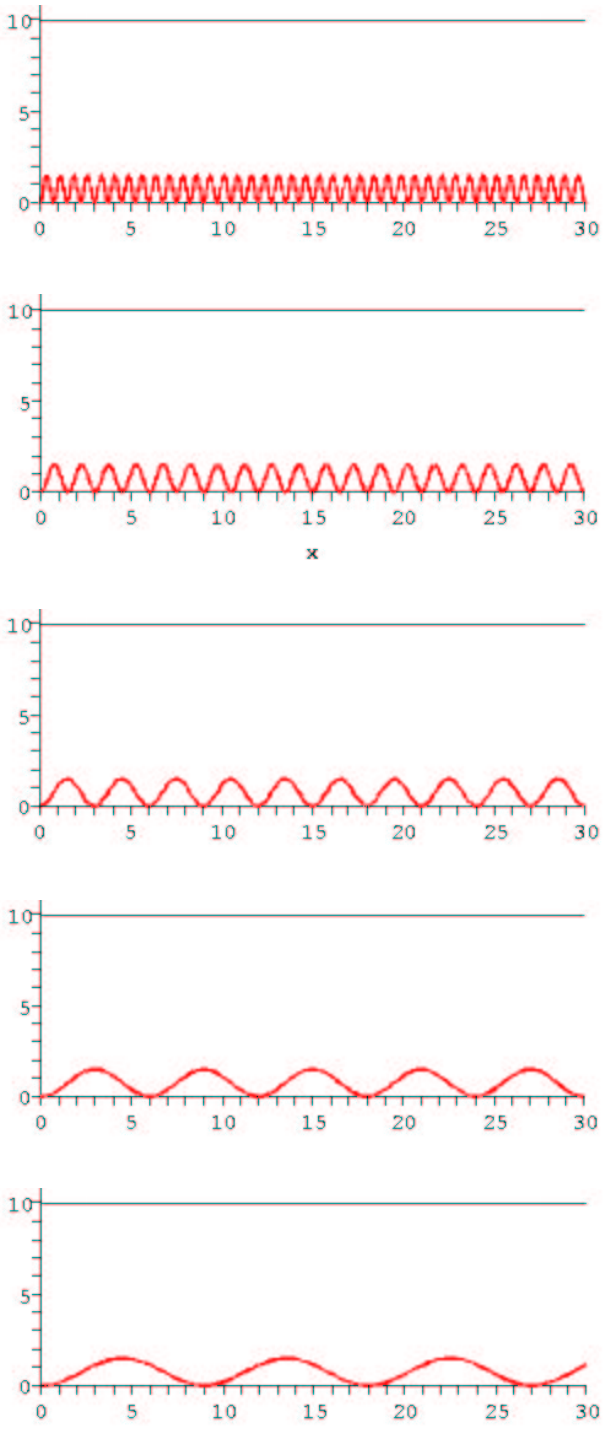

Figure 1.4.9: *Riblets of the same height and shape with period a)* $s = 0.75 \times 10^{-4}m$ *b)* $s = 1.5 \times 10^{-4}m$ *c)* $s = 3 \times 10^{-4}m$ *d)* $s = 6 \times 10^{-4}m$ *e)* $s = 9 \times 10^{-4}m$.

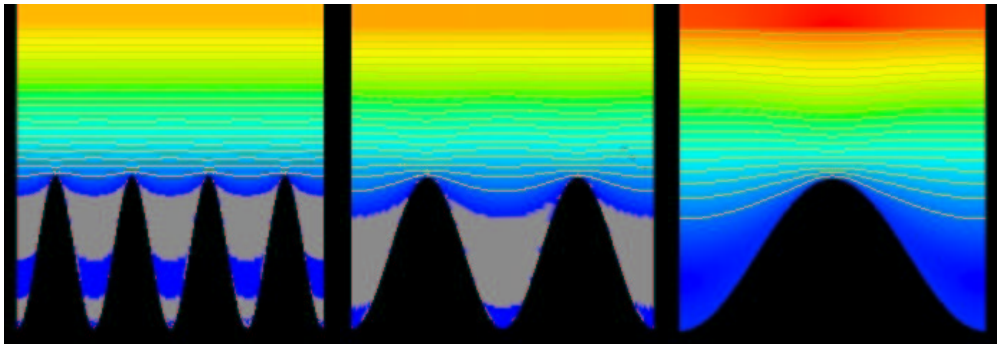

Figure 1.4.10: *Riblets given by* $\gamma(x) = \frac{1}{4}sin(\tau\pi x + \frac{3\pi}{2}) - \frac{3}{4}$ *with spacing a)* $\tau = 8$ *and* $s = 0.75 \times 10^{-4}m$*, b)* $\tau = 4$ *and* $s = 1.5 \times 10^{-4}m$ *and c)* $\tau = 2$ *and* $s = 3 \times 10^{-4}m$*. The colours represent the velocity in x-direction in the range* $0 - 0.6$*.*

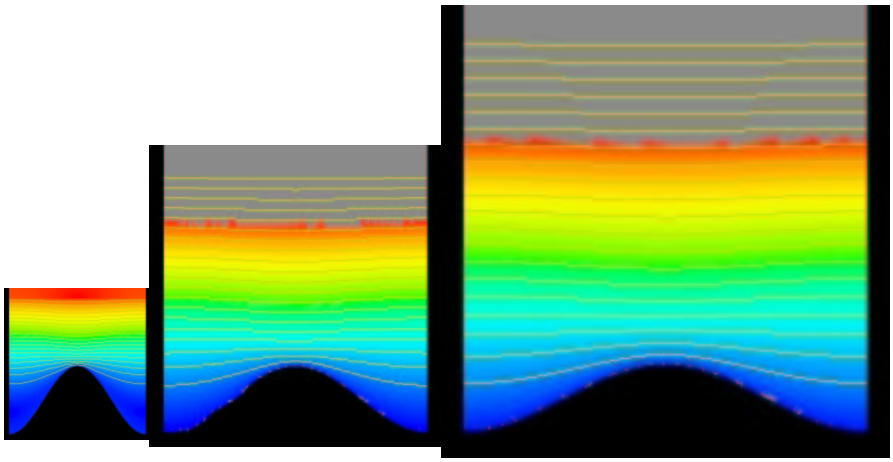

Figure 1.4.11: *Riblets given by a)* $\gamma(x) = \frac{1}{4}sin(2\pi x + \frac{3\pi}{2}) - \frac{3}{4}$ *with spacing* $s = 3 \times 10^{-4}m$*, b)* $\gamma(x) = \frac{1}{8}sin(2\pi x + \frac{3\pi}{2}) - \frac{7}{8}$ *with spacing* $6 \times 10^{-4}m$ *and c)* $\gamma(x) = \frac{1}{12}sin(2\pi x + \frac{3\pi}{2}) - \frac{11}{12}$ *with spacing* $s = 9 \times 10^{-4}m$*. The colours represent the velocity in x-direction in the range* $0 - 0.6$*.*

We analyze this behavior also with a different shape of microstructure which we obtained in our optimization. Here the microscopic representation is no longer the same shape function. We want to see the effect of the spacing if the shape of the thin peak is kept constant. This means that the shape function of the thin peak is the same but the distance between the peaks get wider in each calculation. The representation of the macroscopic shape function γ is more difficult because we have to calculate the right values for the different scaling to keep the height of the microscopic peak fix. The numerical values for the transformed shapes γ for each cell problem are given in table 1.4.3. The lines in the table mark the end of one cell. The function is then the interpolation of these points with cubic splines. The results of the calculations are shown in figures 1.4.12 and 1.4.13, where we also observe that the best structure is the one where the spacing is the double height.

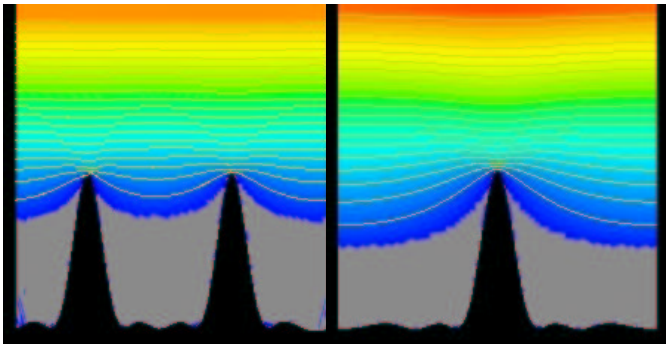

Figure 1.4.12: *Riblets given by a cubic spline interpolation of the numerical values listed in table 1.4.3 a) shape a with* $s = 1.5 \times 10^{-4} m$*, b) shape b with* $s = 3 \times 10^{-4} m$*. The colours represent the velocity in x-direction in the range* $0 - 0.6$*.*

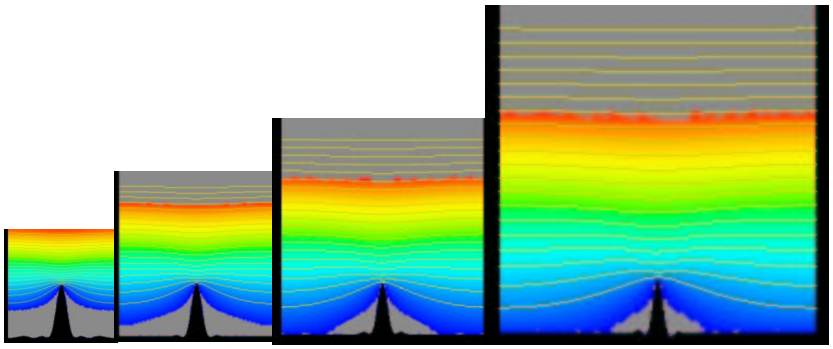

Figure 1.4.13: *Riblets given by a cubic spline interpolation of the numerical values listed in table 1.4.3 a) shape b with* $s = 3 \times 10^{-4} m$*, b) shape c with* $s = 4.5 \times 10^{-4} m$*, c) shape d with* $s = 6 \times 10^{-4} m$*, d) shape e with* $s = 9 \times 10^{-4} m$*. The colours represent the velocity in x-direction in the range* $0 - 0.6$*.*

Table 1.4.3: The numerical values for the riblets tested and scaled to the cell problem.

N	shape a $\gamma(x)$	shape b $\gamma(x)$	shape c $\gamma(x)$	shape d $\gamma(x)$	shape e $\gamma(x)$
0	-1.0	-1.0	-1.0	-1.0	-1.0
1	-0.98	-1.0	-1.0		
2	-0.91	-1.0	-1.0		
3	-0.5	-1.0	-1.0		
4	-0.91	-0.98	-1.0	.	
5	-0.98	-0.95	-1.0	.	
6	-1.0	-0.5	-1.0	.	.
7	-0.98	-0.95	-0.997		.
8	-0.91	-0.98	-0.94		.
9	-0.5	-1.0	-0.66	-1.0	
10	-0.91	-1.0	-0.94	-0.99	
11	-0.98	-1.0	-0.997	-0.955	
12	-1.0	-1.0	-1.0	-0.75	
13	-0.98	-1.0	-1.0	-0.955	
14	-0.91	-1.0	-1.0	-0.99	
15	-0.5	-1.0	-1.0	-1.0	-1.0
16	-0.91	-0.98	-1.0		-0.993
17	-0.98	-0.91	-1.0		-0.983
18	-1.0	-0.5	-1.0	.	-0.833
19	-0.98	-0.91		.	-0.983
20	-0.91	-0.98		.	-0.993
21	-0.5	-1.0			-1.0
22	-0.91	-1.0			
23	-0.98	-1.0			
24	-1.0	-1.0		-1.0	
25	-0.98	-1.0			
26	-0.91	-1.0			
27	-0.5	-1.0			.
28	-0.91	-0.98			.
29	-0.98	-0.91			.
30	-1.0	-0.5			
31	-0.98	-0.91			
32	-0.91	-0.98			
33	-0.5	-1.0			
34	-0.91	-1.0			
35	-0.98	-1.0			
36	-1.0	-1.0			-1.0

Table 1.4.4: The Navier constant for different spacing (shape 2).

s	N	$\tilde{C}_{\mathrm{bl}}$	C_{bl}
1.5×10^{-4}	12	-0.54	-0.54
3.0×10^{-4}	12	-0.58	-0.58
4.5×10^{-4}	18	-0.738	-0.488
6.0×10^{-4}	24	-0.828	-0.328
9.0×10^{-4}	36	-0.908	-0.24

The calculated Navier constants $\tilde{C}_{\mathrm{bl}}$ are listed in table 1.4.4. To be able to compare them we have to evaluate them again at the same position. The transformed Navier constants C_{bl} are listed in the last column.

Now we want to analyze the dependence of the Navier constants for both shapes shown in the figures above on the spacing. The values are evaluated in the next figure. We see that we have an optimal situation for both shapes: the Navier constants are minimal for the case when the heights of the riblets are half of their spacing.

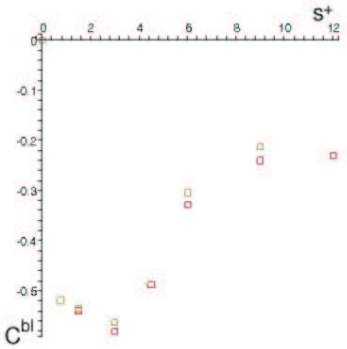

Figure 1.4.14: *The cost function with respect to the spacing of shape 1 and shape 2.*

The results are again comparable with the experiments by Bechert and Walsh (see [11],[58]): Closely spaced riblets work better as drag reducing surfaces. After evaluating the values for shapes obtained by the optimization process (see figure 1.4.12 and 1.4.13) we conclude that very widely spaced riblets do not reduce the skin friction so much. And if we look at the total drag which was evaluated in the experiments, we see that they even increase it. This is because if the riblets are spaced so widely they dampen the cross flow less and do not act as a cross flow shield for their neighbors anymore. The cross flow in the valley of isolated riblets is stronger. This phenomenon plays a more important role when the riblets reach the turbulent boundary layer, the buffer layer. There the cross flow is

much stronger and thus the riblets would act much more as drag reducing devices than in the viscous sublayer. We will see that with this restriction of riblets being in the viscous sublayer the contribution to drag reduction will not be as high as tested for higher riblets. Concerning the spacing we obtain an optimality for the case where the height of the riblet is half its spacing. This conclusion stays in agreement with experimental results obtained by Bechert and co-workers in [9] and with the physiognomy of the shark skin analyzed by Reif and Dinkelacker in [53]. They observed that the height of the microstructures on fast swimming sharks is between one half and two third of their spacing. In our situation the skin friction tends to zero for larger spacing of the riblets.

Chapter 2

Optimal Design Problem

2.1 Setting of the shape optimization problem

Our shape optimization problem is a typical one in fluid mechanics. It consists of finding the profile of a microstructure on the surface of a submerged swimming body such that the tangential drag is minimized. This means in our case that the cost functional is the effective tangential friction and the boundary layer equations are the state problem. With all the simplifications from the last section we come to the following minimization problem:

Find the domain which minimizes the skin friction $J(Z^{\mathrm{bl}}, \beta^{\mathrm{bl}})$ with respect to a part of its boundary $\Gamma \in \delta Z^{\mathrm{bl}}$ subject to the constant height of the microstructure h:

$$\min_{\gamma \in G} \quad J(Z^{\mathrm{bl}}, \beta^{\mathrm{bl}}) = C^{\mathrm{bl}} = -\int_{Z^{\mathrm{bl}}} |\nabla \beta^{\mathrm{bl}}(y)|^2 dy$$

subject to

$$\begin{cases} -\Delta_y \beta^{\mathrm{bl}} + \nabla_y \omega^{\mathrm{bl}} &= 0, \text{ in } Z^+ \cup Y \\ \mathrm{div}_y \ \beta^{\mathrm{bl}} &= 0, \text{ in } Z_{\mathrm{bl}} \\ \left[\beta^{\mathrm{bl}}\right]_S (\cdot, 0) &= 0, \text{ on } S \\ \left[\{\nabla_y \beta^{\mathrm{bl}} - \omega^{\mathrm{bl}} I\} e_2\right]_S (\cdot, 0) &= e_1, \text{ on } S \\ \beta^{\mathrm{bl}} &= 0, \text{ on } \Gamma \\ \{\beta^{\mathrm{bl}}, \omega^{\mathrm{bl}}\} \quad y_1 &- \text{ periodic}, \end{cases} \tag{2.1.1}$$

where $G = \{\gamma : [0,1] \to [-1, -0.5] \quad \Big| \gamma \in C^2([0,1]),\ \gamma(0) = \gamma(1) = -1, \quad \gamma(0.5) = -0.5\}$.

The solution $\gamma^* \in G$ satisfies

$$J(\gamma^*, \beta^{\mathrm{bl}}(\gamma^*)) \leq J(\gamma, \beta^{\mathrm{bl}}) \ \ \forall \gamma \in G.$$

A fundamental property, ensuring the existence of optimal solutions, is the continuous dependence of the solutions of the state problem on the design variables. After imposing appropriate continuity or lower semi-continuity assumptions on the cost functional we will obtain an existence result:

Theorem 2.1.1. Assuming

(B1) compactness of $\mathcal{G} = \{(\gamma, \beta^{\mathrm{bl}}(\gamma)), \gamma \in G, \beta^{\mathrm{bl}}(\gamma) \in V\}$:

for any sequence $(\gamma_n, \beta^{\mathrm{bl}}(\gamma_n))$, where $\gamma_n \in G$ and $\beta^{\mathrm{bl}}(\gamma_n) \in V$ is the solution of the boundary layer problem (1.4.7) with boundary γ_n, there exists a subsequence $(\gamma_{n_k}, \beta^{\mathrm{bl}}(\gamma_{n_k}))$ and an element $(\gamma, \beta^{\mathrm{bl}}(\gamma)) \in \mathcal{G}$ such that

$$\gamma_{n_k} \to \gamma, \quad \text{for } k \to \infty$$

$$\beta^{\mathrm{bl}}(\gamma_{n_k}) \to \beta^{\mathrm{bl}}(\gamma), \quad \text{for } k \to \infty$$

and

(B2) lower semi-continuity of J, i.e.

$$\left.\begin{array}{rcl} \gamma_{n_k} & \to & \gamma, \quad \text{for } k \to \infty \\ \beta^{\mathrm{bl}}(\gamma_{n_k}) & \to & \beta^{\mathrm{bl}}(\gamma), \quad \text{for } k \to \infty \end{array}\right\} \Rightarrow \underline{\lim}\, J(\gamma_n, \beta_n^{\mathrm{bl}}) \geq J(\gamma, \beta^{\mathrm{bl}}).$$

Then, (2.1.1) has at least one solution.

Hence it is sufficient for our optimization problem to have a solution, if the conditions (B1) and (B2) for the solution of the boundary layer equation and respectively for our cost function are fulfilled. Before checking these conditions, we have to specify the parametrization of the boundary and the way how our sequence of shapes is constructed.

2.2 Sensitivity Analysis

To solve an optimization problem two properties are important for the solution of the state problem: As we have seen for the existence of an optimal solution, the continuous dependence to the design variables is one of these properties. The second one is the differentiability with respect to the design and control variables. The discipline in optimization which deals with such information is sensitivity analysis. Sensitivities tell what changes are effected in the state, when the control variables or the design parameters are changed. From results obtained concerning the sensitivities we are able to derive the necessary optimality conditions and we are able to describe how to change the geometry to obtain a minimizing sequence of domains.

In our work we describe the change in geometry as a normal variation of the domain. Let Γ be the part of the boundary of the domain Ω which describes the shape of the microstructures and Γ_λ respectively the part of the boundary of the deformed domain denoted by Ω_λ with $\Gamma_\lambda = \{s + \lambda\alpha(s)n(s) |\ s \in \Gamma\}$. The exact characterization of the functions $\Gamma(x)$ and $\alpha(x)$ will be given in the next subsection.

2.2.1 Parametrization

In this section we describe the parametrization of the function which describes the shape of the microstructures on the surface of the submerged body. In the microscopic model the rough boundary was given by $\mathcal{B}^\varepsilon$ in the coordinates (x_1, x_2), which consists of the periodically distribution of a hump $\Gamma(x_1)$. In the macroscopic model this hump corresponds to $\Gamma(y_1)$ with $y_1 = \frac{x_1}{\varepsilon}$ and $y_1 \in [0,1]$. We choose $\Gamma(y_1)$ from the class of continuous functions with the first and second derivative beeing continuous too, $\Gamma(y_1) \in C^2([0,1])$. The parametrized function will be the interpolated function with cubic splines, $\gamma \in S_H^{(3,2)}[0,1] = \{p \in C^2[0,1] : p|_{I_i} \in P_3(I_i)\}$, $i = 0, ..., N$, where N is the total number of points y_1^i which divide the interval $[0,1]$ in $N-1$ intervals $I_i = [y_1^i, y_1^{i+1}]$, $i = 1, .., N$ of length $H = \frac{1}{N}$. Let φ_i be the basis of the space $S_H^{(3,2)}[0,1]$ given by the condition $\varphi_i(y_1^j) = \delta_{ij}$. The parametrized function γ can be described in the following way:

$$\gamma(y_1) = \sum_{i=0}^{N} \Gamma(y_1^i)\varphi_i(y_1). \tag{2.2.1}$$

For this kind of parametrization the following error estimate holds:

$$\max_{y_1 \in [0,1]} |\Gamma(y_1) - \gamma(y_1)| \leq \frac{1}{2} H^2 \max_{y_1 \in [0,1]} |\Gamma^{(2)}(y_1)|.$$

Let us consider an example:

$$\Gamma(y_1) = 0.25 \sin(2\pi y_1 + \frac{3\pi}{2}) - 0.75.$$

For this case, the fourth derivative exists and is given by $\Gamma^{(4)}(y_1) = 4\pi^4 \sin(2\pi y_1 + \frac{3\pi}{2})$. The error is then $\max_{y_1 \in [0,1]} |\Gamma(y_1) - \gamma(y_1)| \leq 16.23 H^4$.

With this parametrization we now want to analyze the change in geometry. We already mentioned that our boundary Γ should change in the normal direction to $\Gamma_\lambda = \{s + \lambda\alpha(s)n(s) | s \in \Gamma\}$, where $\alpha(s) \in C^2(\Gamma)$ to guarantee the smoothness of the deformed boundary. For the parametrized function it means:

$$\gamma_\lambda(y_1) = \gamma(y_1) + \lambda\alpha(\gamma(y_1))n(\gamma(y_1)).$$

In computations we always use functions which belong to a finite dimensional space which approximates our continuous space instead of continuous functions. This finite space is spanned by functions $\xi_1, ..., \xi_N$, where N is the dimension of the finite space. Then the coefficients of the linear combination of $\{\xi_k\}_{k=0}^N$ form a vector of the discrete design variables α_i:

$$\alpha(s) = \sum_{i=0}^{N} \alpha_i \xi_i(s).$$

For our model of the periodic rough boundary layer we have to keep the two endpoints of $\gamma(y_1)$ and the height h of the roughness fix. We will restrict our model to geometries

where the maximal height of the roughness is in the middle of the interval. The change in geometry looks as follows:

$$\gamma_\lambda(y_1) = \sum_{i=0}^{N} \Gamma(y_1^i)\varphi_i(y_1) + \lambda \sum_{i=0}^{N} \alpha_i \xi_i(s) n_i, \quad \alpha_0 = \alpha_N = \alpha_{\frac{N}{2}} = 0,$$

where n_i are the discrete values of the normal on Γ. Because $\alpha(s) \in C^2(\Gamma)$ we choose the same basis functions for α as for γ, characterized by $\varphi_i(s_j) = \delta_{ij}$. The new boundary $\gamma_\lambda(y_1)$ is then given by

$$\gamma_\lambda(y_1) = \sum_{i=0}^{N} \Big(\Gamma(y_1^i)\varphi_i(y_1) + \lambda \alpha_i \varphi_i(\gamma(y_1)) n_i \Big),$$

with $\varphi_i(\gamma(y_1)) = \gamma(y_1) + \varphi_i(y_1)$. It follows, that

$$\gamma_\lambda(y_1) = \sum_{i=0}^{N} \Big(\Gamma(y_1^i) + \lambda \alpha_i n_i \Big) \varphi_i(y_1) + \lambda \sum_{i=0}^{N} \alpha_i \gamma(y_1) n_i.$$

Using the representation of $\gamma(y_1)$ we get

$$\gamma_\lambda(y_1) = \sum_{i=0}^{N} \Big[\Gamma(y_1^i) \Big(1 + \lambda \sum_{k=0}^{N} \alpha_k n_k \Big) + \lambda \alpha_i n_i \Big] \varphi_i(y_1). \tag{2.2.2}$$

Comparing this result with equation (2.2.1) we see that, as expected, our new boundary is also a spline function which can be represented with the same basis functions $\varphi_i(x)$. The new coefficients are:

$$\Gamma_\lambda(y_1^i) = \Gamma(y_1^i) \Big(1 + \lambda \sum_{k=0}^{N} \alpha_k n_k \Big) + \lambda \alpha_i n_i.$$

2.2.2 Sensitivity

In this subsection we will present the main result obtained for the variation of the cost function:

Theorem 2.2.1. If $\beta^{\mathrm{bl}} \in H^2(Z^{\mathrm{bl}})$ and if the geometry of the domain Z^{bl} changes only on one part of the boundary, denoted by Γ, in the normal direction by $\alpha(s)$, $s \in \Gamma$, $\alpha \in C^2(\Gamma)$ and small, then the change in the cost function is

$$\delta \mathcal{J} = \int_\Gamma \alpha(s) |\partial_n \beta^{\mathrm{bl}}(s)|^2 ds + o(||\alpha||_{C^2[0,1]}),$$

where $\partial_n \beta^{\mathrm{bl}}$ is the derivative of the speed distribution, the weak solution of the boundary layer equation (1.4.3), along the outward normal n to Γ.

Before proving this theorem we have to specify the variation of the cost function in the following way:

The cost function of our optimization problem is given by

$$\min_{\gamma\in G} \quad \mathcal{J}(Z^{\mathrm{bl}}) = -\int_{Z^{\mathrm{bl}}} |\nabla\beta^{\mathrm{bl}}|^2.$$

The change in the cost function is then

$$\delta\mathcal{J} = \mathcal{J}(\widetilde{Z^{\mathrm{bl}}}) - \mathcal{J}(Z^{\mathrm{bl}}) = \int_{Z^{\mathrm{bl}}} |\nabla\beta^{\mathrm{bl}}|^2 - \int_{\widetilde{Z^{\mathrm{bl}}}} |\nabla\widetilde{\beta^{\mathrm{bl}}}|^2,$$

where β^{bl} is the solution of the boundary layer problem in the domain $Z^{\mathrm{bl}} = Z^+ \cup S \cup (Y - b_2e_2)$ and $\widetilde{\beta^{\mathrm{bl}}}$ is the solution of the boundary layer problem in the domain $\widetilde{Z^{\mathrm{bl}}} = Z^+ \cup S \cup (\tilde{Y} - b_2e_2)$, where $Y = \{y \in Z| \quad b_2 > y_2 > \max\{0, \gamma(y_1)\}\}$, $\tilde{Y} = \{y \in Z| \quad b_2 > y_2 > \max\{0, \tilde{\gamma}(y_1)\}\}$ and $\tilde{\gamma}(y_1) = \gamma(y_1) + \alpha(s)n(s)$.

We can extend β^{bl} in the domain $\widetilde{Z^{\mathrm{bl}}} \setminus (Z^{\mathrm{bl}} \cap \widetilde{Z^{\mathrm{bl}}})$ and $\widetilde{\beta^{\mathrm{bl}}}$ in $Z^{\mathrm{bl}} \setminus (Z^{\mathrm{bl}} \cap \widetilde{Z^{\mathrm{bl}}})$ by zero (see [37]). Further we denote the difference of the two solutions by $\delta\beta^{\mathrm{bl}} = \widetilde{\beta^{\mathrm{bl}}} - \beta^{\mathrm{bl}}$, where $\delta\beta^{\mathrm{bl}} \in Z^{\mathrm{bl}} \cup \widetilde{Z^{\mathrm{bl}}}$, and the difference of the two domains Z^{bl}, $\widetilde{Z^{\mathrm{bl}}}$ by $\delta Z^{\mathrm{bl}} = Z^{\mathrm{bl}} \setminus (Z^{\mathrm{bl}} \cap \widetilde{Z^{\mathrm{bl}}}) - \widetilde{Z^{\mathrm{bl}}} \setminus (Z^{\mathrm{bl}} \cap \widetilde{Z^{\mathrm{bl}}})$, which is a very small domain.

Lemma 2.2.2. $\delta\beta^{\mathrm{bl}}$ is the solution of the following system:

$$\begin{cases} -\Delta_y\delta\beta^{\mathrm{bl}} + \nabla_y\delta\omega^{\mathrm{bl}} &= 0, \text{ in } Z^+ \cup Y \\ \mathrm{div}_y\ \delta\beta^{\mathrm{bl}} &= 0, \text{ in } Z^{\mathrm{bl}} \\ \left[\delta\beta^{\mathrm{bl}}\right]_S(\cdot, 0) &= 0, \text{ on } S \\ \left[\{\nabla_y\delta\beta^{\mathrm{bl}} - \delta\omega^{\mathrm{bl}}I\}e_2\right]_S(\cdot, 0) &= 0, \text{ on } S \\ \delta\beta^{\mathrm{bl}} &= -\alpha\partial_n\beta^{\mathrm{bl}}, \text{ on } \Gamma \\ \{\delta\beta^{\mathrm{bl}}, \delta\omega^{\mathrm{bl}}\} \quad (y_1) &- \text{ periodic}, \end{cases} \tag{2.2.3}$$

Proof.

The only non-obvious relation is the boundary condition on $(\gamma - b_2e_2)$. We get it using the Taylor expansion for $\widetilde{\beta^{\mathrm{bl}}} = 0$ on $\tilde{\Gamma}$:

$$\widetilde{\beta^{\mathrm{bl}}}(s + \alpha n) = \widetilde{\beta^{\mathrm{bl}}}(s) + \alpha\partial_n\widetilde{\beta^{\mathrm{bl}}}(s) + o(|\alpha|) = 0, \quad s \in \Gamma$$

$$\Rightarrow \widetilde{\beta^{\mathrm{bl}}}\big|_\Gamma = -\alpha\partial_n\widetilde{\beta^{\mathrm{bl}}}\big|_\Gamma.$$

For the difference of the two solutions we then get

$$\delta\beta_{\mathrm{bl}}\big|_\Gamma = \widetilde{\beta^{\mathrm{bl}}}\big|_\Gamma - \beta^{\mathrm{bl}}\big|_\Gamma = -\alpha\partial_n\beta_{\mathrm{bl}}\big|_\Gamma.$$

The last equation is fulfilled, because $\partial_n \widetilde{\beta^{\mathrm{bl}}}(x)\big|_\Gamma$ is weakly continuous in α (see Lemma 2.2.3).

□

Proof. (of the theorem)

With these assumptions we can transform the variation of the object function in the following way:

$$\begin{aligned}
\delta\mathcal{J} &= \mathcal{J}(\widetilde{Z^{\mathrm{bl}}}) - \mathcal{J}(Z^{\mathrm{bl}}) = \textstyle\int_{Z^{\mathrm{bl}}} |\nabla\beta^{\mathrm{bl}}|^2 - \int_{\widetilde{Z^{\mathrm{bl}}}} |\nabla(\beta^{\mathrm{bl}} + \delta\beta^{\mathrm{bl}})|^2 \\
&= \textstyle\int_{Z^{\mathrm{bl}}} |\nabla\beta^{\mathrm{bl}}|^2 - \int_{\widetilde{Z^{\mathrm{bl}}}} |\nabla\beta^{\mathrm{bl}}|^2 - \int_{\widetilde{Z^{\mathrm{bl}}}} |\nabla\delta\beta^{\mathrm{bl}}|^2 - 2\int_{\widetilde{Z^{\mathrm{bl}}}} \nabla\beta_{\mathrm{bl}}\nabla\delta\beta^{\mathrm{bl}} \\
&= \Big[\textstyle\int_{Z^{\mathrm{bl}}} |\nabla\beta^{\mathrm{bl}}|^2 - \int_{\widetilde{Z^{\mathrm{bl}}}} |\nabla\beta^{\mathrm{bl}}|^2\Big] - 2\int_{Z^{\mathrm{bl}}} \nabla\beta^{\mathrm{bl}}\nabla\delta\beta^{\mathrm{bl}} + o(\delta Z^{\mathrm{bl}}, \delta\beta^{\mathrm{bl}}) \\
&= -\textstyle\int_{\delta Z^{\mathrm{bl}}} |\nabla\beta^{\mathrm{bl}}|^2 - 2\int_{Z^{\mathrm{bl}}} \nabla\beta^{\mathrm{bl}}\nabla\delta\beta^{\mathrm{bl}} + o(\delta Z^{\mathrm{bl}}, \delta\beta^{\mathrm{bl}}).
\end{aligned}$$

Now we calculate the two terms in the above equation separately.

To the first term we apply a change in coordinates. Let ϕ be the continuous function which maps $(y_1, y_2) \in \delta Z^{\mathrm{bl}}$ into $(s, t(s)) \in \Gamma \times [0, \alpha(s)]$: $\phi(x) = s + t(s)n(s)$, where $t \in [0, \alpha(s)]$ is the coordinate in the normal direction. Then,

$$\int_{\delta Z^{\mathrm{bl}}} |\nabla\beta^{\mathrm{bl}}(y)|^2 dy = \int_\Gamma \int_0^{\alpha(s)} |\nabla\beta^{\mathrm{bl}}(s, t(s))|^2 |j(s, t(s))| dt ds, \tag{2.2.4}$$

where $j(s, t(s))$ is the determinant of the Jacobian $J(s, t(s))$ of the map ϕ, which in this case is $1 + O(\kappa)$, where κ is the curvature of the boundary Γ which has to be in $C^2([0, 1])$ to assure the existence of the normal field. Because Γ is compact and connected, $\nabla\beta^{\mathrm{bl}}$ is continuous and $|j(s, t(s))| \geq 0$, we can apply the mean value theorem of the integration theory to (2.2.5). That means, it exists an $t^*(s) \in [0, \alpha(s)]$ such that

$$\int_\Gamma \int_0^{\alpha(s)} |\nabla\beta^{\mathrm{bl}}(s, t(s))|^2 |j(s, t(s))| dt ds = \int_\Gamma |\nabla\beta^{\mathrm{bl}}(s, t^*(s))|^2 \int_0^{\alpha(s)} |j(s, t(s))| dt ds.$$

All admissible α are small, so that we can write the Taylor expansion for $\nabla\beta^{\mathrm{bl}}(s, t^*(s))$:

$$\begin{aligned}
&\textstyle\int_\Gamma |\nabla\beta^{\mathrm{bl}}(s, t^*(s))|^2 \int_0^{\alpha(s)} |j(s, t(s))| dt ds = \int_\Gamma |\nabla\beta^{\mathrm{bl}}(s, 0)|^2 \int_0^{\alpha(s)} |j(s, t(s))| dt ds \\
&\qquad + \textstyle\int_\Gamma \big[\partial_t(|\nabla\beta^{\mathrm{bl}}(s, t(s))|^2)\big]\Big|_{t=0} t^*(s) \int_0^{\alpha(s)} |j(s, t(s))| dt ds + ... \qquad .
\end{aligned}$$

Inserting the determinant of the Jacobian of our mapping ϕ we get

$$\int_{\delta Z^{\mathrm{bl}}} |\nabla\beta^{\mathrm{bl}}|^2 = \int_\Gamma \int_0^{\alpha(s)} |\nabla\beta^{\mathrm{bl}}|^2 + o(||\alpha||_{C^2}) = \int_\Gamma \alpha |\partial_n\beta^{\mathrm{bl}}|^2 + o(||\alpha||_{C^2}). \tag{2.2.5}$$

For the second term we use the corresponding boundary layer equation which in this case

is the Stokes equation which is self-adjoint:

$$\begin{aligned}
\int_{Z^{\mathrm{bl}}} \nabla\beta^{\mathrm{bl}}\nabla\delta\beta^{\mathrm{bl}} &= \int_{Z^{\mathrm{bl}}}(-\Delta\beta^{\mathrm{bl}})\delta\beta^{\mathrm{bl}} + \int_{\partial Z^{\mathrm{bl}}}(\partial_n\beta^{\mathrm{bl}})\delta\beta^{\mathrm{bl}} \\
&= \int_{Z^{\mathrm{bl}}} -(\nabla\omega^{\mathrm{bl}})\delta\beta^{\mathrm{bl}} + \int_{\partial Z^{\mathrm{bl}}}(\partial_n\beta^{\mathrm{bl}})\delta\beta^{\mathrm{bl}} \\
&= \int_{Z^{\mathrm{bl}}} \omega^{\mathrm{bl}}\nabla\cdot\delta\beta^{\mathrm{bl}} - \int_{\partial Z_{\mathrm{bl}}} n\cdot\omega^{\mathrm{bl}}\cdot\delta\beta^{\mathrm{bl}} + \int_{\partial Z^{\mathrm{bl}}}(\partial_n\beta^{\mathrm{bl}})\delta\beta^{\mathrm{bl}} \\
&= \int_{\partial Z^{\mathrm{bl}}}(\partial_n\beta^{\mathrm{bl}} - \omega^{\mathrm{bl}}n)\delta\beta^{\mathrm{bl}} \\
&= \int_{\Gamma}(\partial_n\beta^{\mathrm{bl}} - \omega^{\mathrm{bl}}n)(-\alpha(\partial_n\beta^{\mathrm{bl}})) \\
&= -\int_{\Gamma}\alpha|\partial_n\beta^{\mathrm{bl}}|^2.
\end{aligned} \tag{2.2.6}$$

The last equation is true because

$$n\cdot\partial_n\beta^{\mathrm{bl}} = 0 \text{ on } \Gamma,$$

and we get this using

$$0 = \operatorname{div}\beta^{\mathrm{bl}} = \frac{\partial\beta_1^{\mathrm{bl}}}{\partial x_1} + \frac{\partial\beta_2^{\mathrm{bl}}}{\partial x_2}.$$

We rotate the coordinate system such that we have a decomposition of β^{bl} in the normal and tangential coordinates: $\frac{\partial\beta_n^{\mathrm{bl}}}{\partial n} + \frac{\partial\beta_t^{\mathrm{bl}}}{\partial t}$. The tangential part lies along Γ where $\beta^{\mathrm{bl}} = 0$. It follows that $n\cdot\partial_n\beta^{\mathrm{bl}} = 0$ on Γ.

Adding the two integrals (2.2.5) and (2.2.6) the variation of our object function can be written as

$$\delta\mathcal{J} = \int_{\Gamma}\alpha|\partial_n\beta^{\mathrm{bl}}|^2 + o(||\alpha||_{C^2}) \tag{2.2.7}$$

which completes our proof.

□

In the proof of the previous lemma we used the weakly continuity of $\partial_n\widetilde{\beta^{\mathrm{bl}}}(x)\big|_{\Gamma}$ in α. For completeness we will give here the proof of this statement:

Lemma 2.2.3. Let $\widetilde{\beta^{\mathrm{bl}}}(y_1, y_2)$ be the solution of the boundary layer equation for the domain $\widetilde{Z^{\mathrm{bl}}}$ which is obtained by moving the boundary Γ of Z^{bl} in the normal direction by an admissible function α. Then $\nabla\widetilde{\beta^{\mathrm{bl}}}(x)\big|_{\Gamma}$ is weakly continuous in α.

Proof. From the definition of derivatives in the distribution sense it suffices to show that $\widetilde{\beta^{\mathrm{bl}}}(y_1, y_2)$ converges weakly to $\beta^{\mathrm{bl}}(y_1, y_2)$ when $\alpha \to 0$ or $\tilde{\gamma} \to \gamma$ uniformly in $[0, 1]$. Let $\widetilde{\beta^{\mathrm{bl}}} \in \tilde{V} = \{z \in L^2_{\mathrm{loc}}(\widetilde{Z^{\mathrm{bl}}})^2 : \nabla_y z \in L^2(\widetilde{Z^{\mathrm{bl}}})^4;\ z = 0 \text{ on } \tilde{\Gamma};\ \operatorname{div}_y z = 0 \text{ in } \widetilde{Z^{\mathrm{bl}}};\ z\ y_1\text{ - periodic}\}$ be the solution of

$$\int_{\widetilde{Z^{\mathrm{bl}}}} \nabla\widetilde{\beta^{\mathrm{bl}}}\nabla\varphi = -\int_S \varphi e_1 \quad \forall\varphi \in \tilde{V}. \tag{2.2.8}$$

Let $\widetilde{\beta^{\mathrm{bl}}}$ and $\hat{\varphi}$ be the extension of β^{bl} and φ by zero in $Z^{\mathrm{bl}}\setminus(Z^{\mathrm{bl}}\cap\widetilde{Z^{\mathrm{bl}}})$ (see [37]). Replacing φ by $\widetilde{\beta^{\mathrm{bl}}}$ in (2.2.9) we obtain

$$\int_{Z^{\mathrm{bl}}\cup\widetilde{Z^{\mathrm{bl}}}} |\nabla\widetilde{\beta^{\mathrm{bl}}}|^2 = -\int_S \widetilde{\beta^{\mathrm{bl}}} e_1$$

which implies (see [37]) that $\{\widetilde{\beta^{\mathrm{bl}}}\}$ is bounded in $H_0^1(Z^{\mathrm{bl}} \cup \widetilde{Z^{\mathrm{bl}}})$. As every bounded set is weakly compact, we can extract a subsequence $\{\widetilde{\beta^{\mathrm{bl}}}\}$ which converges weakly to β^{bl}. It remains to prove that β^{bl} is a solution of

$$\int_{Z^{\mathrm{bl}}} \nabla\beta^{\mathrm{bl}} \nabla\varphi = -\int_S \varphi e_1 \quad \forall\varphi \in H_0^1(Z^{\mathrm{bl}}). \tag{2.2.9}$$

Suppose, it is not. Then there exists an $\varepsilon > 0$ and a $\varphi \in H_0^1(Z^{\mathrm{bl}})$ with $\varphi\Big|_{\tilde{\Gamma}} = 0$ and $\operatorname{div}\varphi = 0$ in Z^{bl}, such that

$$\Big|\int_{Z^{\mathrm{bl}}} \nabla\beta^{\mathrm{bl}} \nabla\varphi + \int_S \varphi e_1\Big| \geq \varepsilon. \tag{2.2.10}$$

As seen before, we can extend β^{bl} and φ in $\widetilde{Z^{\mathrm{bl}}} \setminus (Z^{\mathrm{bl}} \cap \widetilde{Z^{\mathrm{bl}}})$ by zero. Then, (2.2.10) is equivalent to

$$\Big|\int_{Z^{\mathrm{bl}} \cup \widetilde{Z^{\mathrm{bl}}}} \nabla\beta^{\mathrm{bl}} \nabla\varphi + \int_S \varphi e_1\Big| \geq \frac{\varepsilon}{2}.$$

From the weak convergence of $\{\widetilde{\beta^{\mathrm{bl}}}\}$ to β^{bl} in $H_0^1(Z^{\mathrm{bl}} \cup \widetilde{Z^{\mathrm{bl}}})$ we obtain a contradiction to the above inequality.

□

With this proof we also checked condition (B1) from theorem 2.1.1, the continuous dependence of the solution of the state problem on the design variable. Imposing the lower semicontinuity condition on our cost function, we arrive to an existence result of our optimization problem.

2.2.3 Optimality Condition

On the basis of the previous results we can now formulate necessary optimality conditions satisfied by optimal solutions. Their interpretation may reveal some important properties and may give a hint how to choose the geometry deformation.

Let

$$\mathcal{O} = \{\Omega \text{ open set in } \mathbb{R}^2 : \quad \Omega = Z^{\mathrm{bl}}, \text{with the part of the boundary } \gamma \in G\}.$$

Theorem 2.2.4. If the solution of (2.1.1) is smooth, it satisfies the first order necessary condition

$$|\partial_n \beta^{\mathrm{bl}}|^2 = \text{const} \quad \text{on} \quad \Gamma.$$

Proof. If the domain $\Omega \in \mathcal{O}$, with Γ being the part of the boundary which describes the shape of the roughness is optimal, then $\delta\mathcal{J} = 0$ holds for every admissible α. Thus, inserting the results of the previous theorem, and applying the well known Lagrange multiplier rule, there exists a constant λ (Lagrange multiplier) such that

$$|\partial_n \beta^{\mathrm{bl}}|^2 = \lambda \quad \text{on} \quad \Gamma.$$

We say that α is admissible, if

$$-\int_\Gamma \alpha d\Gamma = o(||\alpha||_{C^2}).$$

This is the condition by which $\Omega \in \mathcal{O}$ implies $\Omega_\alpha \in \mathcal{O}$.

□

2.2.4 Boundary modification

In this subsection we will propose two possibilities of changing the boundary iteratively. We start with a given profile with smooth boundary Γ. As explained before we change the boundary in its normal direction by an admissible function $\alpha(s)$, $s \in \Gamma$. The main question is how to choose $\alpha(s)$ such that after a few iterations we reach the optimality condition as close as possible in our calculations.

1st Method: Special choice of α:

The authors in [41], [46], [48] and [47] consider the optimization of the shape of a body (e.g. wing of an airplane) to reduce drag. To minimize the drag in absence of lift and gravity, they minimize the energy of the system for Stokes and Navier-Stokes flow with the restriction that the volume of the body should be kept fix. Our optimality condition obtained in the previous subsection coincides with the optimality conditions in their case. They proposed to choose the function α to be the factor under the integral in the change of the cost function (see 2.2.7) minus its mean value and multiplied by a constant to fulfill the constraint. In our case we choose $\alpha(s)$ as

$$\alpha(s) = \begin{cases} 0 & \text{if } s = \{0; 0.5; 1\} \\ -\left|\partial_n \beta^{\text{bl}}(s)\right|^2 & \text{else.} \end{cases} \tag{2.2.11}$$

Using this rule for the modification of our domain we restrict the deformation in one direction because $\left|\partial_n \beta^{\text{bl}}(s)\right|^2 \geq 0$. This means our microstructure can not grow, it can only shrink. Of course it will be interesting to answer the question, if the optimal microstructure will be the one with the smallest possible volume or not. We will answer this question later, where we will present the numerical results.

Lemma 2.2.5. Choosing $\alpha(s)$ as in (2.2.11) and moving the boundary Γ from an initial profile to

$$\Gamma_\lambda = \{s + \lambda \alpha(s) n(s) |\ s \in \Gamma\},$$

we obtain a solution of our optimization problem (2.1.1).

Proof. The modified profile is a solution of our minimization problem (2.1.1), if

$$\mathcal{J}(\tilde{\Gamma}, \widetilde{\beta}^{\text{bl}}) - \mathcal{J}(\Gamma, \beta) = \int_\Gamma \alpha |\partial_n \beta^{\text{bl}}|^2 = -\int_\Gamma |\partial_n \beta^{\text{bl}}|^4 \leq 0$$

□

2nd Method: Sensitivity information method

To be more general we want to allow a change in both directions of the boundary Γ to let one part of the boundary shrink and another part, if necessary, grow. This property is not included in the first method, since $\alpha(s) = -\left|\partial_n \beta^{\text{bl}}(s)\right|^2 \leq 0 \ \forall s \in \Gamma$, and the so constructed new boundary is obtained by shrinking the original one.

In the subsection 2.2.2, we calculated the Gateau derivative of the cost function with respect to the boundary. Our second ansatz consists of the information coming from these sensitivities. First of all let us discretize our continuous design parameter $\alpha(s)$:

$$\alpha(s) = \sum_{k=0}^{N} \alpha_k \varphi_k(s),$$

where α_k are now the $N+1$ discrete design variables and $\varphi_k(s)$ the $N+1$ basis functions for our admissible deformation. We choose the discrete design variables as follows:

$$\alpha_k = \int_\Gamma \varphi_k(s) \left|\partial_n \beta^{\text{bl}}(s)\right|^2 ds \tag{2.2.12}$$

Lemma 2.2.6. Choosing $\alpha(s)$ as in (2.2.12) and moving the boundary Γ from an initial profile to

$$\Gamma_\lambda = \{s + \lambda \alpha(s) n(s) |\ s \in \Gamma\},$$

we obtain a solution of our optimization problem (2.1.1).

Proof. We insert the chosen deformation function $\alpha(s)$ in the formula for the change of the cost function:

$$\begin{aligned}
\mathcal{J}(\tilde{\Gamma}, \widetilde{\beta}^{\text{bl}}) - \mathcal{J}(\Gamma, \beta) &= \textstyle\int_\Gamma \alpha |\partial_n \beta^{\text{bl}}|^2 \\
&= \textstyle\int_\Gamma \Big(\sum_k \alpha_k \varphi_k(s) \Big) \left|\partial_n \beta(s)\right|^2 ds \\
&= \textstyle\int_\Gamma \sum_k \Big(\int_\Gamma \varphi_k(s) \left|\partial_n \beta(s)\right|^2 ds \, \varphi_k(s) \Big) \left|\partial_n \beta(s)\right|^2 ds
\end{aligned}$$

Let us consider the sign of this expression: $\left|\partial_n \beta(s)\right|^2 ds \geq 0 \ \forall s \in \Gamma$. The integral can only be negative if the basis functions where $\left|\partial_n \beta(s)\right|^2$ is very big are negative, $\varphi_k(s) < 0$, this is again the situation of shrinking domains.

□

We learn that for a growing microstructure we obtain a growing cost function and for a shrinking microstructure a shrinking cost function. For the change in geometry we can choose any smooth small function α which exploits the information from the sensitivity so that we can handle the optimization problem with a gradient based method.

2.3 Sensitivity-based optimization method

Most of the problems resulting from shape optimization in fluid mechanics are not possible to be solved with the well known one-shot approach, where the coupled optimality system is solved through computational methods and the optimal states and controls are obtained without solving an optimization iteration. Instead, optimization algorithms can be used to determine the optimal states and controls. Many optimization algorithms require the gradient or at least an approximation of the gradient of the functional which has to be minimized with respect to the controls or design variables. We will use sensitivities to help to determine the gradient of the functional. Alternatively it is possible to use the solution of an adjoint system to determine the gradient of the functional.

2.3.1 The gradient of the cost functional through sensitivities

We consider following minimization method

$$\min_{\gamma \in G} \mathcal{J}(\beta^{\mathrm{bl}}(\gamma), \gamma),$$

where $\beta^{\mathrm{bl}}(\gamma)$ is the solution of our state problem, the boundary layer equation. To determine the gradient of the functional for the optimization algorithm, we can apply the chain rule:

$$\frac{D\mathcal{J}}{D\gamma}\Big|_{\gamma^i} = \frac{\partial \mathcal{J}}{\partial \beta^{\mathrm{bl}}}\Big|_{\gamma^i} \frac{\mathrm{d}\beta^{\mathrm{bl}}}{\mathrm{d}\gamma}\Big|_{\gamma^i} + \frac{\partial \mathcal{J}}{\partial \gamma}\Big|_{\gamma^i},$$

where $(\cdot)\big|_{\gamma^i}$ denotes the evaluation at the current boundary inside the iteration. Here, $\frac{\partial \mathcal{J}}{\partial \beta^{\mathrm{bl}}}$ and $\frac{\partial \mathcal{J}}{\partial \gamma}$ are usually easy to determine, where the sensitivity of the solution of the state equation has to be specified, mostly through a difference quotient approximation:

$$\frac{\mathrm{d}\beta^{\mathrm{bl}}}{\mathrm{d}\gamma}(\gamma^i(s))(\gamma^{i-1}(s) - \gamma^i(s)) \approx \beta^{\mathrm{bl}}(\gamma^{i-1}(s)) - \beta^{\mathrm{bl}}(\gamma^i(s)) \text{ for small } \alpha.$$

To calculate this sensitivity we have to run the code for the state equation twice with different inputs.

Due to our calculations in the previous section we are able to calculate the gradient for the optimization routine more elegant: we use the difference quotient approximation directly to the cost function. Then we have

$$\frac{D\mathcal{J}}{D\gamma}(\gamma^i(s))(\gamma^{i-1}(s) - \gamma^i(s)) \approx \mathcal{J}(\beta^{\mathrm{bl}}(\gamma^{i-1}(s)), \gamma^{i-1}(s)) - \mathcal{J}(\beta^{\mathrm{bl}}(\gamma^i(s)), \gamma^i(s)) \text{ for small } \alpha.$$

And now we have the big advantage to insert the analytical expression for the variation of the cost function in this formula and obtain:

$$\frac{D\mathcal{J}}{D\gamma}(\gamma^i)(\alpha) \approx \int_\Gamma \alpha |\partial_n \beta^{\mathrm{bl}}|^2 + o(||\alpha||_{C^2}) \text{ for small } \alpha. \tag{2.3.1}$$

2.3.2 Optimization method: steepest descent

After we know how the gradient of the functional looks like, we can choose our favorite optimization method to compute the new shape for the next iteration. We choose a gradient method, the steepest descent with line search to calculate an optimal step size.

The basis of gradient methods is the Taylor expansion of the cost function, which is continuously differentiable:

$$\mathcal{J} : H^1([0,1]) \to \mathbb{R}$$
$$\mathcal{J}(\gamma) := J(\Gamma, \beta^{\text{bl}}),$$

which is

$$\mathcal{J}(\gamma + \delta\gamma) = \mathcal{J}(\gamma) + \mathcal{J}'(\gamma)\delta\gamma + o(||\delta\gamma||) \ \forall \delta\gamma \in H^1([0,1]),$$

where $\mathcal{J}' : H^1 \to \mathbb{R}$ is a linear operator. From the sensitivity analysis, we know that in our case

$$< \text{grad}_\gamma \mathcal{J}, \delta\gamma >= \mathcal{J}'\alpha = \int_\Gamma \alpha |\partial_n \beta|^2 \ \forall \alpha \text{ admissible}\,.$$

By choosing $\alpha(s)$, $s \in \Gamma$, as proposed in the last section, the sequence defined by:

$$\gamma^{n+1} = \gamma^n + \alpha(s) n(s) \tag{2.3.2}$$

makes $\mathcal{J}$ decreasing. Following well known result holds

Theorem 2.3.1. If $\mathcal{J}$ is continuous differentiable, bounded from below and infinite at infinity, then all accumulation points γ^* of γ^n generated by (2.3.2) satisfy

$$\text{grad}_\gamma \mathcal{J}(\gamma^*) = 0.$$

In our case $\mathcal{J}$ is bounded from below because the dissipated energy is bounded and bounded from above by zero. This property is more restrictive than the one needed in the theorem. So that we are sure that every accumulation point will be a stationary point. The optimization problem reads as follows:

$$\min_{\gamma \in H^1([0,1])} - \int_{Z^{\text{bl}}} ||\nabla \beta^{\text{bl}}||^2 \tag{2.3.3}$$

subject to the variational formulation of the boundary layer equation:

$$\int_{Z^{\text{bl}}} \nabla \beta^{\text{bl}} \nabla \varphi = - \int_0^1 e_1 \varphi \ \forall \varphi \in V.$$

To apply the gradient method we need to formulate an unconstrained optimization problem. Therefore we have to construct the Lagrangian of (2.3.3):

$$L(\gamma, \beta^{\text{bl}}, \varphi) = - \int_{Z^{\text{bl}}} |\nabla \beta^{\text{bl}}|^2 - \int_{Z^{\text{bl}}} \nabla \beta^{\text{bl}} \nabla \varphi - \int_0^1 e_1 \varphi$$

and (2.3.3) is equivalent to the min-max problem

$$\min_{\gamma, \beta^{\text{bl}}} \Big\{ \max_\varphi L(\gamma, \beta^{\text{bl}}, \varphi) \Big\}. \tag{2.3.4}$$

From the theorem of min-max, we know that at the solution $\{\beta^{\mathrm{bl}}, \varphi\}$ of the min-max:

$$\mathcal{J}'_\gamma(\gamma, \beta^{\mathrm{bl}}) = L'_\gamma(\gamma, \beta^{\mathrm{bl}}, \varphi).$$

The pair $\{\beta^{\mathrm{bl}}, \varphi\}$ is a saddle point of L, if:

$$\begin{aligned}
&\partial_\lambda L(\gamma, \beta^{\mathrm{bl}} + \lambda\widetilde{\beta}^{\mathrm{bl}}, \varphi)\Big|_{\lambda=0} = \\
&\quad = \lim_{\lambda\to 0} \tfrac{1}{\lambda}\Big(L(\gamma, \beta^{\mathrm{bl}} + \lambda\widetilde{\beta}^{\mathrm{bl}}, \varphi) - L(\gamma, \beta^{\mathrm{bl}}, \varphi)\Big) \\
&\quad = \lim_{\lambda\to 0} \tfrac{1}{\lambda}\Big(-\textstyle\int_{Z^{\mathrm{bl}}} |\nabla(\beta^{\mathrm{bl}} + \lambda\widetilde{\beta}^{\mathrm{bl}})|^2 - \int_{Z^{\mathrm{bl}}} \nabla(\beta^{\mathrm{bl}} + \lambda\widetilde{\beta}^{\mathrm{bl}})\nabla\varphi - \int_0^1 e_1\varphi \\
&\qquad\qquad + \textstyle\int_{Z^{\mathrm{bl}}} |\nabla\beta^{\mathrm{bl}}|^2 + \int_{Z^{\mathrm{bl}}} \nabla\beta\nabla\varphi + \int_0^1 e_1\varphi\Big) \\
&\quad = \lim_{\lambda\to 0} \tfrac{1}{\lambda}\Big(-\textstyle\int_{Z^{\mathrm{bl}}} |\nabla\beta^{\mathrm{bl}}|^2 - \lambda^2 \int_{Z^{\mathrm{bl}}} |\nabla\widetilde{\beta}^{\mathrm{bl}}|^2 - 2\lambda \int_{Z^{\mathrm{bl}}} \nabla\beta^{\mathrm{bl}}\nabla\widetilde{\beta}^{\mathrm{bl}} - \int_{Z^{\mathrm{bl}}} \nabla\beta^{\mathrm{bl}}\nabla\varphi \\
&\qquad\qquad -\lambda \textstyle\int_{Z^{\mathrm{bl}}} \nabla\widetilde{\beta}^{\mathrm{bl}}\nabla\varphi + \int_{Z^{\mathrm{bl}}} |\nabla\beta^{\mathrm{bl}}|^2 + \int_{Z^{\mathrm{bl}}} \nabla\beta^{\mathrm{bl}}\nabla\varphi\Big) \\
&\quad = \lim_{\lambda\to 0} \tfrac{1}{\lambda}\Big(-\lambda^2 \textstyle\int_{Z^{\mathrm{bl}}} |\nabla\widetilde{\beta}^{\mathrm{bl}}|^2\Big) - 2\int_{Z^{\mathrm{bl}}} \nabla\beta^{\mathrm{bl}}\nabla\widetilde{\beta}^{\mathrm{bl}} - \int_{Z^{\mathrm{bl}}} \nabla\widetilde{\beta}^{\mathrm{bl}}\nabla\varphi \\
&\quad = 0 \\
&\qquad\qquad \Longleftrightarrow\ 2\int_{Z^{\mathrm{bl}}} \nabla\beta^{\mathrm{bl}}\nabla\widetilde{\beta}^{\mathrm{bl}} + \int_{Z^{\mathrm{bl}}} \nabla\widetilde{\beta}^{\mathrm{bl}}\nabla\varphi = 0 \qquad \forall\widetilde{\beta}^{\mathrm{bl}} \in V. \qquad (2.3.5)
\end{aligned}$$

$$\begin{aligned}
&\partial_\lambda L(\gamma, \beta^{\mathrm{bl}}, \varphi + \lambda\tilde{\varphi})\Big|_{\lambda=0} = \\
&\quad = \lim_{\lambda\to 0} \tfrac{1}{\lambda}\Big(L(\gamma, \beta^{\mathrm{bl}}, \varphi + \lambda\tilde{\varphi}) - L(\gamma, \beta^{\mathrm{bl}}, \varphi)\Big) \\
&\quad = \lim_{\lambda\to 0} \tfrac{1}{\lambda}\Big(-\textstyle\int_{Z^{\mathrm{bl}}} |\nabla\beta^{\mathrm{bl}}|^2 - \int_{Z^{\mathrm{bl}}} \nabla\beta^{\mathrm{bl}}\nabla(\varphi + \lambda\tilde{\varphi}) - \int_0^1 e_1(\varphi + \lambda\tilde{\varphi}) \\
&\qquad\qquad + \textstyle\int_{Z^{\mathrm{bl}}} |\nabla\beta^{\mathrm{bl}}|^2 + \int_{Z^{\mathrm{bl}}} \nabla\beta^{\mathrm{bl}}\nabla\varphi + \int_0^1 e_1\varphi\Big) \\
&\quad = \lim_{\lambda\to 0} \tfrac{1}{\lambda}\Big(-\textstyle\int_{Z^{\mathrm{bl}}} \nabla\beta\nabla\varphi - \lambda \int_{Z^{\mathrm{bl}}} \nabla\beta\nabla\tilde{\varphi} - \lambda \int_0^1 e_1\tilde{\varphi} + \int_{Z^{\mathrm{bl}}} \nabla\beta\nabla\varphi\Big) \\
&\quad = 0 \\
&\qquad\qquad \Longleftrightarrow\ \int_{Z^{\mathrm{bl}}} \nabla\beta^{\mathrm{bl}}\nabla\tilde{\varphi} + \int_0^1 e_1\tilde{\varphi} = 0 \qquad \forall\tilde{\varphi} \in V. \qquad (2.3.6)
\end{aligned}$$

Stationarity with respect to the boundary Γ is

$$\begin{aligned}
&\lim_{\lambda\to 0} \tfrac{1}{\lambda}\Big(L(\gamma + \lambda\alpha, \widetilde{\beta}^{\mathrm{bl}}, \varphi) - L(\gamma, \beta^{\mathrm{bl}}, \varphi)\Big) = \\
&\quad = \lim_{\lambda\to 0} \tfrac{1}{\lambda}\Big(-\textstyle\int_{\widetilde{Z^{\mathrm{bl}}}} |\nabla\widetilde{\beta}^{\mathrm{bl}}|^2 - \int_{\widetilde{Z^{\mathrm{bl}}}} \nabla\widetilde{\beta}^{\mathrm{bl}}\nabla\varphi - \int_0^1 e_1\varphi + \int_{Z^{\mathrm{bl}}} |\nabla\beta^{\mathrm{bl}}|^2 \\
&\qquad\qquad + \textstyle\int_{Z^{\mathrm{bl}}} \nabla\beta^{\mathrm{bl}}\nabla\varphi + \int_0^1 e_1\varphi\Big) \\
&\quad = \lim_{\lambda\to 0} \tfrac{1}{\lambda}\Big(\lambda\,\delta\mathcal{J}(\gamma, \beta) - \textstyle\int_{\widetilde{Z^{\mathrm{bl}}}} \nabla\widetilde{\beta}^{\mathrm{bl}}\nabla\varphi + \int_{Z^{\mathrm{bl}}} \nabla\beta^{\mathrm{bl}}\nabla\varphi\Big).
\end{aligned}$$

We already know the sensitivity of the cost function from a former section and need only to calculate the sensitivity of $\int_{Z^{\mathrm{bl}}} \nabla\beta\nabla\varphi$:

Corollary 2.3.2. If $\widetilde{Z^{\mathrm{bl}}}$ is the domain resulting by moving the boundary $\Gamma \in \partial Z^{\mathrm{bl}}$ in the normal direction by $\lambda\alpha(s)$ admissible, then

$$\int_{Z^{\mathrm{bl}}} \nabla\beta^{\mathrm{bl}}\nabla\varphi - \int_{\widetilde{Z^{\mathrm{bl}}}} \nabla\widetilde{\beta}^{\mathrm{bl}}\nabla\varphi = \int_\Gamma \lambda\alpha\partial_n\beta^{\mathrm{bl}}\partial_n\varphi \qquad \forall\alpha \text{ admissible.}$$

Proof. For proving this statement we use the tools from the former chapter, i.e. we extend the solution $\beta^{\mathrm{bl}} \in Z^{\mathrm{bl}}$ to the domain $\widetilde{Z^{\mathrm{bl}}} \setminus (Z^{\mathrm{bl}} \cap \widetilde{Z^{\mathrm{bl}}})$ and write the solution of the boundary layer equation in this domain as $\widetilde{\beta}^{\mathrm{bl}} = \beta^{\mathrm{bl}} + \delta\beta^{\mathrm{bl}}$, where $\delta\beta^{\mathrm{bl}}$ solves (2.2.3). Then, we have

$$\begin{aligned}
&\textstyle\int_{Z^{\mathrm{bl}}} \nabla\beta^{\mathrm{bl}}\nabla\varphi - \int_{\widetilde{Z^{\mathrm{bl}}}} \nabla(\beta^{\mathrm{bl}} + \delta\beta^{\mathrm{bl}})\nabla\varphi = \\
&\qquad = \textstyle\int_{Z^{\mathrm{bl}}} \nabla\beta^{\mathrm{bl}}\nabla\varphi - \int_{\widetilde{Z^{\mathrm{bl}}}} \nabla\beta^{\mathrm{bl}}\nabla\varphi - \int_{\widetilde{Z^{\mathrm{bl}}}} \nabla\delta\beta^{\mathrm{bl}}\nabla\varphi \\
&\qquad = -\textstyle\int_{\delta Z^{\mathrm{bl}}} \nabla\beta^{\mathrm{bl}}\nabla\varphi - \int_{\widetilde{Z^{\mathrm{bl}}}} \nabla\delta\beta^{\mathrm{bl}}\nabla\varphi.
\end{aligned}$$

From the mean value theorem of integration we get

$$\int_{\delta Z^{\mathrm{bl}}} \nabla\beta^{\mathrm{bl}}\nabla\varphi = \int_0^\alpha \int_\Gamma \nabla\beta^{\mathrm{bl}}\nabla\varphi = \int_\Gamma \lambda\alpha\partial_n\beta^{\mathrm{bl}}\partial_n\varphi + o(||\gamma||). \tag{2.3.7}$$

Further we need to evaluate the second integral, $\int_{\widetilde{Z^{\mathrm{bl}}}} \nabla\delta\beta^{\mathrm{bl}}\nabla\varphi$, where φ solves equation (2.3.5). We have

$$\int_{\widetilde{Z^{\mathrm{bl}}}} \nabla\delta\beta^{\mathrm{bl}}\nabla\varphi = \int_{Z^{\mathrm{bl}}} \nabla\delta\beta^{\mathrm{bl}}\nabla\varphi + o(\delta Z^{\mathrm{bl}}, \delta\beta^{\mathrm{bl}}),$$

so that we are looking only at the domain Z^{bl}:

$$\begin{aligned}
\textstyle\int_{Z^{\mathrm{bl}}} \nabla\delta\beta^{\mathrm{bl}}\nabla\varphi &= -\textstyle\int_{Z^{\mathrm{bl}}} \delta\beta^{\mathrm{bl}}\Delta\varphi + \int_{\partial Z^{\mathrm{bl}}} \delta\beta^{\mathrm{bl}}\partial_n\varphi \\
&= \textstyle\int_{Z^{\mathrm{bl}}} \delta\beta^{\mathrm{bl}}(2\Delta\beta^{\mathrm{bl}}) + \int_{\partial Z^{\mathrm{bl}}} \delta\beta^{\mathrm{bl}}\partial_n\varphi \\
&= 2\textstyle\int_{Z^{\mathrm{bl}}} \delta\beta^{\mathrm{bl}}(-\nabla\omega^{\mathrm{bl}}) + \int_{\partial Z^{\mathrm{bl}}} \delta\beta^{\mathrm{bl}}\partial_n\varphi \\
&= 2\textstyle\int_{Z^{\mathrm{bl}}} \nabla\cdot\delta\beta^{\mathrm{bl}}\omega^{\mathrm{bl}} - 2\int_{\partial Z^{\mathrm{bl}}} \delta\beta^{\mathrm{bl}}\omega^{\mathrm{bl}}n + \int_{\partial Z^{\mathrm{bl}}} \delta\beta^{\mathrm{bl}}\partial_n\varphi \\
&= \textstyle\int_{\partial Z^{\mathrm{bl}}} \Big(\partial_n\varphi - 2\omega^{\mathrm{bl}}n\Big)\delta\beta^{\mathrm{bl}} \\
&= 2\textstyle\int_\Gamma \omega^{\mathrm{bl}}n\lambda\alpha\partial_n\beta^{\mathrm{bl}}ds - \int_\Gamma \partial_n\varphi\lambda\alpha\partial_n\beta^{\mathrm{bl}} \\
&= -\textstyle\int_\Gamma \lambda\alpha\partial_n\varphi\partial_n\beta^{\mathrm{bl}}.
\end{aligned}$$

The last equality holds because $n\partial_n\beta^{\mathrm{bl}} = 0$ on Γ as shown already using the divergence free and the boundary condition for β^{bl}.

□

For the stationarity with respect to Γ following condition must be true:

$$\lim_{\lambda\to 0}\frac{1}{\lambda}\Big(L(\gamma+\lambda\alpha,\widetilde{\beta}^{\mathrm{bl}},\varphi)-L(\gamma,\beta^{\mathrm{bl}},\varphi)\Big)=\int_\Gamma \alpha|\partial_n\beta^{\mathrm{bl}}|^2=0$$

We have shown following theorem:

Theorem 2.3.3. The variation of J, which is defined in (2.3.3), with respect to the shape deformation $\gamma'=\{x+\alpha(x)n(x):\ x\in\Gamma\}$ is

$$\delta\mathcal{J}=\mathcal{J}(\gamma',\beta^{\mathrm{bl}\prime})-\mathcal{J}(\gamma,\beta^{\mathrm{bl}})=\int_\Gamma \alpha|\partial_n\beta^{\mathrm{bl}}|^2+o(||\alpha||).$$

The concept of our gradient method is the following one:

Conceptual gradient method with Armijo Rule

Step 1: Choose Γ^0, $0<\vartheta<\beta<1$, set $i=0$;

Step 2: Solve the boundary layer equation (1.4.3) with $\Gamma=\Gamma^i$;

Step 3: Calculate α^i on Γ^i, if it is small enough STOP;

Step 4: Find a λ^i such that

$$-\lambda^i\beta||\alpha^i||^2<\delta\mathcal{J}(\Gamma^i)<-\lambda^i\vartheta||\alpha^i||^2;$$

Step 5: Set $\Gamma^{i+1}=\Gamma^i+\lambda^i\alpha^i n^i$ and go to Step 2.

2.4 Numerical Simulation

As already mentioned, from the sensitivity analysis we know how to deform our boundary to build a sequence of domains which tend to an optimal solution of our problem. This is one reason to compute the solutions of the stationary equations separately with an external code for partial differential equations which can handle rough boundaries. We chose a package called FEMLISP which was developed by N. Neuss from the technical simulation group of the IWR to solve such kind of boundary layer problems for the model of flow over a porous media (see [34]). We wanted to use this existing software package because it could be adapted to our problem of rough domains, where the infinite cell problem is replaced by a semi-infinite one. Because of the special behavior of the solution of the boundary layer problem, the exponentially stabilization to a constant value away from the boundary, FEMLISP provides efficient solvers for our problem (high order approximation, mesh adaptivity, multigrid solvers, see [45]) and the information where to cut the infinite domain. We couple the existing software package for solving the state equation with an optimization code written in C++. The connection of these two parts, the interface for the data transfer, is realized with a TCP/IP socket communication.

At first, a few approximations have to be done: the infinite domain of the boundary layer problem has to be approximated by a finite one, i.e. we have to cut it at a position $y=k$ and to impose additional boundary conditions on that part of the domain.

The position of cutting has to be chosen in such a way that the resulting finite domain describes a good approximation of the original infinite domain. This bounded domain is sent to the state equation solver. An important step in solving the state equation is the generation of an adequate mesh. A rectangular grid with uniform refinement shows significantly anisotropies and produces a greater discretization error because of the complicated geometry of our roughness. With triangles and local refinement we get better results. For our state equations an automatic grid generator called Triangle is used. To solve the Stokes equation finite elements for the discretization in space are used. Because of the incompressibility we need a stable discretization. We have chosen the Taylor-Hood finite element which approximates the velocity piecewise with a continuous polynomial of degree k and the pressure piecewise with a continuous polynomial of degree k-1 on the generated mesh. In our calculations we use k=4. The created mesh on the finite domain can be refined successively where the refinement rules on the reference cells are supposed to be regular or it can be refined locally using hanging nodes. The degree of refinement of two neighbor cells does not differ with more than two. Standard interpolation error estimates (see [21]) and standard a-priori error estimates for the finite element approximation can be used if we exclude the interface, where the solutions are discontinuous, from the domain. This can be done only if the interface is smooth and aligned with the mesh. The a-priori error estimates give us information about how good the solution on the refined mesh is compared to the solution on the sparser mesh. In the case of global refinement the discretization error can be estimated using the asymptotic behavior of the a-priori error. If local refinements are used, the a-posteriori error estimates are described in [45]. To solve the discretized problem FEMLISP offers the possibility to use direct sparse solvers (UMFPACK) or a multigrid solver. Until now the multigrid solver runs only with uniform refinement, adaptive refinement can be implemented in future. The direct solver runs with uniform and adaptive refinement. The multigrid solver and the smoothing step uses subspace corrections. For our situation a V-cycle with Vanka-VC-SSC-smoothing (*Vanka-vertex centered-successive subspace correction-smoothing*) is used. The Vanka-smoothing (see [57]) uses overlapping blocks for the degrees of freedom. In this case for the pressure vertex centered blocks are used with all velocities appearing in that block. The robust convergence of this method was not yet proved theoretically but tested numerically successfully. We have to point out, that for our optimization problem we need high accuracy for the numerical calculations because of the changing structure of the rough boundary in each iteration. For the 2D-calculations we are able to do maximal three levels of refinement using the direct solver, with the multigrid solver there are more.

In the next subsections we will describe the steps for the numerics in more details.

2.4.1 Approximation of the boundary layer problem on a finite domain

The state equations of our optimization problem are given by:

$$\begin{aligned} -\Delta_y \beta^{\mathrm{bl}} + \nabla_y \omega^{\mathrm{bl}} &= 0, \text{ in } Z^+ \cup Y \\ \mathrm{div}_y\ \beta^{\mathrm{bl}} &= 0, \text{ in } Z^{\mathrm{bl}} \\ \left[\beta^{\mathrm{bl}}\right]_S (\cdot, 0) &= 0, \text{ on } S \\ \left[\{\nabla_y \beta^{\mathrm{bl}} - \omega^{\mathrm{bl}} I\} e_2\right]_S (\cdot, 0) &= e_1, \text{ on } S \\ \beta^{\mathrm{bl}} &= 0, \text{ on } \Gamma \\ \{\beta^{\mathrm{bl}}, \omega^{\mathrm{bl}}\} \qquad y_1 &- \text{ periodic}, \end{aligned} \tag{2.4.1}$$

where $S = (0, b_1)$, $Z^+ = (0, b_1) \times (0, +\infty)$ and the infinite boundary layer is $Z^{\mathrm{bl}} = Z^+ \cup S \cup Y$.

The first step in the numerical realization consists of the approximation of the solution of (2.4.1) with solutions $\beta_k^{\mathrm{bl}}(y_1, y_2)$ of problems defined on finite domains: $Z_k^{\mathrm{bl}} := Z^{\mathrm{bl}} \cap ((0, b_1) \times (-b_2, k))$, while the unit cell is given by $Z_k^+ \cup Y$, with $Z_k^+ = (0, 1) \times (0, k)$ and Y being the fluid part of the cell of roughness defined in section 1.2. This solutions $\beta_k^{\mathrm{bl}}(y_1, y_2)$ fulfill the following equations:

$$\begin{aligned} -\Delta_y \beta_k^{\mathrm{bl}} + \nabla_y \omega_k^{\mathrm{bl}} &= 0, \text{ in } Z_k^+ \cup Y \\ \mathrm{div}_y\ \beta_k^{\mathrm{bl}} &= 0, \text{ in } Z_k^{\mathrm{bl}} \\ \left[\beta_k^{\mathrm{bl}}\right]_S (\cdot, 0) &= 0, \text{ on } S \\ \left[\{\nabla_y \beta_k^{\mathrm{bl}} - \omega_k^{\mathrm{bl}} I\} e_2\right]_S (\cdot, 0) &= e_1, \text{ on } S \\ \beta_k^{\mathrm{bl}} &= 0, \text{ on } \Gamma \\ (\beta_k^{\mathrm{bl}})_2 = \frac{\partial (\beta_k^{\mathrm{bl}})_1}{\partial y_2} &= 0, \text{ on } y_2 = k, \\ \{\beta_k^{\mathrm{bl}}, \omega_k^{\mathrm{bl}}\} \qquad (y_1) &- \text{ periodic}, \end{aligned} \tag{2.4.2}$$

The additional boundary conditions on $y_2 = k$ are the standard boundary conditions at a solid wall: the fluid is not allowed to penetrate the wall, $(\beta_k^{\mathrm{bl}})_2 = 0$, and the derivative of the tangential velocity is zero, $\frac{\partial (\beta_k^{\mathrm{bl}})_1}{\partial y_2} = 0$. The requirement for the pressure field to be unique is:

$$\int_\Gamma \omega_k^{\mathrm{bl}} dy = 0.$$

Let $V_k = \{z \in L^2_{\text{loc}}(Z_k^{\text{bl}})^2 : \nabla_y z \in L^2(Z_k^{\text{bl}})^4;\ z = 0 \text{ on } \Gamma;\ \text{div}_y\, z = 0 \text{ on } Z_k^{\text{bl}};\ z\ y_1 \text{ - periodic}\}$, then the weak formulation of (2.4.2) is given through

$$\beta_k^{\text{bl}} \in V_k : \int_{Z_k^{\text{bl}}} \nabla\beta_k^{\text{bl}} \nabla\varphi = -\int_S \varphi e_1 \quad \forall \varphi \in V_k. \tag{2.4.3}$$

With (2.4.2) we are able to calculate the approximation C_{bl}^k of the Navier constant C_{bl} which was defined in section 1.4:

$$C_{\text{bl}}^k = \int_S (\beta_k^{\text{bl}})_1(y_1, 0) dy_1.$$

Doing approximations we have to control the error which occurs in this process. To calculate the error in the cost function we first have to prove the following proposition:

Proposition 2.4.1. Let $\{\beta_k^{\text{bl}}, \omega_k^{\text{bl}}\}$ be the solution of (2.4.2). Then, for every $\delta < 2\pi$, a constant C exists such that

$$||\nabla\beta_k^{\text{bl}} - \nabla\beta^{\text{bl}}||_{L^2(Z_k^{\text{bl}})} \leq Ce^{-\delta k}. \tag{2.4.4}$$

Proof. Let $\xi := \beta^{\text{bl}} - \beta_k^{\text{bl}}$ and $\psi := \omega^{\text{bl}} - \omega_k^{\text{bl}}$. Then (ξ, ψ) is y_1 - periodic, vanishes on Γ and solves following equations:

$$\begin{aligned} -\Delta\xi + \nabla\psi &= 0 \text{ in } Z_k^{\text{bl}} \\ \text{div}\,\xi &= 0 \text{ in } Z_k^{\text{bl}}. \end{aligned} \tag{2.4.5}$$

Testing this equation with the function ξ we obtain

$$\int_{Z_k^{\text{bl}}} |\nabla\xi|^2 = \int_0^1 (\nabla\xi - \psi I) e_2 \xi dy_1 \Big|_{y_2 = k}. \tag{2.4.6}$$

It follows

$$||\nabla\xi||^2_{L^2(Z_k^{\text{bl}})} \leq |(\nabla\xi(y_1, k) - \psi(y_1, k)I)e_2||\xi(y_1, k)|.$$

The desired inequality can be obtained using Lemma 10 from [34], where an explicit representation for β_k^{bl} is given. This representation was obtained applying the curl-operator to the boundary layer equation and making a variation of the constants from the solution of the resulting Laplace equation. From here we have also the condition $\delta < 2\pi$. Using this representation of β_k^{bl} the authors from [34] were able to prove the exponential decay of $\beta_1^{\text{bl}} - C_{\text{bl}}$, β_2^{bl}, $D^\alpha\beta^{\text{bl}}$, $\omega^{\text{bl}} - C_{\text{bl}}^\omega$ ($C_{\text{bl}}^\omega := \int_S \omega^{\text{bl}}(y_1, 0)dy_1$) and respectively $(\beta_k^{\text{bl}})_1 - C_k^{\text{bl}}$, $(\beta_k^{\text{bl}})_2$, $D^\alpha\beta_k^{\text{bl}}$, $\omega_k^{\text{bl}} - C_{\text{bl, k}}^\omega$ ($C_{\text{bl, k}}^\omega := \int_S \omega_k^{\text{bl}}(y_1, 0)dy_1$):

$$\begin{aligned}
|\beta^{\text{bl}} - (C_{\text{bl}}, 0)| &\leq C(a, \delta)e^{-\delta y_2} \quad \forall \quad y_2 > a > 0 \\
|\beta_k^{\text{bl}} - (C_{\text{bl}}^k, 0)| &\leq C(a, \delta)e^{-\delta y_2} \quad \forall \quad y_2 > a > 0 \\
|D^\alpha\beta^{\text{bl}}| &\leq C(a, \delta, \alpha)e^{-\delta y_2} \quad \forall \quad y_2 > a > 0 \\
|D^\alpha\beta_k^{\text{bl}}| &\leq C(a, \delta, \alpha)e^{-\delta y_2} \quad \forall \quad y_2 > a > 0 \\
|\omega^{\text{bl}} - C_{\text{bl}}^\omega| &\leq Ce^{-\delta y_2} \quad \forall \quad y_2 > 0 \\
|\omega_k^{\text{bl}} - C_{\text{bl, k}}^\omega| &\leq Ce^{-\delta y_2} \quad \forall \quad y_2 > 0
\end{aligned}$$

Applying this to (2.4.6) we obtain

$$||\nabla\xi||^2_{L^2(Z_k^{\mathrm{bl}})} \leq \tilde{C}e^{-2\delta k}$$

and with this (2.4.4).

□

The approximation error in the objective function C_{bl}, can be estimated as follows:

Corollary 2.4.2. For every $\delta < 2\pi$ there is a constant C such that

$$|C_{\mathrm{bl}} - C^k_{\mathrm{bl}}| \leq Ce^{-2\pi k}.$$

Proof. We have

$$|C_{\mathrm{bl}} - C^k_{\mathrm{bl}}| = \Big|\int_0^1 \beta_1^{\mathrm{bl}}(y_1, 0) - (\beta_k^{\mathrm{bl}}(y_1, 0))_1\Big|. \tag{2.4.7}$$

From lemma 1.4.3 we can write

$$|C_{\mathrm{bl}} - C^k_{\mathrm{bl}}| = \Big|\int_{Z_0^{\mathrm{bl}}} \beta_1^{\mathrm{bl}} - (\beta_k^{\mathrm{bl}})_1\Big|,$$

where with Z_0^{bl} we denote only one cell ($Z_0^{\mathrm{bl}} = Y$). Using the inequalities of Hölder and Poincaré we obtain

$$|C_{\mathrm{bl}} - C^k_{\mathrm{bl}}| \leq ||\beta_1^{\mathrm{bl}} - (\beta_k^{\mathrm{bl}})_1||_{L^2(Z_0^{\mathrm{bl}})} \leq C||\nabla\beta_k^{\mathrm{bl}} - \nabla\beta^{\mathrm{bl}}||_{L^2(Z_0^{\mathrm{bl}})}. \tag{2.4.8}$$

From proposition 2.4.1 we have

$$|C_{\mathrm{bl}} - C^k_{\mathrm{bl}}| \leq Ce^{-\delta k}. \tag{2.4.9}$$

□

In order to obtain the approximation error for the pressure difference we have first to construct suitable test functions following the idea from the case of porous media:

Lemma 2.4.3. For each $F \in L^2(Z_k^{\mathrm{bl}})$ satisfying $\int_{Z_k^{\mathrm{bl}}} F = 0$, there exists a function $\varphi \in H^1(Z_k^{\mathrm{bl}})$ with $\varphi = 0$ on Γ and $\{y_2 = k\}$ and satisfying $-\operatorname{div}\varphi = F$ together with the stability estimate

$$||\nabla\varphi||_{L^2(Z_k^{\mathrm{bl}})} \leq (k+1)C||F||_{L^2(Z_k^{\mathrm{bl}})}. \tag{2.4.10}$$

Proof. We search for a function φ which can be written in the form

$$\varphi = \nabla\eta + \operatorname{curl}\vartheta, \tag{2.4.11}$$

where the second term is only used as a correction term correcting the non-zero boundary values from $\operatorname{div}\eta$. Now, η is the solution of following equation

$$\begin{aligned} -\Delta\eta &= F, \text{ in } Z_k^{\mathrm{bl}} \\ \tfrac{\partial\eta}{\partial\nu} &= 0, \text{ on } \{y_2 = k\}. \end{aligned} \tag{2.4.12}$$

Testing the Laplace equation from above with η we get

$$\int_{Z_k^{\mathrm{bl}}} |\nabla\eta|^2 = \int_{Z_k^{\mathrm{bl}}} F\eta = \int_{Z_k^{\mathrm{bl}}} F(\eta - \frac{1}{|Z_k^{\mathrm{bl}}|}\int_{Z_k^{\mathrm{bl}}} \eta), \tag{2.4.13}$$

which holds because $\int_{Z_k^{\mathrm{bl}}} F = 0$. We apply the Poincaré inequality and obtain

$$||\nabla\eta||_{L^2(Z_k^{\mathrm{bl}})} \leq (k+1)C||F||_{L^2(Z_k^{\mathrm{bl}})}. \tag{2.4.14}$$

□

With the help of this lemma we obtain following error estimate for the pressure field:

Proposition 2.4.4. Let ω^{bl} and ω_k^{bl} be the pressure fields determined by (2.4.1) and (2.4.2). Then, for every $\delta < 2\pi$, there exists a constant C such that

$$||\omega^{\mathrm{bl}} - \omega_k^{\mathrm{bl}}||_{L^2(Z_k^{\mathrm{bl}})} \leq (k + \sqrt{k} + 1)Ce^{-\delta k}. \tag{2.4.15}$$

Proof. Let

$$\bar{\omega} := \frac{1}{|Z_k^{\mathrm{bl}}|}\int_{Z_k^{\mathrm{bl}}} (\omega^{\mathrm{bl}} - \omega_k^{\mathrm{bl}}) \tag{2.4.16}$$

and $F := \omega^{\mathrm{bl}} - \omega_k^{\mathrm{bl}} - \bar{\omega}$. Since $\int_{Z_k^{\mathrm{bl}}} F = 0$, the lemma from above guarantees the existence of a function φ which can be used as a test function in the following equation:

$$-\Delta(\beta^{\mathrm{bl}} - \beta_k^{\mathrm{bl}}) + \nabla(\omega^{\mathrm{bl}} - \omega_k^{\mathrm{bl}}) = 0. \tag{2.4.17}$$

Integrating by parts we obtain

$$\int_{Z_k^{\mathrm{bl}}} \nabla(\beta^{\mathrm{bl}} - \beta_k^{\mathrm{bl}})\nabla\varphi + \int_{Z_k^{\mathrm{bl}}} (\omega^{\mathrm{bl}} - \omega_k^{\mathrm{bl}})\,\mathrm{div}\,\varphi = 0. \tag{2.4.18}$$

$$\iff \int_{Z_k^{\mathrm{bl}}} \nabla(\beta^{\mathrm{bl}} - \beta_k^{\mathrm{bl}})\nabla\varphi = \int_{Z_k^{\mathrm{bl}}} (\omega^{\mathrm{bl}} - \omega_k^{\mathrm{bl}})F = \int_{Z_k^{\mathrm{bl}}} F^2, \tag{2.4.19}$$

where we inserted $\bar{\omega}$. From proposition 2.4.1 and lemma 2.4.3 we obtain

$$||F||_{L^2(Z_k^{\mathrm{bl}})} \leq (k+1)Ce^{-\delta k}. \tag{2.4.20}$$

It remains to estimate $\bar{\omega}$: From theorem 3.7 of [29] we have

$$|\bar{\omega}| \leq C\sqrt{k}||\nabla(\beta^{\mathrm{bl}} - \beta_k^{\mathrm{bl}})||_{L^2(Z_k^{\mathrm{bl}})} \tag{2.4.21}$$

Applying the triangle inequality, (2.4.20) and (2.4.21) we obtain

$$||\omega^{\mathrm{bl}} - \omega_k^{\mathrm{bl}}||_{L^2(Z_k^{\mathrm{bl}})} \leq ||F||_{L^2(Z_k^{\mathrm{bl}})} + ||\bar{\omega}||_{L^2(Z_k^{\mathrm{bl}})} \leq C(k + \sqrt{k} + 1)e^{-\delta k}.$$

□

2.4.2 Discretization of the boundary layer problem

For the discretization of the boundary layer equation the package FEMLISP uses Taylor-Hood finite elements on triangular or quadrilateral meshes. For our computations we have chosen P_4/P_3^c on triangular meshes, where P_p is the space of polynomial functions of order p. That means that we approximate the velocity with a continuous polynomial function of degree four and the pressure with a continuous polynomial function of degree three (for the notation see [52]). With this element $\mathcal{FE} = P_4/P_3^c$ following space is defined:

$$S_h := \{\psi \in H^1(Z_k^{\mathrm{bl}}) |\, \psi \; y_1 \text{ - periodic } \; \wedge \forall e : \psi \circ \Phi_e \in \mathcal{FE}\},$$

where $\mathcal{T}_h$ is the partition of Z_k^{bl} in subsets e called elements, where each element e is the image of a reference element $\hat{e}$ under a mapping $\Phi_e : \hat{e} \to e$, where $\hat{e}$ is the reference triangle $\hat{T} := \{(x_1, x_2) | x_1 \geq 0, x_2 \geq 0, x_1 + x_2 \leq 1\}$. The following standard interpolation error can be used in this case (see [18]):

Theorem 2.4.5. Let Z_k^{bl}, $\mathcal{T}_h$ and S_h be as above with the generalized element $\mathcal{FE} = P_p/P_{p-1}^c$. For $p, m, l \in \mathbb{N}$, $p \geq 1$, $0 \leq l \leq p+1$ and $0 \leq m \leq \min(l, 1)$ an operator $\Pi : L^2(Z_k^{\mathrm{bl}}) \to S_h$ exists such that

$$||\beta_k^{\mathrm{bl}} - \Pi\beta_k^{\mathrm{bl}}||_{H^m(Z_k^{\mathrm{bl}} \setminus S)} \leq C(\mathcal{T}_h, l, m, p) h^{l-m} ||\beta_k^{\mathrm{bl}}||_{H^l(Z_k^{\mathrm{bl}} \setminus S)} \qquad \forall \beta_k^{\mathrm{bl}} \in H^l(Z_k^{\mathrm{bl}} \setminus S).$$

Additionally, if β_k^{bl} has zero boundary values on some component of $\partial Z_k^{\mathrm{bl}}$, then also $\beta_{k,h}^{\mathrm{bl}}$ can be chosen such that it has zero boundary values on that boundary component.

In all cases the upper bounds only depend on the smoothness of the domain and the quality of the domain partition $\mathcal{T}_h$.

The ansatz space of the velocity field is defined as

$$H_h := \{\varphi_h \in S_h^2 |\, (\varphi_h)_2 = 0|_{y_2 = k}\}$$

and the ansatz space for the pressure field as

$$L_h := \{\psi_h \in S_h | \int \psi_h dy = 0\}.$$

We now search for $(\beta_{k,h}^{\mathrm{bl}}, \omega_{k,h}^{\mathrm{bl}}) \in H_h \times L_h$ being the solution of

$$\begin{array}{rcl} \int_{Z_k^{\mathrm{bl}}} \nabla\beta_{k,h}^{\mathrm{bl}} \nabla\varphi_{k,h} dy + \int_{Z_k^{\mathrm{bl}}} \nabla\omega_{k,h}^{\mathrm{bl}} \varphi_{k,h} dy & = & -\int_S \varphi_{k,h} e_1 \\ \int_{Z_{k,h}^{\mathrm{bl}}} \mathrm{div}\beta_{k,h}^{\mathrm{bl}} \chi_{k,h} & = & 0 \end{array} \tag{2.4.22}$$

for all $(\varphi_{k,h}, \chi_{k,h}) \in H_h \times L_h$.

For the discretization chosen, following standard error estimate can be used from [19]:

Proposition 2.4.6. Let $\mathcal{T}_h, H_h, L_h$ be defined as above with the generalized element $\mathcal{FE} = P_p/P_{p-1}^c$. Assume that the interior boundary $S = \{y_2 = 0\}$ is aligned with the sides of elements of $\mathcal{T}_h$, let $(\beta_k^{\mathrm{bl}}, \omega_k^{\mathrm{bl}})$ be the solution of (2.4.1) and let $(\beta_{k,h}^{\mathrm{bl}}, \omega_{k,h}^{\mathrm{bl}}) \in H_h \times L_h$ be

the solution of (2.4.22). Then we have an error estimate in the viscous energy norm of the form

$$||\nabla(\beta_k^{\mathrm{bl}}-\beta_{k,h}^{\mathrm{bl}})||_{L^2(Z_k^{\mathrm{bl}}\setminus S)}+h||\nabla(\omega_k^{\mathrm{bl}}-\omega_{k,h}^{\mathrm{bl}})||_{L^2(Z_k^{\mathrm{bl}}\setminus S)} \leq Ch^p(||\beta_k^{\mathrm{bl}}||_{H^{p+1}(Z_k^{\mathrm{bl}}\setminus S)}+||\omega_k^{\mathrm{bl}}||_{H^p(Z_k^{\mathrm{bl}}\setminus S)},$$

where the constant C depends only on k and not of h.

The discrete approximation of the Navier constant is defined as follows

$$C_{k,h}^{\mathrm{bl}} := \int_S (\beta_{k,h}^{\mathrm{bl}})_1$$

and following estimate holds (see [34]):

Proposition 2.4.7. For the discrete Navier constant $C_{k,h}^{\mathrm{bl}}$ given above, we have

$$|C_{k,h}^{\mathrm{bl}} - C_k^{\mathrm{bl}}| \leq C(k)h^{2p-1}.$$

Proof. To show this inequality, we use the variational formulation for the finite domain (see (2.4.3)) and use the functions $\beta_k^{\mathrm{bl}} \in V_k$ and $\beta_{k,h}^{\mathrm{bl}} \in H_h \subseteq V_k$ as test functions:

$$\begin{aligned} C_{k,h}^{\mathrm{bl}} - C_k^{\mathrm{bl}} &= \textstyle\int_S(\beta_{k,h}^{\mathrm{bl}} - \beta_k^{\mathrm{bl}})e_1 ds \\ &= \textstyle\int_{Z_k^{\mathrm{bl}}} \nabla\beta_k^{\mathrm{bl}}\nabla(\beta_k^{\mathrm{bl}} - \beta_{k,h}^{\mathrm{bl}})dx + \int_{Z_k^{\mathrm{bl}}} \nabla\omega_k^{\mathrm{bl}}(\beta_k^{\mathrm{bl}} - \beta_{k,h}^{\mathrm{bl}})dx \\ &= \textstyle\int_{Z_k^{\mathrm{bl}}} |\nabla(\beta_k^{\mathrm{bl}} - \beta_{k,h}^{\mathrm{bl}})|^2 dx + \int_{Z_k^{\mathrm{bl}}} \nabla\beta_{k,h}^{\mathrm{bl}}\nabla(\beta_k^{\mathrm{bl}} - \beta_{k,h}^{\mathrm{bl}})dx \\ &\quad \textstyle+ \int_{Z_k^{\mathrm{bl}}} \nabla\omega_k^{\mathrm{bl}}(\beta_k^{\mathrm{bl}} - \beta_{k,h}^{\mathrm{bl}})dx. \end{aligned}$$

Further we use both variational formulations, the one on the finite domain (see 2.4.3) and the one for the discretized problem (see 2.4.22), and test both with $\beta_{k,h}^{\mathrm{bl}}$. Then

$$\begin{aligned} C_{k,h}^{\mathrm{bl}} - C_k^{\mathrm{bl}} &= \textstyle\int_{Z_k^{\mathrm{bl}}} |\nabla(\beta_k^{\mathrm{bl}} - \beta_{k,h}^{\mathrm{bl}})|^2 dx - \int_{Z_k^{\mathrm{bl}}} \nabla(\omega_k^{\mathrm{bl}} - \omega_{k,h}^{\mathrm{bl}})\beta_{k,h}^{\mathrm{bl}} dx \\ &\quad \textstyle+ \int_{Z_k^{\mathrm{bl}}} \nabla\omega_k^{\mathrm{bl}}(\beta_k^{\mathrm{bl}} - \beta_{k,h}^{\mathrm{bl}})dx. \end{aligned}$$

From the second equation of (2.4.22) we know that

$$\begin{aligned} \textstyle\int_{Z_k^{\mathrm{bl}}} \nabla\omega_k^{\mathrm{bl}}(\beta_k^{\mathrm{bl}} - \beta_{k,h}^{\mathrm{bl}})dx &= \textstyle\int_{Z_k^{\mathrm{bl}}} \nabla(\omega_k^{\mathrm{bl}} - \omega_{k,h}^{\mathrm{bl}})(\beta_k^{\mathrm{bl}} - \beta_{k,h}^{\mathrm{bl}})dx + \int_{Z_k^{\mathrm{bl}}} \nabla\omega_{k,h}^{\mathrm{bl}}\beta_k \\ &\quad \textstyle- \int_{Z_k^{\mathrm{bl}}} \nabla\omega_{k,h}^{\mathrm{bl}}\beta_{k,h} \qquad (2.4.23) \\ &= \textstyle\int_{Z_k^{\mathrm{bl}}} \nabla(\omega_k^{\mathrm{bl}} - \omega_{k,h}^{\mathrm{bl}})(\beta_k^{\mathrm{bl}} - \beta_{k,h}^{\mathrm{bl}})dx \end{aligned}$$

Now, we look at

$$-\int_{Z_k^{\mathrm{bl}}} \nabla(\omega_k^{\mathrm{bl}} - \omega_{k,h}^{\mathrm{bl}})\beta_{k,h}^{\mathrm{bl}} dx = \int_{Z_k^{\mathrm{bl}}} \nabla(\omega_k^{\mathrm{bl}} - \omega_{k,h}^{\mathrm{bl}})(\beta_k^{\mathrm{bl}} - \beta_{k,h}^{\mathrm{bl}})dx \qquad (2.4.24)$$

Adding the two equations (2.4.23) and (2.4.24), we obtain

$$|C^{\mathrm{bl}}_{k,h} - C^{\mathrm{bl}}_k| \leq ||\nabla(\beta^{\mathrm{bl}}_k - \beta^{\mathrm{bl}}_{k,h})||^2_{L^2(Z^{\mathrm{bl}}_k)} + 2\Big|\int_{Z^{\mathrm{bl}}_k} \nabla(\omega^{\mathrm{bl}}_k - \omega^{\mathrm{bl}}_{k,h})(\beta^{\mathrm{bl}}_k - \beta^{\mathrm{bl}}_{k,h})dx\Big|.$$

Using the Hölder and Poincaré inequality we get

$$\begin{aligned}\textstyle\int_{Z^{\mathrm{bl}}_k} \nabla(\omega^{\mathrm{bl}}_k - \omega^{\mathrm{bl}}_{k,h})(\beta^{\mathrm{bl}}_k - \beta^{\mathrm{bl}}_{k,h})dx &\leq ||\nabla(\omega^{\mathrm{bl}}_k - \omega^{\mathrm{bl}}_{k,h})||_{L^2(Z^{\mathrm{bl}}_k)}||\beta^{\mathrm{bl}}_{k,h} - \beta^{\mathrm{bl}}_k||_{L^2(Z^{\mathrm{bl}}_k)} \\ &\leq C(k+1)||\nabla(\omega^{\mathrm{bl}}_k - \omega^{\mathrm{bl}}_{k,h})||_{L^2(Z^{\mathrm{bl}}_k)}||\nabla(\beta^{\mathrm{bl}}_{k,h} - \beta^{\mathrm{bl}}_k)||_{L^2(Z^{\mathrm{bl}}_k)}.\end{aligned}$$

From proposition 2.4.6 it follows that

$$\begin{aligned}|C^{\mathrm{bl}}_{k,h} - C^{\mathrm{bl}}_k| &\leq ||\nabla(\beta^{\mathrm{bl}}_{k,h} - \beta^{\mathrm{bl}}_k)||_{L^2(Z^{\mathrm{bl}}_k\setminus S)}\big(||\nabla(\beta^{\mathrm{bl}}_{k,h} - \beta^{\mathrm{bl}}_k)||_{L^2(Z^{\mathrm{bl}}_k\setminus S)} \\ &\quad + ||\nabla(\omega^{\mathrm{bl}}_{k,h} - \omega^{\mathrm{bl}}_k)||_{L^2(Z^{\mathrm{bl}}_k\setminus S)}\big) \leq C(k)h^{2p-1}.\end{aligned}$$

□

Further details concerning FEMLISP can be found in [44] and [45].

2.4.3 Discretization of the optimization problem

Usually an exact solution of an optimization problem can not be found by hand such that an approximation is often necessary. This appropriate discretization is a transformation of the original problem into a new one which has only a finite number of degrees of freedom. The discretization must be done in such a way that the resulting problem is a good approximation to the original one.

We start with the discretization of G, the set of admissible shapes, defined in section 2.1. Let $0 = y_0 < y_1 < ... < y_N = 1$, $N \in \mathbb{N}$ be an equidistant partition of $[0,1]$ with the step size $H = \frac{1}{N}$. Instead of general functions from G we consider now piecewise cubic splines:

$$G_H = \{\gamma_H \in C^2([0,1]) \Big|\ \gamma_H\big|_{[y_{i-1},y_i]} \in S^{(3,2)}_H, i = 1, ..., N\} \cap G.$$

The discretized cost function of our optimization problem defined in section 2.1 is a function:

$$\mathcal{J} : G_H \subseteq \mathbb{R}^N \to \mathbb{R}$$
$$\mathcal{J}(\gamma_H) := J(\gamma_H, \beta^{\mathrm{bl}}_{k,h}),$$

where $\beta^{\mathrm{bl}}_{k,h} \in H_h$ is the solution of the discretized state equation (2.4.22).

We define now the discretization of our optimization problem as follows:

$$\left\{\begin{array}{l} \min_{\gamma_H \in G_H} \mathcal{J}(\gamma_H) \\ \\ \text{subject to the discretized boundary layer equation:} \\ \\ \begin{aligned}\textstyle\int_{Z^{\mathrm{bl}}_k} \nabla\beta^{\mathrm{bl}}_{k,h}\nabla\varphi_{k,h}dy + \int_{Z^{\mathrm{bl}}_k} \nabla\omega^{\mathrm{bl}}_{k,h}\varphi_{k,h}dy &= -\textstyle\int_S \varphi_{k,h}e_1 \\ \\ \textstyle\int_{Z_{k,h}} \mathrm{div}\beta^{\mathrm{bl}}_{k,h}\chi_{k,h} &= 0.\end{aligned} \end{array}\right. \tag{2.4.25}$$

Under the above assumptions, problem (2.4.25) has a solution for any $H > 0$.

After all the simplifications done in the former sections we know that the Navier constant for a configuration γ_H is our object function:

$$\min_{\gamma_H \in G_H} \mathcal{J}(\gamma_H) = \min_{\gamma_H \in G_H} C_{\mathrm{bl}}^{\mathrm{k,h}}(\gamma_H), \tag{2.4.26}$$

and we observed that with the discretization chosen we made an approximation error of order h^{2p-1}. For the total error done cutting the domain and discretizing for a given configuration γ approximated by γ_H we have

$$\begin{aligned} |\mathcal{J}(\gamma) - \mathcal{J}(\gamma_H)| &= |C_{\mathrm{bl}} - C_{\mathrm{bl}}^{\mathrm{k,h}}| \\ &\leq |C_{\mathrm{bl}} - C_{\mathrm{bl}}^{\mathrm{k}}| + |C_{\mathrm{bl}}^{\mathrm{k}} - C_{\mathrm{bl}}^{\mathrm{k,h}}| \\ &\leq Ce^{-2\pi k} + Ch^{2p-1}. \end{aligned} \tag{2.4.27}$$

2.4.4 Some comments on the optimization routine

We presented already in section 2.2.1 our concept for the minimization algorithm. Here we want to comment the single steps after we have presented all the details about the numerical approximations.

The optimization routine is written in C++. With exception of the starting shape, the rough boundary Γ is known only in the discretization points. To assure the regularity $\Gamma \in C^2$, the boundary will be represented with a cubic spline interpolation. The formulas for this interpolation assure the smoothness of the first derivative and the continuity of the second one, both within the interval $[0, 1]$ and at its boundary. Cubic splines are practical because using additional boundary conditions (i.e. natural cubic splines) the resulting equations for the second derivatives are a tridiagonal system which can be solved in $O(N)$ operations by a tridiagonal algorithm. With this cubic spline interpolation we get also the values for the first derivative of Γ and with this the values for the normals on this boundary:

$$n_1 = \frac{-\Gamma'}{\sqrt{\Gamma'^2 + 1}}$$
$$n_2 = \frac{1}{\sqrt{\Gamma'^2 + 1}}.$$

The discrete values for the rough boundary are sent to the software package FEMLISP which calculates the solution of the state equation. This transfer is realized by a TCP/IP socket connection. TCP called Transmission Control Protocol is one of the two important transport protocols set up with the IP-protocol. It guarantees a secure data transfer while re-sending the data packages if they do not reach the listener after some time and guarantees a correct order. We can send command lines to FEMLISP which can be directly executed. We have to create the client program which initiates the connection with the server, where a server program has to accept the connection. After this, data can be send in both directions until the connection is closed. The server send us back the gradient of the solution of the state equation evaluated on the rough boundary.

Having now the gradient along the boundary the next step in our optimization routine is to calculate the normal derivative on the boundary. It follows the calculation of the sensitivities and of α. Then a function is implemented which calculates the new shape in the normal direction with an optimal step size (Armijo rule) taking care not to violate the constraints. Because of the normal variation we need further evaluations of the new shape, its derivatives and normals on the same grid points as before. This is again done by cubic spline interpolation. We implemented the Armijo line search here because there the optimal step size can be established in a finite number of steps. Of course each step needs one additional solution of the state problem but with this the total number of the iterations of the optimization algorithm shrinks and we reach the optimal shape much faster.

2.5 Numerical Results

We will give some examples of the numerical calculations. As mentioned before we tested the calculations on the rough boundary layer first with rectangular elements and uniform refinement. Because of the curved structure of the microstructure it turns out that adaptive triangles given through a mesh generator give us better results. In table 2.5.1 the discretized cost function and its a posteriori error are listed for $k = 1$ (the case of two coarse cells) and for the shape of the microstructure given by the function $0.25(\sin(2\pi x + \frac{3}{2}\pi)) - 0.75$. We see that in this case it is enough to refine twice. The used grids for the calculations are shown in figure 2.5.1. In figure 2.5.2 we see the mesh for the domain where the microstructure is a very thin peak.

Table 2.5.1: Numerical results and their error.

level l	$C_{\text{bl}}^{k,h}(l)$	$C_{\text{bl}}^{k,h}(l)$ -$C_{\text{bl}}^{k,h}(l-1)$	cells
0	0.563828769	-	50
1	0.563840156	$1.1387 \cdot 10^{-5}$	200
2	0.563840304	$1.48 \cdot 10^{-7}$	800

The figures 2.5.3, 2.5.4 and 2.5.5 show the results of our optimization applied to cell problem. The left pictures present the values of the solution of the boundary layer problem (2.4.22) for the starting shape of microstructure and the right ones the values of the solutions for the optimized structure. The color black describes the microstructure itself and the color space blue to red represents the calculated values where blue means the lowest value and red the highest. We plotted each calculated component in the same range for a better comparability. That means that in every two pictures one color represents the same value. The range of this values is given under the corresponding pictures. For the two components of the velocity blue describes the velocity zero. The gray domain is

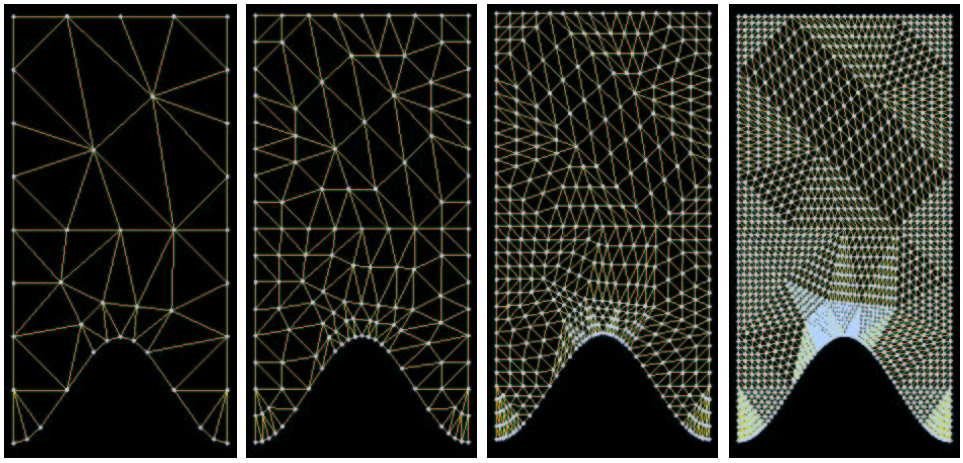

Figure 2.5.1: *The generated grid over a sinus shaped microstructure at level of refinement 0,1,2 and 3.*

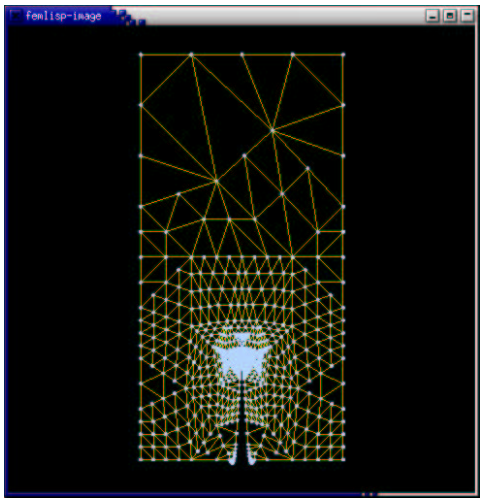

Figure 2.5.2: The grid for the optimized shape.

the region where the velocity reaches negative values so that we can see where we have a back flow but anyway this back flow is very slow. For the case of the starting structure the flow between the microstructures is nearly standing and the gray region is larger than for the optimized structure. For the case of the optimized structure the region of positive flow is smaller so that the flow reaches higher velocities on S which is the proof that the structure is better. In figure 2.5.4 we can see that the second component of the boundary layer velocity is a cavity type flow. The values are very small as expected because the flow movement is the x_1-direction. The microscopic flow over the optimized structure is greater than on the starting structure which again indicates a higher circulation. We see a region of cavity type flow over the microstructures and a region of cavity flow between the microstructures. In the last figure we see the pressure distribution. Here we used the color blue for the lowest negative value and red for the highest positive value. Because of the symmetry of the structure these values have the same absolute value. In the picture we see mostly a constant distribution of the pressure except of a region in front and behind the microstructure. This pressure difference depends of course on the shape of the microstructure: the higher the slope of the shape function the higher the pressure difference. The pressure contribution in the optimized structure is higher and concentrated directly on the tip of the roughness. This fact does not influence our homogenized calculations much because we calculate the tangential drag on a smooth boundary above the roughness and the pressure term disappears because the normal of this smooth boundary is e_2 which is perpendicular to the tangential direction e_1. To have a better understanding of this pressure effect we will compare our calculation with direct calculations on the microscopic rough model which were done from Th. Richter from the numerical simulation group of R. Rannacher from Heidelberg. We will present the results obtained there in the next section.

Next, we give an interpretation of the results obtained for the boundary layer velocity to our cost function

$$\mathcal{J}(\gamma_h) = C_{\mathrm{bl}} = \int_S (\beta_{k,h}^{\mathrm{bl}})_1.$$

We have seen above that on the optimized profile the first component of the boundary layer velocity reaches higher values than on the starting profile. The greater the velocity on S the lower the value for the cost function C_{bl}. This stays in agreement with our assumption that the effective velocity profile is linear in the macroscopic variable x_2 and that the Navier constant C_{bl} describes the origin of the effective velocity profile. The deeper this origin rises into the microstructure the better its shape. How much our cost function is minimized we see in figure 2.5.6. The values rise from -0.56 to -0.578. Typically for a gradient-based method the improvement of the cost functional in the first iterations is greater and then the values converge to an optimal value. Because of the choice of the parametrization of our microstructure, a smooth function constructed with piecewise cubic polynomials, no better shape could be found. But from the sensitivity analysis and also from the observations, how the sequence of solutions develop, we are able to claim that the slit domain, which does not belong anymore in this class, is even better. Several numerical tests confirm this conclusion and also the fact that the optimality conditions are fulfilled in this situation. The cost function for the slit domain is $C_{\mathrm{bl}} = -0.582$ which is the minimal value we obtained in our simulations.

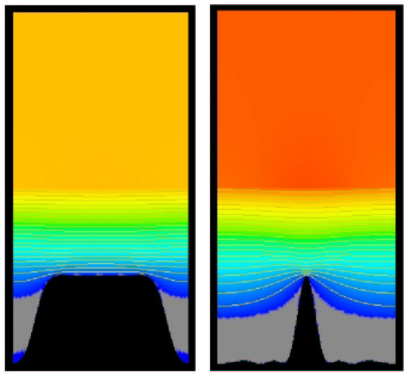

Figure 2.5.3: The x-velocity in the range: 0 – 0.6, a) starting shape, b) optimized shape.

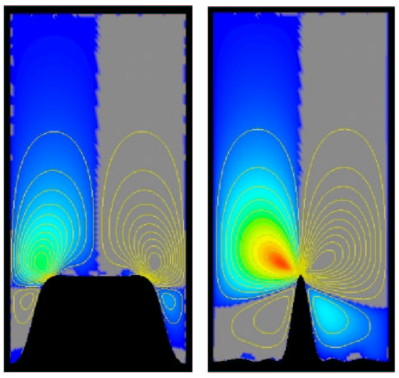

Figure 2.5.4: The y-velocity in the range: 0 – 0.036, a) starting shape, b) optimized shape.

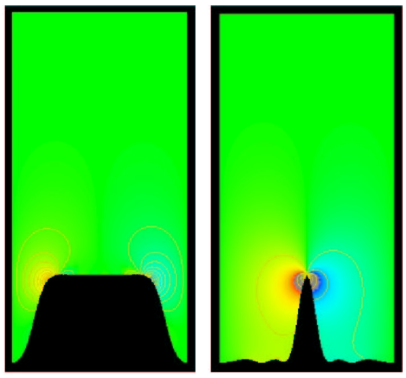

Figure 2.5.5: The pressure distribution in the range: -1.5 – 1.5, a) starting shape, b) optimized shape.

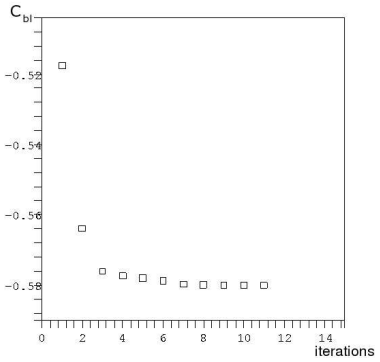

Figure 2.5.6: Minimization of the cost function.

In the next table we see the effect of our minimization results from the macroscopic cell to the tangential drag force for the microscopic problem. Because of the numerous simplifications of our optimization problem the numbers obtained in our optimization are not the numbers for our initial size of interest, the tangential drag force. To see the contribution of our minimization to this quantity of interest we have to go back in the simplifications and insert the obtained values for the cost function C_{bl} in the formula for the tangential drag force which is

$$\mathcal{F}_{\mathrm{t}}^{\mathrm{eff}} = \frac{\nu}{L_2} \frac{U}{1 - \frac{\varepsilon}{L_2} C_{\mathrm{bl}}}. \tag{2.5.1}$$

In this formula our calculated cost function appears with the coefficient ε, our scaling parameter. This indicates that the effect of minimization on the drag will be the smaller the smaller the scaling parameter is. The table 2.5.2 lists the values for the smooth, starting and optimized structure for different scaling parameters, for different sizes of microstructures.

Table 2.5.2: The two-dimensional optimization results in dependence of the scaling.

ε $(L_2 : h)$	$\mathcal{F}_{\mathrm{t}}^{\mathrm{smooth}}$	$\mathcal{F}_{\mathrm{t}}^{\mathrm{eff}}$ starting shape (rel.)	$\mathcal{F}_{\mathrm{t}}^{\mathrm{eff}}$ opt. (rel.)
0.15 (1:13)	1.081	1.0786 (0.2%)	1.067 (1.3%)
0.3 (1:6)	1.1765	1.1707 (0.5%)	1.1416 (2.7%)

The values for the tangential drag decay from left to right. The numbers for the smooth structure are highest which means that microstructures do reduce drag and the values for the optimized structure are lower than for the starting structure which confirms our optimization process. How much the drag is reduced is given in percents in the parenthesis near the respective values. In the first row the microstructures are 0.075 mm high and the effect of our optimization is only slightly higher than 1% which is not so much. For higher

microstructures (0.15mm) the calculated shape is about 2.2% better than the starting structure. We conclude that for the two dimensional model which can be seen as a cross flow model over microstructures we can not obtain big advantages of rough surfaces which can be comparable to the ones obtained in the three dimensional experiments and test mentioned at the beginning. To obtain comparable results we have to consider three dimensional microstructures and a three dimensional flow model. This three dimensional case will be described in the next chapter and we will see that for the case of three dimensional riblets, which were used on the airplane, ships and on the swimmer suits, all the calculations done in this chapter can be used.

2.6 Direct simulations

In this section we compare our results with the data obtained by direct simulation of the oscillating incompressible steady state Navier-Stokes equation (1.2.1) with one of the powerful codes developed by the numerical group of R. Rannacher from Heidelberg. The calculations have been done by Th. Richter using the simulation toolkit Gascoigne, which combines error control, adaptive mesh refinement and a fast solution algorithm based on multigrid methods. The discretization of the oscillating state equations, the Navier-Stokes equations, is here done by stabilized finite elements on locally refined rectangular meshes what allows the treatment of the complex oscillating boundary. For the discretization in space finite elements of second order (Q_2/Q_2) are used. This finite element space is not stable in the sense of the inf-sup condition, a LPS (*local projection stabilization*) with respect to the stable (Q_2/Q_1) Taylor-Hood element was used introduced by R. Becker and M. Braack (see [12]). Due to the easy structure, the equal order ansatz, an efficient implementation is possible which leads to a significant reduction of the computational effort. Error control and mesh adaptation is applied following the framework of the DWR (*dual weighted residual method*) by R. Becker and R. Rannacher (see [13] and [14]). The discretized problem provides 300 000 degrees of freedom on the refined mesh (up to level 8). After applying the Newton method the resulting linear system is solved with GMRES (*generalized minimal residual method*) which uses a V-cycle multigrid method as preconditioner. First results are in table 2.6.3. There we compare four different shapes from our optimization process (see picture 2.6.7) with constant height of 0.15 mm and constant spacing. Shape 1 describes the starting shape, shape 2 and 3 are shapes picked out from the sequence of shapes constructed in our optimization problem and shape 4, the slit domain, has been tested as a candidate for our optimal solution. The values obtained for the skin friction are not direct comparable to the ones obtained with the homogenized formula (1.4.1) because the skin friction was measured in different heights of the channel. In the direct simulation the skin friction is measured directly on the rough skin, where in the homogenized formula the skin friction is measured on the artificial smooth boundary S which lies double as high as the height of the microstructure. The total drag calculated with the direct simulations is given by the sum of the skin friction $\mathcal{F}_{\text{fric}}$ and the form drag or pressure drag $\mathcal{F}_{\text{pres}}$ on the oscillating boundary $\mathcal{B}^\varepsilon$:

$$\begin{aligned} D = \mathcal{F}_t &= \mathcal{F}_{\text{fric}} + \mathcal{F}_{\text{pres}} \\ &= \int_{\mathcal{B}^\varepsilon} \nu \Big[\tfrac{\partial u_1^\varepsilon}{\partial x_1}(x_1,x_2) n_1(x_1,x_2) + \tfrac{1}{2}\Big(\tfrac{\partial u_1^\varepsilon}{\partial x_2}(x_1,x_2) + \tfrac{\partial u_2^\varepsilon}{\partial x_1}(x_1,x_2)\Big) n_2(x_1,x_2) \Big] \\ &\quad - \int_{\mathcal{B}^\varepsilon} p^\varepsilon(x_1,x_2) n(x_1,x_2) e_1. \end{aligned} \tag{2.6.1}$$

This direct two-dimensional calculations from table 2.6.3 confirm that we indeed reduce the total drag and the skin friction in our optimization problem. In agreement with our two-dimensional simulation on one cell of roughness (see figure 2.5.5) we observe that the pressure term of the drag increases, as sharper the bump as higher the contribution to the pressure drag. We recall that in our simulations the pressure term vanished because of the artificial smooth boundary. It remains to clarify in this section how we can compare the results of these two simulations. For shape four it was possible to obtain only two

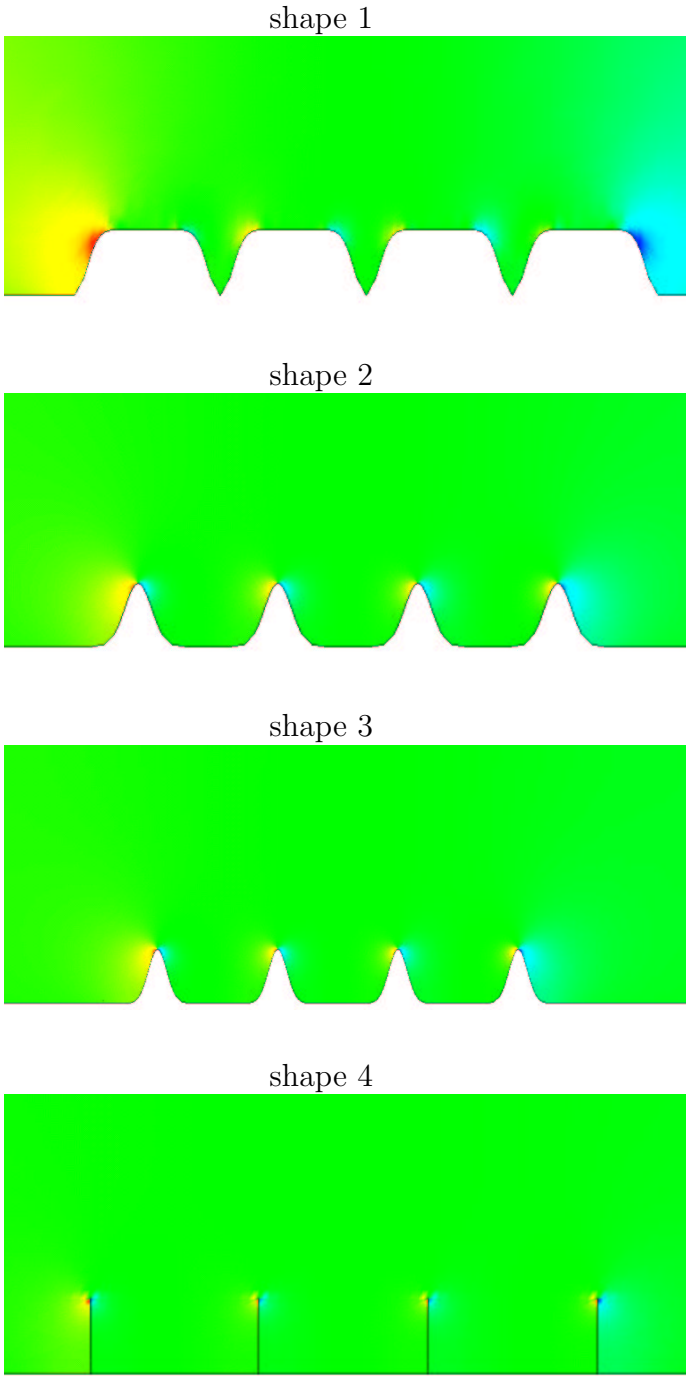

Figure 2.6.7: The pressure distribution on different shapes of microstructures calculated with direct simulations (Th. Richter). The microstructures have the same height and spacing.

Table 2.6.3: The total drag and its components for different shapes tested with direct simulation (Th. Richter).

length	shape 1			shape 2			shape 3		
$[10^{-3}m]$	drag	fric.	pres.	drag	fric.	pres.	drag	fric.	pres.
0.333	0.125	0.065	0.060	0.100	0.0025	0.075	0.100	0.0155	0.085
1.333	0.315	0.185	0.130	0.275	0.065	0.205	0.270	0.0365	0.235
5.320	1.085	0.680	0.405	0.885	0.230	0.755	0.875	0.1185	0.855
21.312	4.160	2.650	1.510	3.825	0.890	2.835	3.800	0.4500	3.350

shape 4		
drag	fric.	pres.
n.a.		
0.28	-0.01	0.29
0.98	-0.075	1.045
n.a.		

results because of the complexity of the mesh and the resulting big error. In these two results the skin friction is very small but negative. This comes from the big region of back circulation where the velocity profile has a negative derivative. In the first raw of the table the values for the drag reduction are much smaller than on the last raw where the length of the channel is much larger. In the simulations for the homogenized problem we calculated always the normalized tangential drag what we have to take into account in the comparison of the results, and also if we compare the results with the values obtained from the experiments.

We have to mention here that the values in the above table were obtained by modeling a two-dimensional channel with smooth parts at the beginning and at the end of the bottom. The rugosities were placed in the middle part. As inflow and outflow condition a Couette flow profile was used with zero boundary condition on the lower part of the boundary and the prescribed velocity U on the upper part of the boundary. This is the reason for the higher pressure difference in front and at the end of the rugosities which can be seen clearly in the first picture of figure 2.6.7 where all of the microstructures are captured. This pressure difference becomes smaller if we make the channel longer. We observe also that this configuration is not suitable if we want to compare the rough channel with a smooth one where the lower boundary is situated on the top of the microstructures. We are able to compare the values obtained only with the smooth configuration where the boundary is at the bottom of the microstructures which gives a better result the viscous sublayer is then thicker. To obtain a comparable model for our homogenized structure we have to change the geometry and the boundary conditions in the direct simulation.

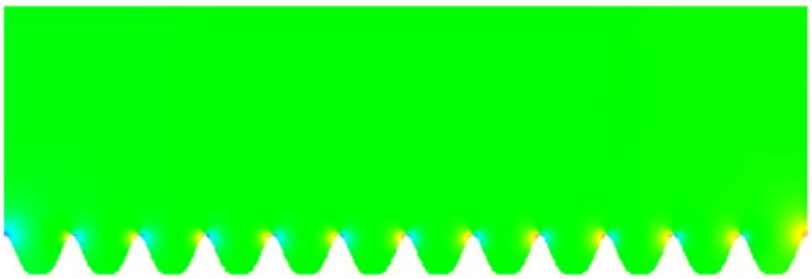

Figure 2.6.8: The pressure distribution on the correct two-dimensional model calculated with direct simulations.

We recall that the width of the channel was 1mm. In our second simulation we choose the length of the channel three times larger than the width which is than 3mm and the bottom should be completely rough starting and ending with the maximum value of the shape function which describes the roughness (see figure 2.6.8). With this geometry it makes sense to choose the origin of the Couette flow for the inflow directly on the top of the microstructure and we get now comparable values to our homogenized problem and also to the correct smooth one.

For the smooth structure the pressure drag $\mathcal{F}_p$ is zero because the normal to the smooth boundary is e_2 which is perpendicular to the tangential direction e_1. Because the velocity profile is a pure Couette profile which means that $\frac{\partial u_2^\varepsilon}{\partial x_1}(x_1, x_2)$ is zero the drag which we calculate in our homogenization process is:

$$\mathcal{F}_{\mathrm{t}}^{\mathrm{eff}} = \frac{1}{2}\nu \int_S \frac{\partial u_1^{\mathrm{eff}}}{\partial x_2}(x_1, x_2). \tag{2.6.2}$$

The velocity profile for the corresponding smooth structure is

$$u^{\mathrm{smooth}} = \frac{U}{L_2 + 0.5\varepsilon}\Big(x_2 + \frac{1}{2}\varepsilon\Big) \tag{2.6.3}$$

and with this the normalized drag is reduced to

$$\mathcal{F}_{\mathrm{t}}^{\mathrm{smooth}} = \frac{1}{2}\nu \frac{U}{L_2 + 0.5\varepsilon}. \tag{2.6.4}$$

To compare the results obtained with the direct simulation with the results obtained with the homogenized model first we choose the same shape function in both simulations:

$$\gamma(x) = \frac{1}{\lambda} \cdot 1.5 \cdot 10^{-4}\Big[\frac{1}{2}\Big(1 + \sin\big(\frac{2}{3}\lambda \cdot 10^3 \pi x\big)\Big)\Big]^2, \tag{2.6.5}$$

where λ is an additional scaling factor This shape function describes a sinus shaped microstructure with height of $\frac{1}{\lambda} \cdot 0.15$ mm and spacing of $\frac{3}{\lambda}$ mm. Then we are able to describe the behavior of the calculated drag with respect to the scaling of the microstructures. We compare the values for the drag on the rough boundary $\mathcal{B}^\varepsilon$ with the values for the drag on the smooth boundary S, situated above the microstructures in a distance of their double height, obtained both with direct simulation denoted by $\mathcal{F}_{\mathrm{t}}^\varepsilon$, with the values obtained

from the homogenized system denoted by $\mathcal{F}_{\mathrm{t}}^{\mathrm{eff}}$ and with the values obtained from the smooth configuration $\mathcal{F}_{\mathrm{t}}^{\mathrm{smooth}}$. The results are presented in table 2.6.4.

In the last two columns where the values are evaluated on the same boundary first by direct simulation and second by our simulation, we observe how close our calculations from the homogenized system are to the direct ones and that the small error decreases with the scaling parameter which in this case is $\varepsilon = \frac{3}{\lambda} \cdot 10^{-4}$. This stays in agreement with the homogenization theory which describes the behavior of an oscillating system for $\varepsilon \to 0$. Comparing the third and fourth column in the table we can conclude that for small ε we can replace the tangential drag on the oscillating boundary with the tangential drag on an artificial smooth boundary. We observe again that the contribution to the drag reduction decrease with the size of the microstructures. The minimization effect in this two-dimensional simulation is very small but we will see in the next chapter that for the three-dimensional simulations we will get a higher contribution.

Table 2.6.4: The numerical results obtained from the homogenized problem in comparison with the results obtained from direct simulations.

height of microstructure [mm]	$\mathcal{F}_{\mathrm{t}}^{\mathrm{smooth}}$	$\mathcal{F}_{\mathrm{t}}^{\varepsilon}$ on $\mathcal{B}^{\varepsilon}$	$\mathcal{F}_{\mathrm{t}}^{\varepsilon}$ on S	$\mathcal{F}_{\mathrm{t}}^{\mathrm{eff}}$ on S
0.15000	3.529	3.088	3.35	3.43
0.03750	3.117	2.995	3.05	3.09
0.01875	3.057	2.991	3.01	3.04

Chapter 3

The shark skin as drag reducing surface

In this chapter we consider the three-dimensional model of a submerged body with a rough surface and we want to know how the shape of this roughness must look like to obtain a smaller drag than the one of the corresponding smooth surface. The resulting model describes the shark skin. As mentioned at the beginning, the shark skin is not smooth. The microstructures found on the surface are similar all over the trunk, their shape differs only in regions like fins and on the places where flow separation has to be avoided like on the snout and on the ends of the fins - there no microstructures are found. This is why we are firstly interested in modeling the shark skin as a straight rough surface. For simplicity we do not consider any curvature to be able to apply the analysis results from [33]. Our resulting model is a three-dimensional channel with a rough bottom. The main flow direction is chosen to be parallel to the x-axis and is called the longitudinal flow. The way to model the Couette flow in the viscous sublayer would be to prescribe the velocity on the upper boundary with $U = (U_1, 0, 0)$ and the no-slip condition on the top of the microstructures. Then we can examine how the linear profile in the x-direction is disturbed by the microstructures. Recently it turned out that this is not the correct model. The latest theory is to consider both longitudinal flow and cross flow in a three dimensional channel. The longitudinal flow is the stream flow and the cross flow is generated by the turbulent motion in the layer above the viscous sublayer. So that the correct model for the viscous sublayer is a deflected Couette flow, deflected from the main stream velocity. The correct boundary condition on the top of the channel is therefore the velocity $U = (U_1, U_2, 0)$. There is a qualitative explanation of why three dimensional riblets do contribute to drag reduction given by Bechert in [10]. He explains that the corrugations interfere with the secondary cross flow associated with the longitudinal vortices which randomly appear in the turbulent flow. Due to this interference these vortices and with them the level of turbulence itself is dampened. The resulting reduction in the rate of turbulent diffusion is responsible for the lower eddy viscosity and thus for the reduction of drag. The quantity of this drag reduction could be given only if we would consider turbulent flow. But this leads beyond the aim of this thesis. We analyze in this chapter only the effect of microstructures which remain within the viscous sublayer of the turbulent flow on the tangential drag force calculated with a homogenized model.

3.1 Modeling of the viscous sublayer of a turbulent Couette flow in 3D

The steady state incompressible Navier-Stokes equation for the three-dimensional viscous sublayer reads as follows:

$$\begin{cases} -\nu\Delta v^\varepsilon + (v^\varepsilon\nabla)v^\varepsilon + \nabla p^\varepsilon &= 0, \text{ in } \Omega^\varepsilon \\ \operatorname{div} v^\varepsilon &= 0, \text{ in } \Omega^\varepsilon \\ v^\varepsilon &= 0, \text{ on } \mathcal{B}^\varepsilon \\ v^\varepsilon &= U, \text{ on } S_2 \\ \{v^\varepsilon, p^\varepsilon\} &- (x_1, x_2) \text{ periodic.} \end{cases} \tag{3.1.1}$$

To introduce the domains in this case we start with the so-called canonical cell of roughness $Z = (0, b_1) \times (0, b_2) \times (0, b_3)$ which is plotted in figure 3.1.2. Because of the periodicity the arbitrary geometry of one microstructure denoted by $\gamma(y_1, y_2)$, where $y_1, y_2 \in (0, b_1) \times (0, b_2)$ are the macroscopic variables, stays in this domain.

The fluid part of this cell is denoted by $Y = \{y \in Z |\ b_3 > y_3 > \max\{0, \gamma(y_1, y_2)\}\}$.

Then the bottom of our three-dimensional channel consists of the layer of roughness given through the periodical repetition of one basic cell of roughness scaled with our scaling parameter ε to obtain the microscopical description. Mathematically the layer of roughness is $\mathcal{R}^\varepsilon = (\cup\varepsilon(Y + (k_1, k_2, -b_3))) \cap ((0, L_1) \times (0, L_2) \times (-\varepsilon b_3, 0))$. We recall the connection between the macroscopic and microscopic variables: $y_i = \frac{x_i}{\varepsilon}$, with $i = 1, 2, 3$. The rough boundary $\mathcal{B}^\varepsilon = \varepsilon(\cup\gamma + (k_1, k_2, -b_3))$ consists of a large number of periodically distributed humps of characteristic length ε but variable height εh with $h \in [0, 1]$. The region above the layer of roughness is the cuboid $P = (0, L_1) \times (0, L_2) \times (0, L_3)$, and the interface which separates this region from the layer of roughness is denoted by $S = (0, L_1) \times (0, L_2) \times (0)$. It is the artificial smooth interface whit what we will replace the rough boundary applying homogenization. Thus the region where the fluid flows is $\Omega^\varepsilon = P \cup S \cup \mathcal{R}^\varepsilon$ (see figure 3.1.1). With S_2 we denote the upper interface $(0, L_1) \times (0, L_2) \times \{L_3\}$, where the velocity is prescribed. The position of S can be fixed arbitrary because a perturbation in its position of order $O(\varepsilon)$ implies a perturbation in the solution of order $O(\varepsilon^2)$ (see [33]).

Numerical simulations for (3.1.1) are even more difficult than for the two-dimensional problem especially when the microstructures are very small. To simplify this huge system we will first apply homogenization and then numerical algorithms to solve the resulting system. This process of homogenization was already described in subsection 1.3, even more details can be found in [33]. The rough boundary $\mathcal{B}^\varepsilon$ will be replaced by an artificial smooth one on which new boundary conditions have to be imposed to take into account the information from the roughness. For the oscillating velocity v^ε following ansatz will be considered: v^ε is constructed as a perturbed Couette flow $v^0 \in P$ which is extended in $\Omega^\varepsilon \setminus P$ by zero. This perturbed Couette flow is written as an asymptotic expansion which

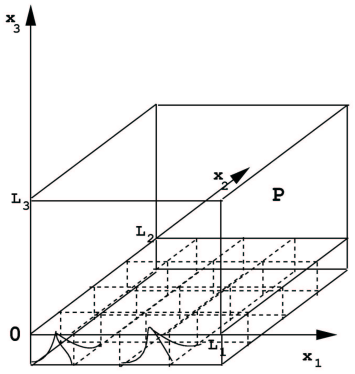

Figure 3.1.1: *The three-dimensional viscous sublayer.*

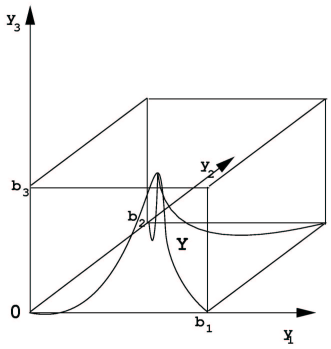

Figure 3.1.2: *The three-dimensional canonical cell of roughness.*

tends in some sense which we will not specify here to the so-called effective solution for $\varepsilon \to 0$. This effective solution is the solution of the resulting effective equations on the smooth domain (see figure 3.1.3) which are:

$$\begin{cases} -\nu\Delta u^{\text{eff}} + (u^{\text{eff}}\nabla)u^{\text{eff}} + \nabla p^{\text{eff}} &= 0, \text{ in } P \\ \text{div } u^{\text{eff}} &= 0, \text{ in } P \\ u^{\text{eff}} &= (U_1, U_2, 0), \text{ on } S_2 \\ u_j^{\text{eff}} &= -\varepsilon \sum_{i=1}^{2} M_{ji} \frac{\partial u_i^{\text{eff}}}{\partial x_3}, \quad j = 1,2 \text{ on } S \\ u_3^{\text{eff}} &= 0, \text{ on } S \\ \{u^{\text{eff}}, p^{\text{eff}}\} \quad (x_1, x_2) &- \text{ periodic.} \end{cases} \tag{3.1.2}$$

We observe that the new boundary condition on the artificial smooth boundary S is similar to the one from the two-dimensional case, it is the Navier slip condition on the two-dimensional surface S. Instead of the Navier constant C_{bl} we have here the Navier matrix which is also defined by the solutions of an auxiliary boundary layer problem (see (3.1.5)):

Definition 3.1.1. Let $\{\beta^\lambda, \omega^\lambda\}$ be the solution for (3.1.5) and $\{\beta^j, \omega^j\}$ be the solutions of (3.1.5) for $\lambda = e_j$, $j = 1, 2$. Then the Navier matrix is defined by

$$M_{ij} := \frac{1}{b_1 b_2} \int_S \beta_i^j dy_1 dy_2.$$

In [33] the authors proved the existence and uniqueness of an effective solution:

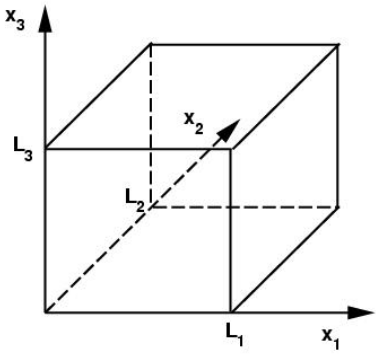

Figure 3.1.3: *The three-dimensional homogenized channel.*

Proposition 3.1.2. If $|U|L_3 < 2\nu$, there is a unique solution of (3.1.2)

$$\begin{cases} u^{\text{eff}} &= (U + (\frac{x_3}{L_3} - 1)(I - \frac{\varepsilon}{L_3}M)^{-1}U, 0), \quad x \in P \\ p^{\text{eff}} &= 0 \quad x \in P, \end{cases} \tag{3.1.3}$$

and obtained the uniform a priori estimates for $\{v^\varepsilon, p^\varepsilon\}$:

Proposition 3.1.3. The Couette flow v^0 is in $\mathcal{O}(\varepsilon^{\frac{3}{2}})$ as approximation of v^ε in $L^2(P)$ and, restricted to S, in $\mathcal{O}(\varepsilon)$ as approximation of v^ε in $L^2(S)$.

The asymptotic expansion for the oscillating Couette flow is

$$\begin{aligned} v^\varepsilon = v^0 &- \tfrac{\varepsilon}{L_3} S^2_{j=1} U_j(\beta^j(\tfrac{x}{\varepsilon}) - (M_{j1}, M_{j2}, 0)H(x_3)) \\ &- \tfrac{\varepsilon}{L_3} S^2_{j=1} U_j(1 - (\tfrac{x_3}{L_3}) - (M_{j1}, M_{j2}, 0)H(x_3)) + O(\varepsilon^2) \end{aligned} \tag{3.1.4}$$

and on the artificial smooth boundary S following equations hold:

$$\frac{\partial v^\varepsilon_j}{\partial x_3} = \frac{U_j}{L_3} - \frac{1}{L_3} S^2_{i=1} U_j \frac{\partial \beta^i_j}{\partial y_3} + O(\varepsilon)$$

$$\frac{1}{\varepsilon} v^\varepsilon_j = -\frac{1}{L_3} S^2_{i=1} U_i \beta^i_j(\frac{x}{\varepsilon}) + O(\varepsilon).$$

The three-dimensional auxiliary problem which plays the crucial role for calculating the Navier matrix reads as follows:

For a given constant vector $\lambda \in \mathbb{R}^2$ find $\{\beta^\lambda, \omega^\lambda\}$ that solve

$$\begin{cases} -\Delta_y \beta^\lambda + \nabla_y \omega^\lambda &= 0, \text{ in } Z^+ \cup Y \\ \operatorname{div}_y \beta^\lambda &= 0, \text{ in } Z^{\text{bl}} \\ \left[\beta^\lambda\right]_S (\cdot, 0) &= 0, \text{ on } S \\ \left[\{\nabla_y \beta^\lambda - \omega^\lambda I\} e_3\right]_S (\cdot, 0) &= \lambda, \text{ on } S \\ \beta^\lambda &= 0, \text{ on } \Gamma \\ \{\beta^\lambda, \omega^\lambda\} \quad (y_1, y_2) &- \text{ periodic,} \end{cases} \tag{3.1.5}$$

where $S = (0, b_1) \times (0, b_2)$, $Z^+ = (0, b_1) \times (0, b_2) \times (0, +\infty)$ and $Z^{\text{bl}} = Z^+ \cup S \cup Y$ (see figure 3.1.4). Note that $\beta^\lambda = S_{j=1}^2 \beta^j \lambda_j, \quad \omega^\lambda = S_{j=1}^2 \omega^j \lambda_j$, where $\{\beta^j, \omega^j\}$ is the solution of the boundary layer problem with $\lambda = e_j$.

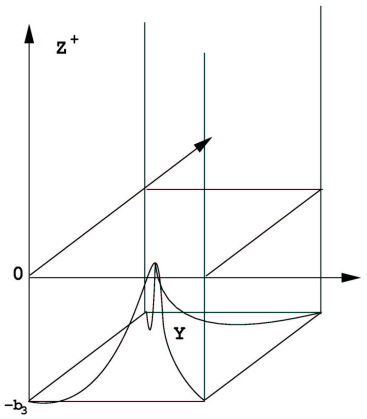

Figure 3.1.4: *The three-dimensional boundary layer Z^{bl}.*

Theorem 3.1.4. If $V = \{z \in L^2_{\text{loc}}(Z^{\text{bl}})^3 : \nabla_y z \in L^2(Z^{\text{bl}})^9; z = 0 \text{ on } \Gamma; \operatorname{div}_y z = 0 \text{ on } Z^{\text{bl}}; z(y_1, y_2) \text{ - periodic}\}$, then there exists an unique solution $\beta^\lambda \in V$ satisfying

$$\int_{Z^{\text{bl}}} \nabla \beta^\lambda \nabla \phi dy = -\int_S \phi \lambda dy_1 dy_2 \quad \forall \phi \in V$$

and $\omega^\lambda \in L^2_{\text{loc}}(Z^{\text{bl}})$ is unique up to a constant.

Proof.

The proof uses the Lax-Milgram lemma and De Rham's theorem (see chapter 2 or [33]). In the neighborhood of S we have $\forall q \in [1, \infty)$ that

$$\beta^\lambda - (\lambda_1, \lambda_2, 0)(y_3 - \frac{y_3^2}{2}) e^{-y_3} H(y_3) \in W^{2,q}$$

and

$$\omega^\lambda \in W^{1,q}.$$

Then following lemma holds:

Lemma 3.1.5. Let $\lambda \in \mathbb{R}^2$ and let $\{\beta^\lambda, \omega^\lambda\}$ be the solution of (3.1.5) satisfying $\int_S \omega^\lambda dy_1 dy_2 = 0$. Then $\beta^\lambda = \sum_{j=1}^2 \beta^j \lambda^j$ and $\omega^\lambda = \sum_{j=1}^2 \omega^j \lambda^j$, where $\{\beta^j, \omega^j\} \in V \times L^2_{\text{loc}}(Z^{\text{bl}})$, $\int_S \omega^j dy_1 dy_2 = 0$, is the solution of (3.1.5) for $\lambda = e_j$, $j = 1, 2$.

We already used this lemma to define the components of the Navier matrix. Now we want to associate a corresponding Navier constant to the Navier matrix M which we will define as follows:

Definition 3.1.6. The Navier constant C^λ_{bl} is defined as

$$C^\lambda_{\text{bl}} := \int_{Z^{\text{bl}}} |\nabla \beta^\lambda(y)|^2 dy < 0. \tag{3.1.6}$$

From [33] we know that

$$C^\lambda_{\text{bl}} = \int_{Z^{\text{bl}}} |\nabla \beta^\lambda(y)|^2 dy = \int_S \beta^\lambda \lambda dy_1 dy_2.$$

Lemma 3.1.7. Let M be the Navier matrix defined above. Then M is negatively definite.

Proof. There is a relation between the Navier matrix and the Navier constant given by

$$M\lambda\lambda = \frac{1}{b_1 b_2} C^\lambda_{\text{bl}} = -\frac{1}{b_1 b_2} \int_S |\nabla \beta^\lambda(y)|^2 dy < 0, \tag{3.1.7}$$

where λ is a given constant vector in $\mathbb{R}^2$.

□

3.2 Modeling of longitudinal riblets

Motivated from nature through the skin of fast swimming sharks we are first interested in a special kind of three-dimensional microstructures, in longitudinal riblets (see figure 3.2.5). This streamlined longitudinal riblets are formed on the surface of the skin by microstructures on the crown of each dermal denticle. This special geometry is believed to reduce drag by damping the cross flow and with this the level of turbulence in the upper layer. It was used also in the experiments mentioned before and tested on aircrafts, ships and swimming suits. The longitudinal riblets are interesting not only from the practical point of view but also because they simplify the three-dimensional equations significantly: The three-dimensional boundary layer equation can be divided in two two-dimensional ones.

Lemma 3.2.1. Let us suppose that the shape of the boundary does not depend on y_1 which is the main flow direction. Then for $\lambda = e_1$ the system (3.1.5) has the solution $\beta^1 = (\beta_1^1(y_2, y_3), 0, 0)$ and $\omega^1 = 0$, where β_1^1 is determined by

$$\begin{aligned}
-\tfrac{\partial^2\beta_1^1}{\partial y_2^2} - \tfrac{\partial^2\beta_1^1}{\partial y_3^2} &= 0 \text{ in } (0,b_2)\times(0,\infty)\cup(Y\cap\{y_1=0\}) \\
\left[\beta_1^1\right](\cdot,0) &= 0 \text{ on } (0,b_2)\times\{0\} \\
\left[\tfrac{\partial\beta_1^1}{\partial y_3}\right](\cdot,0) &= 1 \text{ on } (0,b_2)\times\{0\} \\
\beta_1^1 &= 0 \text{ on } (\Gamma\cap\{y_1=0\}) \\
\beta_1^1 &- y_2 \text{ periodic.}
\end{aligned} \tag{3.2.1}$$

Furthermore for $\lambda = e_2$ the system (3.1.5) has the solution $\beta^2 = (0, \beta_2^2(y_2, y_3), \beta_3^2(y_2, y_3))$ and $\omega^2 = \omega^2(y_2, y_3)$ satisfying

$$\begin{aligned}
-\tfrac{\partial^2\beta_2^2}{\partial y_2^2} - \tfrac{\partial^2\beta_2^2}{\partial y_3^2} + \tfrac{\partial\omega^2}{\partial y_2} &= 0 \text{ in } (0,b_2)\times(0,\infty)\cup(Y\cap\{y_1=0\}) \\
-\tfrac{\partial^2\beta_3^2}{\partial y_2^2} - \tfrac{\partial^2\beta_3^2}{\partial y_3^2} + \tfrac{\partial\omega^2}{\partial y_3} &= 0 \text{ in } (0,b_2)\times(0,\infty)\cup(Y\cap\{y_1=0\}) \\
\tfrac{\partial\beta_2^2}{\partial y_2} + \tfrac{\partial\beta_3^2}{\partial y_3} &= 0 \text{ in } (0,b_2)\times(0,\infty)\cup(Y\cap\{y_1=0\}) \\
\left[\beta_2^2\right](\cdot,0) &= 0 \text{ on } (0,b_2)\times\{0\} \\
\left[\beta_3^2\right](\cdot,0) &= 0 \text{ on } (0,b_2)\times\{0\} \\
\left[\tfrac{\partial\beta_2^2}{y_3}\right](\cdot,0) &= 1 \text{ on } (0,b_2)\times\{0\} \\
\left[\tfrac{\partial\beta_3^2}{\partial y_3} - \omega^2\right](\cdot,0) &= 0 \text{ on } (0,b_2)\times\{0\} \\
\beta_2^2 = \beta_3^2 &= 0 \text{ on } (\Gamma\cap\{y_1=0\}) \\
\{\beta_2^2, \beta_3^2, \omega^2\} &- y_2 \text{ periodic.}
\end{aligned} \tag{3.2.2}$$

Comparing these last equations (3.2.2) with the ones from the two dimensional problem from chapter 2 (see (1.4.4)) we observe that they are exactly the same. We are able to use the results already obtained for the cross flow and have to solve only the flow equations for the longitudinal flow, the Laplace equation (see (3.2.1)).

3.3 The protrusion height

Bechert defined the protrusion height h_p in [8] as the distance of the riblet tips from the virtual origin of the velocity profile. Important is the fact that the origin of the cross flow differs in its location from the origin of the longitudinal flow (see figure 3.2.5). We denote the protrusion height of the longitudinal or parallel flow with $h_{p||}$ and the protrusion

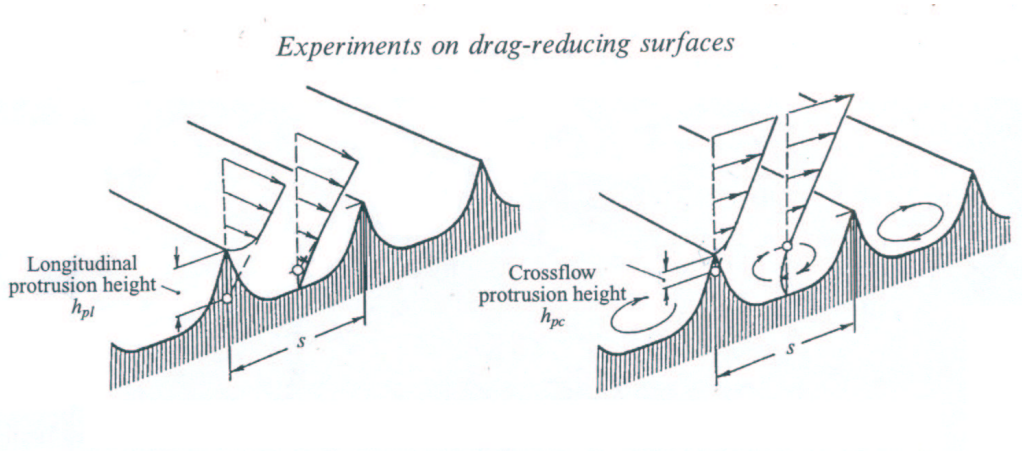

Figure 3.2.5: *Viscous longitudinal and cross flow on a ribbed surface (from [9]).*

height of the cross flow with $h_{p\perp}$. To calculate the protrusions heights in our situation, we have to set the first component of the effective velocity to zero for the parallel protrusion height and the second component to zero for the cross flow. The first two components of the effective velocity are

$$u_i^{\text{eff}} = (U_i + (\frac{x_3}{L_3} - 1)(I - \frac{\varepsilon}{L_3}M)^{-1}U_i), \;\; i = 1, 2.$$

For this special geometry of longitudinal riblets the Navier matrix M has a special structure:

Lemma 3.3.1. If the shape of the boundary does not depend on y_1 then the Navier matrix M is diagonal with the following elements:

$$\begin{aligned} M_{11} &= \tfrac{1}{b_2}\textstyle\int_0^{b_2} \beta_1^1(y_2, 0)dy_2 \\ M_{12} &= M_{21} = 0 \\ M_{22} &= \tfrac{1}{b_2}\textstyle\int_0^{b_2} \beta_2^2(y_2, 0)dy_2. \end{aligned} \tag{3.3.1}$$

Proof. $M_{12} = M_{21} = 0$ follows directly from the definition of M and Lemma 3.2.1. From (3.1.7) we have

$$M\lambda\lambda = \lambda_1^2 M_{11} + \lambda_2^2 M_{22} + \lambda_1\lambda_2(M_{12} + M_{21}) = \frac{1}{b_1 b_2} C_{\text{bl}}^{\lambda},$$

$$\begin{aligned} C_{\text{bl}}^{\lambda} &= \textstyle\int_S \beta^{\lambda}\lambda dy_1 dy_2 = \int_S \big(\lambda_1^2\beta_1^1(y_2, y_3) + \lambda_2^2\beta_2^2(y_2, y_3) + \lambda_1\lambda_2(\beta_1^2 + \beta_2^1)\big) \\ &= \lambda_1^2 \textstyle\int_S \beta_1^1(y_2, 0)dy_2 dy_3 + \lambda^2 \int_S \beta_2^2(y_2, 0)dy_2 dy_3 \\ &= \lambda_1^2 \textstyle\int_0^{b_2} \beta_1^1(y_2, 0)dy_2 + \lambda^2 \int_0^{b_2} \beta_2^2(y_2, 0)dy_2. \end{aligned} \tag{3.3.2}$$

The last equation holds because of the periodicity of the solutions. □

We introduce a new definition:

Definition 3.3.2. $C_{\mathrm{bl}}^{||}$ is the Navier constant from the parallel flow

$$C_{\mathrm{bl}}^{||} := \frac{1}{b_2}\int_0^{b_2} \beta_1^1(y_2,0)dy_2 \tag{3.3.3}$$

and $C_{\perp}^{\mathrm{bl}}$the Navier constant from the cross flow

$$C_{\mathrm{bl}}^{\perp} := \frac{1}{b_2}\int_0^{b_2} \beta_2^2(y_2,0)dy_2. \tag{3.3.4}$$

For the three-dimensional longitudinal riblets we have then

$$M\lambda\lambda = \lambda_1^2 C_{\mathrm{bl}}^{||} + \lambda_2^2 C_{\mathrm{bl}}^{\perp}$$

and

$$M_{11} = C_{\mathrm{bl}}^{||} \qquad M_{22} = C_{\mathrm{bl}}^{\perp}.$$

To come back to the calculation of the protrusion heights we have to calculate the origin of the effective velocity profile. For the first component of the effective flow we have

$$u_1^{\mathrm{eff}} = U_1\Big(1 + \frac{\frac{x_3}{L_3} - 1}{1 - \frac{\varepsilon}{L_3}C_{\mathrm{bl}}^{||}}\Big) \tag{3.3.5}$$

and it follows

$$u_1^{\mathrm{eff}} = 0 \iff \frac{1 - \frac{\varepsilon}{L_3}C_{\mathrm{bl}}^{||} + \frac{x_3}{L_3} - 1}{1 - \frac{\varepsilon}{L_3}C_{\mathrm{bl}}^{||}} = 0 \iff x_3 = -\varepsilon C_{\mathrm{bl}}^{||}.$$

For the second component we have

$$u_2^{\mathrm{eff}} = U_2\Big(1 + \frac{\frac{x_3}{L_3} - 1}{1 - \frac{\varepsilon}{L_3}C_{\mathrm{bl}}^{\perp}}\Big) \tag{3.3.6}$$

and it follows

$$u_2^{\mathrm{eff}} = 0 \iff \frac{1 - \frac{\varepsilon}{L_3}C_{\mathrm{bl}}^{\perp} + \frac{x_3}{L_3} - 1}{1 - \frac{\varepsilon}{L_3}C_{\mathrm{bl}}^{\perp}} = 0 \iff x_3 = -\varepsilon C_{\mathrm{bl}}^{\perp}.$$

Definition 3.3.3. The protrusion height of the parallel flow is given by

$$h_{p||} := \varepsilon C_{\mathrm{bl}}^{||}$$

and the protrusion height of the cross flow is given respectively by

$$h_{p\perp} := \varepsilon C_{\mathrm{bl}}^{\perp}.$$

The protrusion heights are a length which depends only on the chosen reference length and not on the reference velocity. The ratio of the protrusion height to the period of the corrugations $\frac{h_p}{s}$ is called the normalized protrusion height $\bar{h}_p$ and depends only on the shape of the microstructures and neither on their size nor on the actual speed of the fluid. Bechert (in [10]) and Luchini (in [38]) claimed that the only parameter on which the behavior of the turbulent boundary layer depends is the difference between the two protrusion heights $\Delta h = h_{p||} - h_{p\perp}$, the distance between the two virtual plain walls, where the velocity is zero, seen by the longitudinal and cross flow. We will see that the origin of the cross flow lies always higher than the one of the longitudinal flow, and thus Δh is a measure of how much the microstructures impede the cross flow more than the longitudinal flow. The higher the difference between the two protrusion heights is the greater the contribution to the drag reduction.

Projecting these results to our theory we found out that the quantitative parameter which characterizes how much the microstructures reduce drag are here again the Navier constants $C_{\mathrm{bl}}^{||}$ and $C_{\mathrm{bl}}^{\perp}$. Let us calculate the normalized difference between the protrusion heights:

$$\Delta\bar{h} = \bar{h}_{p\perp} - \bar{h}_{p||} = \frac{h_{p\perp} - h_{p||}}{s} = \frac{\varepsilon(C_{\perp}^{\mathrm{bl}} - C_{\mathrm{bl}}^{||})}{\varepsilon} = C_{\perp}^{\mathrm{bl}} - C_{\mathrm{bl}}^{||}.$$

Luchini, Manzo and Pozzi found out in [38] that the maximum possible difference between the heights of the two origins is $\Delta h = 0.132s$, which means $\Delta\bar{h} = 0.132$. Then for the Navier constants the following condition holds: $0 < C_{\perp}^{\mathrm{bl}} - C_{\mathrm{bl}}^{||} \leq 0.132$ for all possibles shapes.

3.4 The three-dimensional optimization problem

For the three-dimensional rough channel the tangential drag force on the artificial smooth surface S is a two-dimensional vector, where

$$\begin{aligned}
\left(\mathcal{F}_{\mathrm{t}}^{\varepsilon}\right)_1 &= \tfrac{1}{L_1L_2}\int_S \nu\sigma n e_1 dy_1 dy_2 \\
&= \tfrac{1}{L_1L_2}\int_S \nu\Big(\big(\tfrac{\partial v_1^{\varepsilon}}{\partial x_1}(x_1,x_2,0) - p\big)n_1 + \tfrac{1}{2}\big(\tfrac{\partial v_1^{\varepsilon}}{\partial x_2}(x_1,x_2,0) + \tfrac{\partial v_2^{\varepsilon}}{\partial x_1}(x_1,x_2,0)\big)n_2 \\
&\quad + \tfrac{1}{2}\big(\tfrac{\partial v_1^{\varepsilon}}{\partial x_3}(x_1,x_2,0) + \tfrac{\partial v_3^{\varepsilon}}{\partial x_1}(x_1,x_2,0)\big)n_3\Big)dx_1dx_2
\end{aligned} \tag{3.4.1}$$

and

$$\begin{aligned}
\left(\mathcal{F}_{\mathrm{t}}^{\varepsilon}\right)_2 &= \tfrac{1}{L_1L_2}\int_S \nu\sigma n e_2 dy_1 dy_2 \\
&= \tfrac{1}{L_1L_2}\int_S \nu\Big(\tfrac{1}{2}\big(\tfrac{\partial v_2^{\varepsilon}}{\partial x_1}(x_1,x_2,0) + \tfrac{\partial v_1^{\varepsilon}}{\partial x_2}(x_1,x_2,0)\big)n_1 \\
&\quad + \big(\tfrac{\partial v_2^{\varepsilon}}{\partial x_2}(x_1,x_2,0) - p\big)n_2 + \tfrac{1}{2}\big(\tfrac{\partial v_2^{\varepsilon}}{\partial x_3}(x_1,x_2,0) + \tfrac{\partial v_3^{\varepsilon}}{\partial x_2}(x_1,x_2,0)\big)n_3\Big)dx_1dx_2.
\end{aligned} \tag{3.4.2}$$

For our geometry the normal to S is $n = e_3$, then we get

$$\left(\mathcal{F}_{\mathrm{t}}^{\varepsilon}\right)_1 = \frac{1}{2}\frac{1}{L_1L_2}\int_S \nu\Big(\frac{\partial v_1^{\varepsilon}}{\partial x_3}(x_1,x_2,0) + \frac{\partial v_3^{\varepsilon}}{\partial x_1}(x_1,x_2,0)\Big)dx_1dx_2 \tag{3.4.3}$$

and

$$\left(\mathcal{F}_{\mathrm{t}}^{\varepsilon}\right)_2 = \frac{1}{2}\frac{1}{L_1L_2}\int_S \nu\Big(\frac{\partial v_2^{\varepsilon}}{\partial x_3}(x_1,x_2,0)+\frac{\partial v_3^{\varepsilon}}{\partial x_2}(x_1,x_2,0)\Big)dx_1dx_2. \tag{3.4.4}$$

Applying homogenization we consider the effective tangential drag force replacing the oscillating velocity with the effective one taking into account that the effective velocity depends only on x_3 and we get

$$\left(\mathcal{F}_{\mathrm{t}}^{\mathrm{eff}}\right)_1 = \frac{1}{2}\frac{1}{L_1L_2}\int_S \nu\frac{\partial u_1^{\mathrm{eff}}}{\partial x_3}(x_1,x_2,0)dx_1dx_2 \tag{3.4.5}$$

and

$$\left(\mathcal{F}_{\mathrm{t}}^{\mathrm{eff}}\right)_2 = \frac{1}{2}\frac{1}{L_1L_2}\int_S \nu\frac{\partial u_2^{\mathrm{eff}}}{\partial x_3}(x_1,x_2,0)dx_1dx_2. \tag{3.4.6}$$

Inserting the formulas for each component of the effective velocity (see (3.3.5) and (3.3.6)) we get following simplification of the components of the effective tangential drag force:

$$\left(\mathcal{F}_{\mathrm{t}}^{\mathrm{eff}}\right)_1 = \frac{\nu}{L_3}\big(1-\frac{\varepsilon}{L_3}C_{\mathrm{bl}}^{||}\big)^{-1}U_1 = \frac{\nu}{2}\,\frac{U_1}{L_3-\varepsilon C_{\mathrm{bl}}^{||}} \tag{3.4.7}$$

and

$$\left(\mathcal{F}_{\mathrm{t}}^{\mathrm{eff}}\right)_2 = \frac{\nu}{L_3}\big(1-\frac{\varepsilon}{L_3}C_{\mathrm{bl}}^{\perp}\big)^{-1}U_2 = \frac{\nu}{2}\,\frac{U_1}{L_3-\varepsilon C_{\mathrm{bl}}^{\perp}} \tag{3.4.8}$$

The approximation error which is done in this process is

$$|\mathcal{F}_{\mathrm{t}}^{\mathrm{eff}}-\mathcal{F}_{\mathrm{t}}^{\varepsilon}| \le C_F(\frac{\varepsilon|U|}{L_3})^2.$$

In our optimization problem we want to find the shape of microstructures which minimizes the tangential drag force:

$$\min_{\gamma\in G}|\mathcal{F}_{\mathrm{t}}^{\mathrm{eff}}| \iff \min_{\gamma\in G}\quad \left(\mathcal{F}_{\mathrm{t}}^{\mathrm{eff}}\right)_1^2+\left(\mathcal{F}_{\mathrm{t}}^{\mathrm{eff}}\right)_2^2. \tag{3.4.9}$$

Due to our simplifications from above the resulting optimization problem is

$$\min_{\gamma\in G} C_{\mathrm{bl}}^{||}+C_{\mathrm{bl}}^{\perp} \tag{3.4.10}$$

which can be decomposed into two optimization problems: In the first one we minimize the longitudinal Navier constant

$$\begin{cases} \min_{\gamma\in G} C_{\mathrm{bl}}^{||} \iff \min_{\gamma\in G}\frac{1}{b_2}\int_0^{b_2}\beta_1^1(y_2,0)dy_2 \\ \text{subject to} \\ -\frac{\partial^2\beta_1^1}{\partial y_2^2}-\frac{\partial^2\beta_1^1}{\partial y_3^2} = 0 \text{ in } (0,b_2)\times(0,\infty)\cup(Y\cap\{y_1=0\}) \\ \big[\beta_1^1\big](\cdot,0) = 0 \text{ on } (0,b_2)\times\{0\} \\ \Big[\frac{\partial\beta_1^1}{\partial y_3}\Big](\cdot,0) = 1 \text{ on } (0,b_2)\times\{0\} \\ \beta_1^1 = 0 \text{ on } (\gamma\cap\{y_1=0\}) \\ \beta_1^1 - y_2 \text{ periodic} \end{cases} \tag{3.4.11}$$

and in the second one the Navier constant for the cross flow:

$$
\begin{cases}
\min_{\gamma\in G} C_{\mathrm{bl}}^{\perp} \iff \min_{\gamma\in G} \frac{1}{b_2}\int_0^{b_2} \beta_2^2(y_2,0)dy_2 \\
\text{subject to} \\
-\frac{\partial^2\beta_2^2}{\partial y_2^2} - \frac{\partial^2\beta_2^2}{\partial y_3^2} + \frac{\partial\omega^2}{\partial y_2} = 0 \text{ in } (0,b_2)\times(0,\infty)\cup(Y\cap\{y_1=0\}) \\
-\frac{\partial^2\beta_3^2}{\partial y_2^2} - \frac{\partial^2\beta_3^2}{\partial y_3^2} + \frac{\partial\omega^2}{\partial y_3} = 0 \text{ in } (0,b_2)\times(0,\infty)\cup(Y\cap\{y_1=0\}) \\
\frac{\partial\beta_2^2}{\partial y_2} + \frac{\partial\beta_3^2}{\partial y_3} = 0 \text{ in } (0,b_2)\times(0,\infty)\cup(Y\cap\{y_1=0\}) \\
\left[\beta_2^2\right](\cdot,0) = 0 \text{ on } (0,b_2)\times\{0\} \\
\left[\beta_3^2\right](\cdot,0) = 0 \text{ on } (0,b_2)\times\{0\} \\
\left[\frac{\partial\beta_2^2}{y_3}\right](\cdot,0) = 1 \text{ on } (0,b_2)\times\{0\} \\
\left[\frac{\partial\beta_3^2}{\partial y_3} - \omega^2\right](\cdot,0) = 0 \text{ on } (0,b_2)\times\{0\} \\
\beta_2^2 = \beta_3^2 = 0 \text{ on } (\gamma\cap\{y_1=0\}) \\
\{\beta_2^2,\beta_3^2,\omega^2\} - y_2 \text{ periodic,}
\end{cases}
\tag{3.4.12}
$$

where $G := \{\gamma : [0,b_1]\times[0,b_2] \to [-1,-0.5] \,\big|\, \gamma \in C^2([0,b_1]\times[0,b_2]),\ \gamma(y_1,0) = \gamma(y_1,b_2) = -1,\ \gamma(y_1,\frac{b_2}{2}) = -0.5,\ \gamma(y_1,y_2) \text{ constant in } y_1\ \forall y_1 \in [0,b_1]\}$.

In the last section we observed that the greater the difference between the two Navier constants is the greater the contribution to the drag minimization. The geometrically interpretation of this statement is that we have to minimize the virtual origin for the longitudinal flow and we have to maximize the virtual origin for the cross flow:

$$\max_{\gamma\in G} |C_{\mathrm{bl}}^{\perp} - C_{\mathrm{bl}}^{||}| \iff \{\min_{\gamma\in G} C_{\mathrm{bl}}^{||}\} \wedge \{\max_{\gamma\in G} C_{\mathrm{bl}}^{\perp}\}.$$

But this would mean in the case of the cross flow that we have to do the opposite operation than described in our optimization problem (3.4.12). But we should not forget that we can not solve both optimization problems independently because the two Navier constants are connected to each other by the three dimensional geometry. Changing the shape of γ to minimize $C_{\mathrm{bl}}^{||}$ has a consequence to the Navier constant of the cross flow and changing the shape of γ to minimize $C_{\mathrm{bl}}^{\perp}$ has a consequence to the Navier constant of the longitudinal flow. The values for $C_{\mathrm{bl}}^{||}$ changes during the optimization process (3.4.12). We know from the two-dimensional problem that a worser microstructure for the cross flow is the one with a bigger cross section, with more material, smooth and flat tips. Exactly this type of microstructure dampen the longitudinal flow more because the valleys are too narrow. To solve the three-dimensional optimization problem we have to minimize the Navier constant from the cross flow which is already done in chapter 2, use the results obtained there and calculate the corresponding values for the longitudinal Navier constant. Solving

(3.4.12) we automatically solve (3.4.11) where the Navier constant from the longitudinal flow is minimized even more than the one from the cross flow, and the difference between the two, Δh, gets greater.

3.5 Numerical results for cross and longitudinal flow

In this section we will present our numerical calculations for the three-dimensional longitudinal riblets. As we have seen we can use our results from the two-dimensional calculations: The starting and resulting three-dimensional geometry in the optimization process is constructed by using the starting and calculated optimal shape from chapter 2 as the cross section for the three-dimensional riblets in the coordinates (y_2, y_3), forcing the additional coordinate y_1 to be constant. Then we have only to calculate the solution of the additional boundary layer equation, the Laplace problem (see (3.2.1)) for this geometry which is done by using the software FEMLISP. Due to our work for the two-dimensional situation we need not to solve here an optimization problem. We need only to discretize the cross section of the microstructures, to cut the infinite domain of the boundary layer, transfer the data to the software which creates a mesh for the given domain and discretizes the boundary layer equations, in this case the Laplace equation, on the resulting mesh using finite elements (for more details see chapter 2). Analyzing the results for the longitudinal flow we will see that it is minimized more than the cross flow so that we expect that the effect of minimization of the tangential drag force will be here much greater than in the two-dimensional situation. To calculate how much percents we reduced the drag doing shape optimization we have to insert the calculated values for the Navier constants in the formulas for the tangential drag. Therefore we have to choose our scaling parameter ε. We will list the calculations for different values of ε and will analyze their dependence on the size of the microstructures. All the numbers are obtained with the boundary condition $U = (U_1, U_2, 0)$ on the upper boundary, where $U_1 = U_2 = 10^{-3}\frac{m}{s}$.

Using the starting shape from chapter 2 (see figure 3.5.6) we get the following Navier constants: $C_{\perp}^{\mathrm{bl}} = -0.514$ and $C_{\mathrm{bl}}^{||} = -0.5280$. The normalized difference of the protrusion heights is thus $\Delta\bar{h} = 0.014$. The optimized shape calculated in the former chapter (see figure 3.5.7) gives us following numbers: $C_{\perp}^{\mathrm{bl}} = -0.580$ and $C_{\mathrm{bl}}^{||} = -0.68855$. The normalized difference of the protrusion heights is thus $\Delta\bar{h} = 0.1086$. We recall that the optimized shape obtained with our optimization procedure must be the slit domain. This domain was not possible to obtain directly through optimization because of the regularity conditions imposed on the shape of the microstructures Γ and on α which describes the variation of this boundary. We made further calculation for shapes which we believed to give better results: a thinner peak and the slit domain. For the thinner peak (see figure 3.5.8) we get $C_{\perp}^{\mathrm{bl}} = -0.582$, $C_{\mathrm{bl}}^{||} = -0.69898$ and $\Delta\bar{h} = 0.117$. For the slit domain which is believed to be the optimum in this case we get following values: $C_{\perp}^{\mathrm{bl}} = -0.582$, $C_{\mathrm{bl}}^{||} = -0.7$ and $\Delta\bar{h} = 0.118$. We recall that in experiments it was observed that $\Delta\bar{h} < 0.132$ which is close to our calculations.

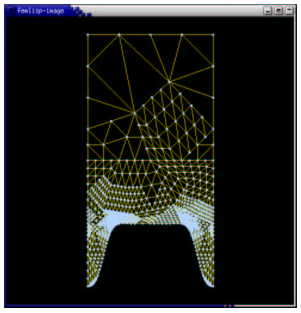

Figure 3.5.6: *Mesh of level 3 created over the cross section of the starting shape to calculate the solution of the Laplace equation.*

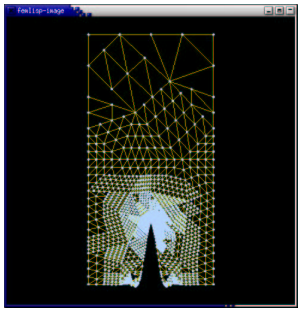

Figure 3.5.7: *Mesh of level 3 created over the cross section of the shape obtained from the optimization process.*

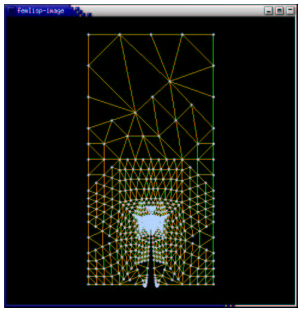

Figure 3.5.8: *Mesh of level 3 created over a thinner peak with more discretization points.*

To evaluate the effect of the microstructures on the drag we compare the values for the drag force for the different structures:

Theorem 3.5.1. The effective tangential drag force measured directly on the tip of the microstructures is given by

$$\mathcal{F}_{\mathrm{t},1}^{\mathrm{eff}} = \frac{\nu}{2}\,\frac{U_1}{L_3 - \varepsilon C_{\mathrm{bl}}^{\parallel}},$$

$$\mathcal{F}_{\mathrm{t},2}^{\mathrm{eff}} = \frac{\nu}{2}\,\frac{U_2}{L_3 - \varepsilon C_{\mathrm{bl}}^{\perp}},$$

and the tangential drag for the smooth surface is in this case

$$\mathcal{F}_{\mathrm{t},1}^{\mathrm{smooth}} = \frac{\nu}{2}\,\frac{U_1}{L_3 + 0.5\varepsilon},$$

$$\mathcal{F}_{\mathrm{t},2}^{\mathrm{smooth}} = \frac{\nu}{2}\,\frac{U_2}{L_3 + 0.5\varepsilon}.$$

Proof. We insert the corresponding components of u^{eff} in $\mathcal{F}_{\mathrm{t}}^{\mathrm{eff}}$ and of v^0in $\mathcal{F}_{\mathrm{t}}^{\mathrm{smooth}}$, where v^0 was the Couette flow in P specified through the boundary conditions on the upper, $v^0(L_3) = U$, and lower boundary, $v^0(-\frac{\varepsilon}{2}) = 0$:

$$v^0(x) = \frac{U}{L_3 + \frac{\varepsilon}{2}}\left(x_3 + \frac{\varepsilon}{2}\right)$$

□

With this, following theorem is true:

Theorem 3.5.2. A rough surface with three-dimensional longitudinal riblets has a lower drag than the corresponding smooth one where holes are drilled in:

$$|\mathcal{F}_{\mathrm{t}}^{\mathrm{eff}}| < |\mathcal{F}_{t}^{\mathrm{smooth}}|$$

This statement corresponds to the claim that under the same conditions the shark is able to swim faster than another fish of the same size and form but with smooth skin.

In our model the riblets are restricted to stay within the viscous sublayer because otherwise a turbulent flow model has to be considered. This is why the size of the sublayer and the size of the microstructures gives the amount how much the drag is reduced. The size of the viscous sublayer is fixed by $L_3 = \sqrt(\nu) \approx 10^{-3}$ m so that we can vary only the sizes of the riblets in changing the scaling parameter ε. Here are some values for the drag for different scaling parameters: For $\varepsilon = 3 \cdot 10^{-4}$ m we have $\mathcal{F}_{\mathrm{t},1}^{\mathrm{smooth}} = \mathcal{F}_{t,2}^{\mathrm{smooth}} = 0.588 \cdot 10^{-6}$ and $\mathcal{F}_{\mathrm{t},1}^{\mathrm{eff}} = 0.582 \cdot 10^{-6}$, $\mathcal{F}_{\mathrm{t},2}^{\mathrm{eff}} = 0.585 \cdot 10^{-6}$. Thus, $|\mathcal{F}_{\mathrm{t}}^{\mathrm{smooth}}| = 0.825 \cdot 10^{-6}$ and $|\mathcal{F}_{\mathrm{t}}^{\mathrm{eff}}| = 1.1867$, which is 3.5% better than the smooth structure. Further evaluations are listed in table 3.5.1.

Table 3.5.1: The three-dimensional optimization results in dependence of the height of the microstructure.

h $[10^{-4}]$	L_3 $[10^{-3}]$	$\frac{\varepsilon}{\delta}$	$\lvert\mathcal{F}_{\mathrm{t}}^{\mathrm{smooth}}\rvert$	$\lvert\mathcal{F}_{\mathrm{t}}^{\mathrm{eff}}\rvert$ non-optimized	$\lvert\mathcal{F}_{\mathrm{t}}^{\mathrm{eff}}\rvert$ optimized
0.25	0.95	0.05	0.725	0.724 (0.14%)	0.720 (0.7%)
0.5	0.9	0.10	0.744	0.7428 (0.16%)	0.731 (1.3%)
0.75	0.85	0.15	0.7644	0.7618 (0.34%)	0.748 (2.1%)
1.0	0.8	0.20	0.785	0.7819 (0.4%)	0.763 (2.8%)
1.5	0.7	0.30	0.8319	0.825 (0.8%)	0.7946 (4.5%)
2.0	0.65	0.35	0.857	0.849 (0.9%)	0.811 (5.4%)
2.5	0.6	0.40	0.884	0.875 (1%)	0.829 (6.2%)

Conclusion

It was our aim to solve the following shape design problem on periodically distributed microstructures: Find the optimal shape of microstructures on the surface of a submerged body such that the tangential drag force is minimized.

This optimization problem was solved by the following approach: The domain of optimization was a channel with the height of the viscous sublayer of a turbulent flow with a rough bottom. The flow equations therein were described by the incompressible steady state Navier-Stokes equation with a Couette flow profile prescribed at the in- and outflow boundary and given by two boundary conditions, by the no-slip condition on the lower boundary and the friction velocity $U \sim \sqrt{\nu}$ on the upper boundary. These state equations have rapidly oscillating coefficients for small microstructures and are hard, or even impossible, to solve directly without special software. Therefore, in the first part of this thesis, we described the approximation process of these state equations via homogenization, and, in the second part, we solved the optimization problem of the resulting simplified model. This approach is done for two and three dimensions, where the optimization problem in three dimensions was solved only for a special geometry that involves longitudinal riblets, which were observed on the skin of fast swimming sharks.

Homogenization theory facilitates our numerical computations of physical phenomena in which microscopic irregularities arise. The macroscopic (averaged) model is derived by describing the limiting behavior (where the period tends to zero) of the solutions of an elliptic boundary value problem with periodic coefficients. These effective equations have smooth coefficients and solutions. We used the results of W. Jäger and A. Mikelić from [32] and [33] who justified the wall law on the artificial smooth boundary by multiscale expansion, the so-called Navier friction law and proved convergence results for the asymptotic expansion of the velocity, for the mass flow and for the tangential drag force. Deriving the effective solutions analytically was of great impact to our optimization problem. The objective could be replaced by a scalar size, the so-called Navier constant, which was calculated from an auxiliary boundary layer problem, the Stokes equation with additional boundary conditions on the smooth interface. With the developed formula for the effective drag force we were able to prove that a rough surface has smaller drag than the corresponding smooth one. A numerical validitation is given for the optimal step size of microstructures which is twice their height. This result was motivated by the physiognomy of shark skin which was researched by Dinkelacker and Reif in [53], and by experimental results obtained from Bechert and his co-authors in [10], where they measured the optimal groove depth for a rib surface in an oil channel. For blade ribs they obtained an optimal groove depth of half of the lateral rib spacing and for scalloped riblets, an optimal depth which is located near two-third of the spacing.

For the definition of our optimization problem state variables, design parameters, an objective and constraints have to be specified. In our fluid mechanics setting the state variables were the velocity and pressure, first of the incompressible steady state Navier-Stokes equation, and second of the boundary layer equation. The design parameters were given by the parameters which determine the shape of the microstructure; hence, the class of admissible shapes had to be specified. The result obtained by the optimization process depends, among other factors, on the size of the chosen set of admissible shapes. We chose

this set in such a way that the shape function of the microstructures can be represented as a cubic spline function with prescribed height. The objective functional is first the tangential drag force acting on the rough surface, and second the effective tangential drag force acting on the artificial smooth surface which replaces the rough one in the homogenized model. Inserting the formula for the velocity of the effective flow, we end up in minimizing a scalar size, the so-called Navier constant. The main constraints were the governing flow equations, the incompressible steady state Navier-Stokes equation, and the boundary layer equations, the Stokes equation with additional boundary conditions on the smooth interface. The side constraint in our problem was the fixed height of the microstructures.

The smoothness restriction of our parametrization was a necessary assumption considering sensitivity analysis which deals with computations of derivatives of solutions of state problems and cost functionals with respect to shape variations. We considered very small shape variations in the normal direction of the boundary of the microstructure. The most important results obtained here are the analytical representation of the sensitivity, which is given by a boundary integral, which shows a linear dependence in the domain variation, and the proof, that the solutions of the state problem depend continuously on the design variables. The latter together with lower semicontinuity assumptions on the cost functional gives us an existence result of our optimization problem. From the sensitivity, the necessary optimality conditions could be derived and a sequence of admissible shapes which converges to an optimal solution could be constructed.

The optimization problem was therefore solved with a sensitivity-based optimization method, where we chose the steepest descent with Armijo line search for the optimization process. In each iteration the state equation had to be solved several times until the conditions imposed by the Armijo rule are fulfilled. With this choice of algorithms not many iterations are needed to reach an optimal solution. Solving the state equations is much more time consuming than to realize a minimization step. We used an external software for solving partial differential equations on rough boundaries. In our case it was convenient to use the package FEMLISP, developed by N. Neuss for boundary layer problems resulting from modeling the flow over porous media. We were able to transform some approximation results and error estimates to our problem with rough boundary. For the discretization finite elements on unstructured grids and multigrid algorithms were used. An optimal shape was found with this algorithm; it is a thin peak represented with cubic spline functions.

We compared the computed results for the effective tangential drag force with values for the tangential drag force on the smooth configuration, on the rough boundary and on the smooth artificial boundary obtained with direct simulations of the microscopic model. This direct simulations on the rough boundary could be performed with special methods developed in the group of R. Rannacher for bigger scales. The results obtained emphasize on one hand the power of the used simulation toolkit Gascoigne, which could handle microstructures larger than 0.01mm with a period twice their height. On the other hand, the results emphasize the advantage of the homogenized model. For larger scales it can be used as a predictor for the correct model, for the right boundary conditions or even for the choice of shapes. For very small scales the homogenized model becomes more and more accurate whereas direct simulations cannot be performed anymore. Compared to

the software used for the direct simulations, the numerics for the homogenized method is much easier to implement and the calculations can be performed on a normal PC. The computing technics differ and are optimized to each problem. In the direct simulations the big data are handled with unstable finite elements of equal quadratic order to reduce the implementation effort whereas in FEMLISP higher order stable finite elements on a small part of the domain are used.

In this thesis we were able to motivate the influence of the shape of riblets on the viscous sublayer of a turbulent flow, as laboratories have examined in experiments. The most important contribution of the microstructures to the drag minimization seems to be that the cross flow is dampened compared to the smooth case which has the effect that the vortices in the buffer layer loose intensity. The amount of drag reduction depends on the ratio: scaling parameter to width of the viscous sublayer. In our analysis the width of the model is fixed. If we would enlarge it, other state equations for turbulent flow had to be considered. The scaling parameter can be varied: The smaller it is, the smaller the contribution to the drag force.

By changing our parametrization of the shape of the microstructures, i.e. imposing less regularity, we would enlarge our set of admissible shapes. This would create the possibility to find more interesting shapes. Nevertheless, we calculated the cost function for the solution to the state equations on the slit domain, and got an only slightly better result.

To conclude, there remain interesting questions to answer in the future: Would a generalized parametrization with a different methodology in the optimization algorithm lead to a different optimal shape? Is it really necessary to consider generalized three-dimensional structures instead of longitudinal riblets, which leads to a three-dimensional optimization routine and three-dimensional state equations? How can we model the state equations if the riblets reach the buffer layer? And, how big would the amount of drag reduction be in this turbulent flow?

Bibliography

[1] Y Achdou, O. Pironneau, and F. Valentin. Effective boundary conditions for laminar flows over rough boundaries. *J. Comp. Phys.*, 147:187–218, 1998.

[2] Y Achdou, O. Pironneau, and F. Valentin. Effective boundary conditions for laminar flows over rough boundaries. *Journal in Computational Physics*, 147:187–218, 1998.

[3] G. Allaire. Homogenization and two-scale convergence. *SIAM J. Math. Anal.*, 23(6):1482–1518, 1992.

[4] H. W. Alt. *Lineare Funktionalanalysis*. Springer, 1992.

[5] Y Amirat and O. Bodart. Numerical approximation of laminar flows over rough walls with sharp asperities. *Preprint*, 17, 2000.

[6] W. Barthlott, Z. Cerman, and C. Neinhuis. *Der Lotus-Effekt: Selbstreinigende technische Oberflächen nach dem Vorbild der Natur*. Faszination Lebenswissenschaften. Beck, E., 2002.

[7] W. Barthlott and C. Neinhuis. Der Lotus-Effekt: biologische Grundlagenforschung und die Entwicklung neuer Werkstoffe. *Bionik. Ökologische Technik nach dem Vorbild der Natur?*, pages 189–203, 2001.

[8] D.W. Bechert, M. Bartenwerfer, and W.-E. Hoppe, G.and Reif. Drag reduction mechanisms derived from shark skin. *AIAA, In 15th Congr. Intl. Counc. Aeronautical Science*, London, September 7-12:1044–1068, 1986.

[9] D.W. Bechert, M. Bruse, and W. Hage. Experiments with three-dimensional riblets as an idealized model of shark skin. *Experimentsin Fluids*, 28:403–412, 2000.

[10] D.W. Bechert, M. Bruse, W. Hage, J.G.T. van der Hoeven, and G. Hoppe. Experiments on drag-reducing surfaces and their optimization with an adjustable geometry. *J. Fluid Mech.*, 338:59–87, 1997.

[11] D.W. Bechert and W.-E. Hoppe, G.and Reif. On the drag reduction of the shark skin. *AIAA, Shear Flow Control Conference*, Boulder (Colorado), March 12-14:1–18, 1985.

[12] R. Becker and M. Braack. A finite element pressure gradient stabilization for the Stokes equation based on Local Projections. *Calcolo*, 38 (4):173–199, 2001.

[13] R. Becker and R. Rannacher. A feed-back approach to error control in finite elemnt methods: Basic analysis and examples. *East-West J. Numer. Math.*, 4 (4):237–264, 1996.

[14] R. Becker and R. Rannacher. An optimal control approach to a posteriori error estimation in finite element methods. *Acta Numerica 2001*, 2001.

[15] M. P. Bendsøe. *Optimization of Structural Topology, Shape, and Material*. Springer-Verlag, Berlin, Heidelberg, New York, 1995.

[16] A. Bensoussan, J. L. Lions, and Papanicolaou. *Asymptotic analysis for periodic structures*. North Holland, 1978.

[17] Q. Bone. Muscular and energetic fish swimming. *Swimming and flying in nature*, 2, 1975.

[18] S. C. Brenner and L. R. Scott. *The Mathematical Theory of Finite Element Methods*. Texts in Applied Mathematics. Springer Verlag, New York, 1994.

[19] F. Brezzi and R. S. Falk. Stability of higher order Taylor-Hood methods. *SIAM J. Num. Anal.*, 28:581–590, 1991.

[20] D. Ciorănescu and P. Donato. *An introduction to homogenization*. Oxford Lecture Notes in Math. and Appl., 1999.

[21] P. Clemént. Approximation by finite element functions using local regularization. *RAIRO*, 9,R-2:77–84, 1975.

[22] E. Friedmann. Optimal Shape Design and its application to microstructures. In *Proceedings of the 6th World Congress on Structural and Multidisciplinary Optimization*, Rio de Janeiro, 2005.

[23] E. Friedmann (Stöckel). Optimales Shape-Design und seine Anwendung auf die Materialwissenschaften. Master's thesis, Fakultät für Mathematik der Ruprecht-Karls-Universität Heidelberg, 2000.

[24] Ch. Großmann and H.-G. Roos. *Numerik partieller Differentialgleichungen*. Teubner-Verlag, Stuttgart, 1994.

[25] M. D. Gunzburger. *Perspectives in Flow Control and Optimization*. Society for Industrial and Applied Mathematics, 20022.

[26] J. Haslinger and R. A. E. Mäkinen. *Introduction to Shape Optimization. Theory, Approximation, and Computation*. Society for Industrial and Applied Mathematics Philadelphia, 2003.

[27] U. Hornung. *Homogenization and Porous Media*. Springer-Verlag, New York, 1997.

[28] J. W. Hoyt. Hydrodynamic drag reduction due to fish slimes. *Swimming and flying in nature*, 2, 1975.

[29] W. Jäger and A. Mikelić. On the boundary conditions at the contact interface between a porous medium and a free fluid. *Annali della Scuola Normale Superiore di Pisa*, XXIII:403–465, 1996.

[30] W. Jäger and A. Mikelić. On the boundary conditions at the contact interface between two porous media. *Partial Differential Equations, Theory and Numerical Solution*, 406:175–186, 1999.

[31] W. Jäger and A. Mikelić. On the interface boundary conditions by Beavers, Joseph and Saffman. *SIAM Journal on Applied Mathematics*, 60:1111–1127, 2000.

[32] W. Jäger and A. Mikelić. On the roughness-induced effective boundary conditions for a viscous flow. *Journal of Differential Equations*, 170:96–122, 2001.

[33] W. Jäger and A. Mikelić. Couette flows over a rough boundary and drag reduction. *Communications in Mathematical Physics*, 232:429–455, 2003.

[34] W. Jäger, A. Mikelić, and N. Neuss. Asymptotic analysis of the laminar viscous flow over a porous bed. *SIAM J. Scientific Computing*, 22 (6):2006–2028, 2001.

[35] V.V. Jikov, S.M. Kozlov, and O.A. Oleinik. *Homogenization of Differential Operators and Integral Functionals*. Springer-Verlag, Berlin, Heidelberg, New York, 1994.

[36] A. B. Kesel. *Antifouling nach biologischem Vorbild*. BMBF Projekt. Bionik: Innovationen aus der Natur, 2005.

[37] O. Ladyzhenskaya. *The mathematical theory of viscous incompresible flow*. Gorden & Breach, 1963.

[38] P. Luchini, F. Manzo, and A. Pozzi. Resistance of a grooved surface to parallel flow and cross-flow. *J. Fluid Mech.*, 228:87–109, 1991.

[39] A. R. Martin. *Field Guide to the Great White Shark*. ReefQuest Center for shark research, special publication No. 1, 2003.

[40] R. Mehnert, A. Sobottka, and Ch. Elsner. Microstructured Polyacrylate surfaces generated by UV&EB Curing. *Proc. RadTech Europe*, Basel, October 8-10:603–608, 2001.

[41] B. Mohammadi and O. Pironneau. *Applied Shape Optimization for Fluids*. Oxford University Press, Oxford New York, 2001.

[42] B. Mohammadi, O. Pironneau, and F. Valentin. Rough boundaries and wall laws. *Int. J. Numer. Meth. Fluids*, 27:169–177, 1998.

[43] W. Nachtigall. *Bionik*. Springer-Verlag, 2002.

[44] N. Neuss. FEMLISP - a toolbox for solving partial differential equations with finite elements and multigrid. *SFB-Preprint*, 2003.

[45] N. Neuss. Schnelle numerische Approximation von effektiven Parametern mit einer interaktiven Finite-Elemente Umgebung. *Habilitationsschrift*, 2003.

[46] O. Pironneau. On optimum profiles in Stokes flow. *J. Fluid Mech.*, 59:117–128, 1973.

[47] O. Pironneau. On optimum design in fluid mechanics. *J. Fluid Mech.*, 64:97–110, 1974.

[48] O. Pironneau. *Optimal Shape Design for Elliptic Systems*. Springer-Verlag, New York, 1984.

[49] E. Polak. *Computational methods in optimization*, volume 77 of *Mathematics in science and engineering*. Academic Press, 1992.

[50] W. H. Press, S. A. Teukolsky, W. T. Vetterling, and B. P. Flannery. *Numerical recipes in C++. The art of scientific computing.* Cambridge University Press, 2002.

[51] R. Rannacher. *Numerik partieller Differentialgleichungen*. Vorlesungsskript.

[52] R. Rannacher. *Numerische Methoden der Kontinuumsmechanik*. Vorlesungsskript, 2005.

[53] W.-E. Reif and A. Dinkelacker. Hydrodynamics of the squamation in fast swimming sharks. *Neues Jahrbuch für Geologie und Paläontologie Abhandlungen*, 164:184–187, 1982.

[54] H. Schlichting and K. Gersten. *Boundary-Layer Theory*. 8th revised and enlarged edition. Springer-Verlag, Berlin, 2000.

[55] J. Sokolowski and J. P. Zolesio. *Introduction to shape optimization*. Springer Series in Computational Mathematiks. Springer, 1992.

[56] K. Sch. Steuben and G. Krefft. *Die Haie der Sieben Meere*. Verlag Paul Parey, Hamburg und Berlin, 1995.

[57] S. P. Vanka. Block-implicit multigrid solution of Navier-Stokes equations in primitive variables. *J. Computational Physics*, 65:138–158, 1986.

[58] M. J. Walsh. Riblets as a viscous drag reduction technique. *AIAA Journal*, 21 No. 4, 1983.